Properties and Applications of Potassium Lithium Tantalate Niobate

Thesis by

Xiaolin Tong

In Partial Fulfillment of the Requirements
for the Degree of
Doctor of Philosophy

California Institute of Technology

Pasadena, CA

1998

To My Parents and Min

Acknowledgements

First, I would like to thank my thesis advisor Prof. Amnon Yariv for the support, instruction, and inspiration he has given me over the last four years. His encouragement and trust in my research will always be remembered and appreciated. It truly has been both a privilege and a rewarding experience to work in the atmosphere of his research group. I am also especially grateful to Drs. Aharon Agranat and Rudolf Hofmester for their energetic and enthusiastic support as well as their friendship and guidance. I am indebted to Drs. Mordechai (Moti) Segev and Tony Kewitsch for numerous enlightening discussions on physics and experimental techniques.

Special thanks to Dr. Bin Zhao who introduced and recommended me to Caltech, Professor T. R. Chen, and Y. H. Zhuang who provided invaluable guidance in many aspects beyond the research. I enjoyed their friendship. I would also like to express my appreciation to Jana Mercado for the help I received during my stay with the group.

Many members of the Quantum Electronics Group deserve appreciation as well for their assistance and support, including Gilad Almogy, Salik Boaz, Gert Cauwenberghs, Kevin Cooper, Danny Eliyahu, Doruk Engin, Jing Feng, Ali Ghaffari, John Iannelli, John Kitching, Roger Koumans, Reg Lee, Dr. Victor Levya, Zhiwen Liu, Matt McAdams, Bill Marshall, John O'Brien, Sergei Orlov, Volnei Pedroni, Eva Peral, Dan Provenzano, Dr. George Rakuljic, Dr. Joseph Rosen, Akira Saito, Randy

Salvatore, Thomas Schrans, Ali Shakouri, Atsushi Sugitatsu, Scott Van Essen, Yong Xu, and Yuanjian Xu.

I have also received invaluable help from many other faculty, students and staff at Caltech community throughout the years. Especially I would like to thank Prof. George Rossman and Prof. Bill Johnson for their encouragement and advise. Thanks are extended to Xiaochang Cheng, Haiyun Tang, Ning Zhang and Yongfang Zhang for many fruitful and stimulating discussions. The help and kindness of Parandeh Kia, Paula Samazon, Reynod Johnson and Larry Begay are truly appreciated. I would also like to thank Tony Stark, Ray Garcia, Paul Carpenter for their assistance.

I wish to thank the numerous individuals whom I have had the pleasure to work with, including Quanlu Song, Chaoen Huang, Daya Jiang, Anyi Li, Yong Lu, Xiaoyan Ma, Dezhong Shen, and Shuqing Zhao of Research Institute of Synthetic Crystals in Beijing. Special thanks to Liang Xiaho and Guangya Hu for their support and kindly help.

Finally, I would like to thank my parents and Min Zhang for their unwavering support and encouragement.

Abstract

This thesis describes the physical and photorefractive properties of potassium lithium tantalate niobate (KLTN) single crystal material.

The top seeded solution growth method is reviewed. The phase transition temperatures and dielectric properties are related to the compositions of the KLTN crystals. A liquid/solid interface dynamics model is introduced to explain the experimental results which is that hydrogen ion concentration in KLTN crystals can be reduced dramatically by doping copper in the absence of titanium.

Dark conductivity of KLTN crystals are contributed by two species when the temperature is in the range of 250 K and 350 K. Two species are hydrogen ions and shallow trapped electrons (holes). These results have been confirmed by direct dc conductivity measurments and holograms fixing experiments. Hydrogen ion has two typies of motion in the crystals: O-H vibration and O-H libration. We established a model to describe hydrogen ions motions and hopping in KLTN crystals. The theoretical prediction is in agreement with experimental results. Hologram thermal fixing for optical data storage is discussed. Hydrogen ions are identified as the mobile ion which is responsible for thermal fixing.

In ferroelectric phase KLTN crystals, spontaneous polarization of individual microdomains can be aligned throughout the entire crystal by

the poling process. Photorefractive space charge fields play a role deploing the microdomains wherever space charge field opposing to spontaneous polarization. This may cause microdomain switching and lead to the generation of index grating. Experimental observation of Barkhausen current jumps is the signature of domain inversion.

Holograms thermal fixing in potassium niobate crystals are also investigated. Because potassium niobate crystal has an orthognal structure with space group mm2, 3D polarization dependence of OH bands are observed. A special cut of iron doped potassium niobate crystal was designed to achieve the maximum exponential gain coefficient for thermal fixing of volume holograms. A significant enhancement of diffraction efficiency of the fixed grating 43% is measured.

The last part of this thesis discussed topological distribution of phase matching of three-wave mixing in biaxial crystals. Thirty possible distributions are illustrated. The optimum operating directions under phase matching condition in biaxial crystal can be obtained from the calculation of the effective nonlinear coefficients. A set of analytical expressions of effective nonlinear optical coefficient for the crystals with mm2 point group is given. The phase matching directions are in either x, y, or z plane in order to obtain maximum coefficient.

Table of Contents

Chapter One

Introduction to the Photorefractive Nonlinear Optics and Applications

1.1 Introduction

The photorefractive effect refers to a light-induced refractive index change observed in certain photoconductive electro-optic materials. The effect produces refractive index changes with relatively low intensities of incident light. The photorefractive effect arises through the photoexcitation, transport, and subsequent re-trapping of charge. When a photorefractive medium is illuminated by a grating pattern, photoexcited carriers migrate from bright regions to dark regions. The separation of charge sets up a space charge field which, through the electro-optic effect gives rise to a refractive index grating and hence a phase hologram. The refractive index grating may persist for several hours or even longer if the photorefractive material is kept in the dark. However, it can be erased by exposing the material to uniform illumination. To prevent the erasure of these gratings of volume holograms during readout, numerous fixing techniques have been developed. These techniques will be discussed in this thesis.

The photorefractive effect was first reported as "optical damage" at Bell Labs in frequency doubling experiments using lithium niobate in 1966 by Ashkin [1] and independently by Chen [2]. Chen published the first

charge migration model in 1969 specific to photorefractive, ferroelectric crystals [3]. The model used the spontaneous polarization characteristic of such materials combined with the illumination pattern due to the interference of two beams within the medium, to explain the formation of volume holograms in ferroelectrics. This model suggested that ultra-violet illumination and thermal re-excitation are typically required for erasing holograms. Thaxter [4] reported the influence of an applied electric field on hologram storage in SBN, lending support to the "drift" model for carrier migration. Amodei showed [5] that charge migration by diffusion may play an important part in holographic recording for sufficiently small grating spacings and derived expressions for the electric field patterns generated through drift and diffusion for plane-wave holograms.

Drift and diffusion mechanisms did not account for the efficiency of the photorefractive effect in certain materials. Hence Glass et al. introduced the bulk photovoltaic effect [6]. This effect is due to the asymmetry of the crystal which, caused photoionized charge carriers to be ejected into the conduction band preferentially in a particular direction relative to the spantaneous polarization of the crystal, thus giving rise to a photocurrent. This has been widely accepted as a contribution to the photorefractive effect.

Yariv illustrated [7] that the wave formalism used to describe photorefractive four-wave mixing was identical to the formalism employed to discuss nonlinear optical degenerate four-wave mixing. Optical phase conjugation of a signal beam is the generation of a light beam with an

identical phase front to the signal, but propagating in the opposite direction [8].

In 1979 Kukhtarev et al. published [9] the most complete model to date. It took into account the effects of externally applied electric fields, the bulk photovoltaic effect, and the recursive effects of the space charge field on the distribution of the space charge field itself. The model described how a refractive index grating was established with the same spatial frequency as the interference pattern and was shifted by a factor of $\pi/2$ with respect to the interference pattern in the absence of applied field.

Alternatey, the following year Feinberg proposed [10] a model that was not based on a band transport approach. It was called a "hopping" model, and involved a simple physical picture of charge carriers hopping from site to site, with the probability of hopping dependent on the local light intensity and electric field.

A photorefractive material should exhibit several properties. First, it should possess a gap, partially filled photoionizable impurity level. Second, it must be linearly electro-optic to exhibit the conventional photorefractive effect, or quadratically electro-optic to display the electric field controlled photorefractive effect. Several characteristics are used to distinguish the various materials from each other. They include the response time, the dark current, the sensitivity, the magnitude of the induced index change, and the phase shift.

Some inorganic materials typically employed in photorefractive experiments include bismuth silicon oxide (BSO) [11], bismuth germanium oxide (BGO) [12], $LiTaO_3$ [3], $LiNbO_3$ [13], $Sr_2BaNb_2O_6$ (SBN) [14], $KNbO_3$ [15], $BaTiO_3$ [16], and KLTN [17]. The ferroelectric oxides (SBN, $KNbO_3$ $BaTiO_3$ etc.) tend to have slow response times and relatively low sensitivities because of their low carrier mobility. The photorefractive sillenites (BSO, BGO, etc.) tend to have much smaller dielectric constants and higher photoconductivities than the ferroelectric oxides, hence they have faster response times.

The study of the materials themselves is an important part of the work. Their understanding and control provides insight into the electronic and optical characteristics. KLTN as an example has been described in detail regarding infrared absorption, conductivity, phase transition etc. throughout this thesis.

1.2 Applications

Numerous applications of the photorefractive effect have been investigated. One of the first was holographic data storage, where it was predicted that the ultimate storage capacity would be $\sim 10^{12}$ bits cm^{-3} [18,19]. This culminated in the simultaneous storage of 500 fixed holograms in one crystal sample [20]. In addition, since the photorefractive effect leads to an index grating which, in general, is not in-phase with the intensity pattern, the power in the two beams is coupled, leading to optical

power transfer [9]. Beam coupling was used to demonstrate the amplification of weak signal beams by factors of several thousand [21]. Real time image processing involving cross-correlation and two image processing techniques have been demonstrated by Yariv's group [22]. Image contouring [23], edge enhancement [24], and adaptive optical techniques to correct distortion [25] have also been performed.

Photorefractive materials may also be important in the field of integrated optics. A change of the refractive indices in photorefractive waveguides by visible light has been used for the formation of components such as gratings for optical switches or wavelength division multiplexes (WDM) [26-30]. Such components have the advantages of planer guides that holograms recorded automatically compensate for wavefront perturbations introduced by the mode structure or imperfections.

In recent years, a tunable quasi-phase matching second harmonic generation has been developed using dynamic ferroelectric domain gratings induced by photorefractive space charge field [31].

1.3 Outline of the Thesis

Potassium Lithium Tantalate Niobate (KLTN) is a new type of photorefractive material. The properties of KLTN, such as the ability to control the phase transition temperature, hydrogen concentration of as-grown doped crystal, and ferroelectric domain switching, were studied to

better understand this material and explore new applications of such a material.

In chapter two the band transport model of the photorefractive effect is described. This is used to derive the coupled wave equations of two-wave mixing in photorefractive materials. Fixing based on thermal assisted ionic drift and ferroelectric domain reversal for holographic data storage are reviewed.

The growth of KLTN crystals is discussed in chapter three. The construction of a crystal growth system and the method of top seed solution growth are illustrated. The phase transition temperature is determined via the composition of Ta/Nb. The growth temperature is also a function of the composition of Ta/Nb. Dielectric properties of several compositions of KLTN are presented.

Chapter four examines the infrared absorption of OH band as a function of the dopant. A model based on the experimental results for hydrogen diffusion in a KLTN crystal is proposed. The unique properties of the liquid/solid interface dynamics explain how hydrogen concentration changes significantly by copper doping the KLTN crystals.

Chapter five describes the results of experiments demonstrating thermally assisted ionic transport fixing of volume holograms in KLTN crystals in both the paraelectric phase (in the presence of external electric field) and ferroelectric phase (in the absence of external electric field).

Crystals in the paraelectric phase exhibit no linear electro-optic effect so the conventional photorefractive effect can be modulated by an external field. The mobile species responsible for fixing is identified as the hydrogen ion. On the other hand, no thermal fixing is observed in a KLTN : Cu, V crystals. As expected, the spectral signature of hydrogen ion is absent in the infrared absorption measurements. The activation energy of hydrogen ions in a KLTN crystal is about 0.7 eV. Shallow trapped electrons display only a 0.1 eV activation energy.

Hologram fixing using ferroelectric microdomain switching is the topic of chapter six. The photorefractive space charge field aligns ferroelectric domains and produces a series of displacement current jumps, the so-called "Barkhausen noise". These domain gratings are recorded with spatial periods on the order of a few optical wavelengths. Unlike thermally assisted ionic fixing, fixed gratings based on ferroelectric hysteresis are in-phase with respect to the original space charge field. The diffraction from fixed gratings does not exhibit the decay and subsequent revealing while developing the holograms.

Three dimensional polarization of OH bands are reported in chapter seven. Hydrogen ion motion in perovskite unit cell is a combination of vibration and libration. These two types of motions are perpendicular to one another and can be treated independently. The anisotropy of proton activation energy is analyzed theoretically and confirmed experimentally. A special angle cut crystal is used to optimize the diffraction efficiency of the thermally fixed hologram.

Chapter eight discusses phase matching conditions on optical wave mixing in biaxial crystals. In particular, the topological distributions and effective nonlinear optical coefficient are illustrated for the crystals with space group mm2. Three typical NLO crystals are used to describe the relationship between the structure symmetry coordinate and refractive index coordinate.

References for Chapter One

[1] A. Ashkin, G. D. Boyd, J. M. Dziedzik, R. G. Smith, A. A. Ballman, and K. Nassan, Appl. Phys. Lett. **9**, 72 (1966).

[2] F. S. Chen, J. Appl. Phys. **38**, 3418 (1967).

[3] F. S. Chen, J. Appl. Phys. **40**, 3389 (1969).

[4] J. B. Thaxter, Appl. Phys. Lett. **15**, 210 (1969).

[5] J. J. Amodel, RCA Rev. **32**, 185 (1971).

[6] A. M. Glass, D. Von Der Linde and T. J. Negran, Appl. Phys. Lett. **25**, 233 (1974).

[7] A. Yariv, IEEE J. Quant. Elect. **QE14**, 650 (1978).

[8] R. A. Fisher Ed., Optical Phase Conjugation, Academic Press, Orlando (1983).

[9] N. V. Kukhtarev, V. B. Markov, S. G. Odulov and V. L. VinetskII, Ferroelectrics, **22**, 949, (1979).

[10] J. Feinberg, D. Heiman, A. R. Tanguay, Jr. and R. W. Hellwarth, J. Appl. Phys. **51**, 1297 (1980).

[11] S. L. Hou, R. B. Lauer, and R. E. Aldrich, J. Appl. Phys. **44**, 2652 (1973).

[12] J. P. Herriau, A. Delboulbe and J.P. Huignard, SPIE Proc. **398**, 123 (1983).

[13] W. D. Johnson, J. Appl. Phys. **41**, 3279 (1970).

[14] B. Fisher, M. Cronin-Colomb, J. O. White and A. Yariv, Appl. Phys. Lett. **40**, 863 (1982).

[15] P. Gunter and A. Krumins, Appl. Phys. **23**, 199 (1980).

[16] R. L. Townsend and J. T. La Macchia, J. Appl. Phys. **41**, 5188 (1970).

[17] A. Agranat, R. Hofmeister, and A. Yariv, Opt. Lett. **17**, 713 (1992).

[18] P. J. Van Heerden, Appl. Opt. **2**, 393 (1963).

[19] T. Jannson, Opt. Appl. **IX**, 169 (1979).

[20] D. L. Staebler, W. J. Burke, W. Phillips, J. J. Amodei, Appl. Phys. Lett. **26**, 182 (1975).

[21] F. Laeri, T. Tschudi, J. Albers, Opt. Comm. **47**, 387 (1983).

[22] J. O. White and A. Yariv, Appl. Phys. Lett. **37**, 5 (1980).

[23] Y. Faiman, E. Lenz. and J. Shamir, Appl. Opt. **20**, 158 (1981).

[24] J. Feinberg, Opt. Lett. **5**, 330 (1980).

[25] G. S. Agarwal, A.T. Friberg, and E. Wolf, J. Opt. Soc. Am. **73**, 529 (1983).

[26] R. V. Schmidt, P. S. Cross and A. M. Glass, J. Appl. Phys. **51**, 90 (1980).

[27] S. I. Bozhevol'nyi, E. M. Zolotov, V. A. Kiselov and E. A. Shcherbakov, Sov. J. Quant. Elec. **9**, 216 (1979).

[28] R. P. Kenan, D. W. Vahey, N. F. Hartman, V. E. Wood and C. M. Verber, Opt. Eng. **15**, 12 (1976).

[29] C. M. Verber, V. E. Wood, R. P. Kenan and N. F. Hartman, Ferroelectrics, **10**, 253 (1976).

[30] C. M. Verber, N. F. Hartman and A. M. Glass, Appl. Phys. Lett. **30**, 272 (1977).

[31] A. Kewitsch, M. Segev, A. Yariv, G. Salamo, T. Towe, E. Sharp, R. Neurgoankar, Appl. Phys. Lett. **64**, 3068 (1994).

Chapter Two

Photorefractive Effect and Materials

2.1 Introduction

In photorefractive materials a nonlocal change in the refractive index is caused by an optical pattern. The incident light excites charge carriers preferentially in bright regions where they undergo transport, are repeatedly trapped and re-excited, and are finally trapped in dark regions (Figure 2-1). The resulting separation of charge sets up a space charge field which, through the electro-optic effect, gives rise to a refractive index grating and hence a phase hologram. Two beams propagating in a photorefractive medium can thus interact with one another through coherent scattering from the grating formed by their interference. The phases and the intensities of the two beams can be modified in the process. This chapter describes the band transport mechanism of the photorefractive effect, and the formation of the space charge field. The coupled mode equations are used to calculate the influence of index gratings on the propagation of beams passing through the material.

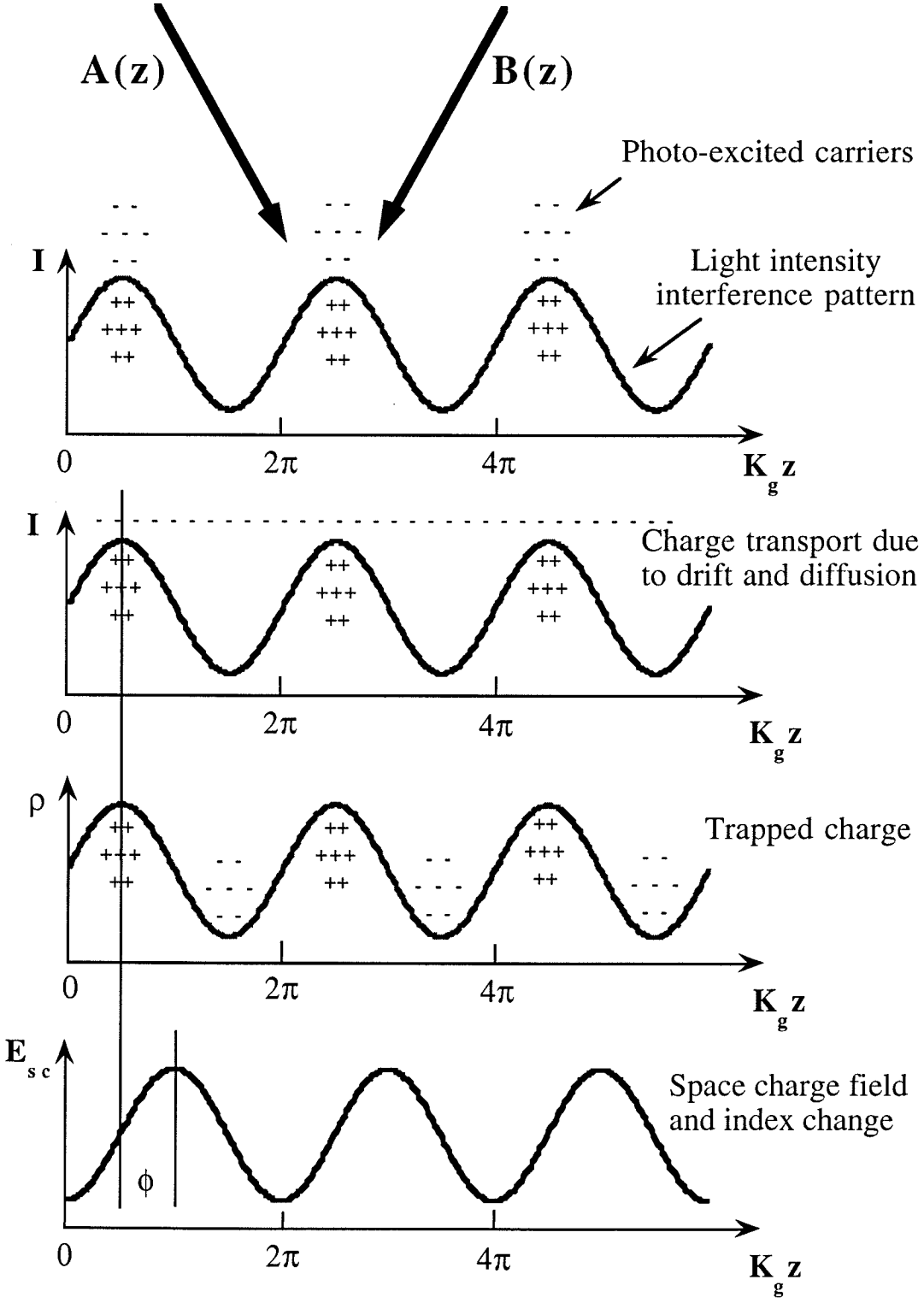
A(z)
B(z)
Photo-excited carriers
I
Light intensity
interference pattern
0
2π
4π
K g z
I
Charge transport due
to drift and diffusion
0
2π
4π
K g z
ρ
Trapped charge
0
2π
4π
K g z
E sc
Space charge field
and index change
ϕ
0
2π
4π
K g z

Figure 2-1

Two coherent monochromatic beams A(z) and B(z) interfere in a photorefractive material. Free carriers are preferentially photoexcited in the bright regions, where they undergo transport. They are repeatedly trapped and re-excited, and are finally trapped in a dark region. The steady-state charge distribution ρ creates a space charge field. In the diffusion limited case the charge modulation is in-phase with the intensity pattern. However, the sinusoidal component of the field is shifted by exactly one quarter of a grating period from the sinusiodal component of the charge distribution, because $\mathrm{div}E = 4\pi\rho/\varepsilon$. Thus the phase between the intensity pattern and the space charge field is equal to $\pi/2$.

The primary types of inorganic materials ussed in photorefractive research include the oxygen octahedra, the sillenites, and certain semiconductors. Some characteristics which are used to distinguish the various materials from one another are the magnitude of the induced index change, the photorefractive phase, the response time, the dark current, and the possibility of fixing the grating.

Barium titanate, potassium niobate, and strontium barium niobate all possess the oxygen octahedra structure and they are widely used in photorefractive research. Barium titanate and SBN:75 possess a strong electrooptic effect at room temperature [1,2]. Potassium niobate is also a good photorefractive material. However, it is difficult to grow monodomain crystals due to growth and poling problems.

2.2 Band Transport Model

The band transport model for photorefractives is based on the photogeneration of mobile charge carriers. The atomic, usually ionic species which generates the charge carriers (the electron donors) must be stable in the crystal in at least two valence configurations. For example, we define the density of this species as N_D. $N_D = N_D^+ + N_D^0$. N_D^0 acts as an electron donor, allowing photoexcitation or thermal excitation of charge to the conduction band and leaving an ionized N_D^+ site behind. The mobile charge can be retrapped at one of the N_D^+ sites, turning it into an un-ionized N_D^0 in the process. At the same time, hole mobility can occur when a hole is photoexcited from an N_D^+ site to the valence band and is retrapped at an N_D^0 site. These processes are illustrated in figure 2-2.

Charge neutrality is preserved by postulating the existence of a number of non-photoactive acceptor sites $N_A = N_D^+$. If no N_A sites existed. the excited charge would always be forced to recombine with the N_D^+ site from which it was photoexcited. This would prevent any net charge transport.

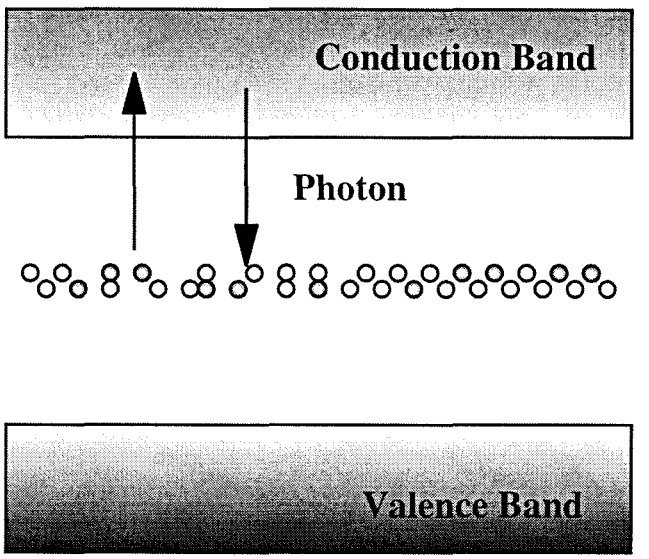

Figure 2-2

The energy diagram for a simple band transport model. A mid band dopant level is occupied with $N_D = N_D^+ + N_D^0$ dopant ions. An electron (hole) is photoexcited from an N_D^0 (N_D^+, open circle) ion by incident photon to the conduction (valence) band where it diffuses and/or drift under and applied field before being retrapped at an N_D^+ (N_D^0, dark circle) site.

The designations N_D^+ and N_D^0 are meant to convey the relative ionization state. In practice, the N_D^0 site is always positively ionized. For example, two stable states of ions are given by Cu^{1+} and Cu^{2+} or Fe^{2+} and Fe^{3+}. In both cases, the less positively charged of the two ionic species acts as the donor while the more positive acts as the trap.

In general, the space charge field is determined theoretically by solving a set of rate equations. If we neglecte the photovoltaic contribution to the charge transport, the rate equations can be solved as follows. Note that electrons are excited into the conduction band at a rate $[\beta_e + s_e I/(h\nu)]$ $(N_D - N_D^+)$, and they combine at a rate $\gamma_e n N_D^+$. Similarly, the excitation rate for holes is given by $[\beta_h + s_h I/(h\nu)]$ N_D^+ and the recombination rate by $\gamma_h p$ $(N_D - N_D^+)$. The variables are defined as:

I,	incident light intensity
$h\nu$,	optical energy of incident photon
β_e (β_h),	thermal generation rate for electrons (holes)
s_e (s_h),	photoexcitation cross section for electrons (holes)
N_D,	density of defect ions
N_D^+,	density of ionized defect ions
N_D^0,	density of un-ionized defect ions
γ_e (γ_h),	recombination rate of electrons (holes)
n,	free electron density
p,	free hole density
j_e (j_h),	total electron (hole) current density
e,	electronic charge
E,	electric field
μ_e (μ_h),	electron (hole) mobility
D_e (D_h),	diffusion coefficient for electrons (holes)
κ_e (κ_h),	photovoltaic coefficient for electrons (holes)
ε,	relative dielectric constant
ε_0,	permittivity of free space
ρ,	total charge density.

The rate equations for electrons and holes are written as:

$$\frac{\partial n}{\partial t} - \nabla \cdot \frac{j_e}{e} = \left(s_e \frac{I}{h\nu} + \beta_e \right)\left(N_D - N_D^+\right) - \gamma_e n N_D^+ \qquad \text{(2-1a)}$$

$$\frac{\partial p}{\partial t} - \nabla \cdot \frac{j_h}{e} = \left(s_h \frac{I}{h\nu} + \beta_h \right) N_D^+ - \gamma_h p\left(N_D - N_D^+\right) . \qquad \text{(2-1b)}$$

The continuity equation is given by

$$\nabla \cdot J = \nabla \cdot J_e + \nabla \cdot J_h = e\frac{\partial}{\partial t}\left(n - N_D^+ - p\right) . \qquad \text{(2-2)}$$

The current equations for electrons and holes are

$$j_e = ne\mu_e E + eD_e \nabla n + \kappa_e s_e \left(N_D - N_D^+\right) I \qquad \text{(2-3a)}$$

$$j_h = pe\mu_h E + eD_h \nabla p + \kappa_h s_h N_D^+ I . \qquad \text{(2-3b)}$$

Equations (2-3a, b) also can be expressed using the Einstein relation eD=kTμ, where T is the temperature. Finally, the Poisson equation gives

$$\nabla \cdot E = \frac{\rho}{\varepsilon\varepsilon_0} = -\frac{e}{\varepsilon\varepsilon_0}\left(n + N_A - N_D^+ - p\right) . \qquad \text{(2-4)}$$

Consider a photorefractive material being illuminated with the intensity pattern:

$$I(x) = I(1 + me^{iKx} + c.c.) , \qquad (2\text{-}5)$$

where m is the modulation index, K is the grating wavevector equal to $2\pi/\lambda_g$ and directed along x. If the intensity pattern is caused by two coherent interfering beams I_1 and I_2, then m is given by $m = (I_1 I_2)^{0.5}/I$, and $I = I_1 + I_2$. When $m << 1$ the spatial dependence of n, p, N_D^+, and E can be approximated by linearized Fourier expansions. We include fundamental terms only in our analysis. In the case of large modulation depth, higher order harmonics of these quantities should be considered [3, 4].

The band transport model simplifies considerably for only a single type and species of charge carrier, usually considered to be the electron. All parameters describing holes in equations (2-1) through (2-4) are set to zero. The photovoltaic contribution is neglected. Then we have:

$$\frac{\partial N_D^+}{\partial t} = \frac{\partial n}{\partial t} - \nabla \cdot \frac{j_e}{e} \qquad (2\text{-}6)$$

$$\frac{\partial}{\partial t}(n - N_D^+) = \mu_e (E \cdot \nabla n + n \nabla \cdot E + \frac{K_B T}{e} \nabla^2 n) \qquad (2\text{-}7)$$

$$\frac{\partial N_D^+}{\partial t} = (s_e \frac{I}{h\nu} + \beta_e)(N_D - N_D^+) - \gamma_e n N_D^+ \qquad (2\text{-}8)$$

$$\nabla \cdot E = -\frac{e}{\varepsilon \varepsilon_0}(n + N_A - N_D^+) . \qquad (2\text{-}9)$$

The solutions of N_D^+, n, E will be expressed in the form of Fourier expansions:

$$N_D^+ = N_{D,0}^+ + \frac{1}{2} N_{D,1}^+ e^{iKx} + c.c. \qquad (2\text{-}10a)$$

$$n = n_0 + \frac{1}{2} n_1 e^{iKx} + c.c. \qquad (2\text{-}10b)$$

$$E = E_0 + \frac{1}{2} E_1 e^{iKx} + c.c. \qquad (2\text{-}10c)$$

Based on the charge neutrality requirement, it is assumed that $N^+_{D,0} - n_0 - N_A = 0$, and $N_D >> N_A >> n_0$ as well as $N^+_{D,1} \sim N_A >> n_1$. A solution for the space charge field can be obtained [5, 6] from these equations:

$$E_{sc} = -im \frac{E_N (E_0 + iE_d)}{E_0 + i(E_N + E_d)} (1 - e^{-t/\tau}) , \qquad (2\text{-}11)$$

where

$$E_N = \frac{eN_A}{\varepsilon K_g} (1 - \frac{N_A}{N_D}) \qquad (2\text{-}12a)$$

$$E_d = \frac{K_B T K_g}{e} . \qquad (2\text{-}12b)$$

E_N is the limiting space charge field, E_d is the diffusion field, and E_0 is the spatially uniform applied field. The time constant τ is given by [7]:

$$\tau = t_0 \frac{E_0 + i(E_{\mu_e} + E_d)}{E_0 + i(E_N + E_d)}, \tag{2-13}$$

where

$$t_0 = \frac{h\nu N_A}{s_e I_0 (1 + \beta_e h\nu / (s_e I_0)) N_D} \tag{2-14}$$

and

$$E_{\mu_e} = \frac{\gamma N_A}{\mu_e K_g}. \tag{2-15}$$

The time constant for approaching the steady-state value of the space charge field is inversely proportional to the incident intensity. When an electric field is applied the response time τ becomes imaginary so that the space charge field amplitude oscillates in time before reaching the steady-state value.

We also consider a material with a single photorefractive species with two charge carriers: both electrons and holes. In KLTN crystals, for example, two charge carriers are present. The dominant charge carrier can be changed by heat treatment. A detailed discussion of thermal processing

of crystals is presented in chapter three and four. Equations (2-1) through (2-5) apply in this case. The solution for the space charge field has been obtained in the steady state with no applied field [8, 9, 10]:

$$E_{sc} = imE_N \frac{E_d(\sigma_h - \sigma_e)}{(E_d + E_N)(\sigma_h + \sigma_e)}, \qquad (2\text{-}16)$$

where σ_e and σ_h are electron and hole conductivities and are given by [11]:

$$\sigma_e = ne\mu_e = \frac{e\mu_e s_e I_0}{h\nu\gamma_e}\left(\frac{N_D}{N_D^+} - 1\right) \qquad (2\text{-}17)$$

$$\sigma_h = pe\mu_h = \frac{e\mu_h s_h I_0}{h\nu\gamma_h}\left(\frac{N_D}{N_D^+} - 1\right)^{-1}. \qquad (2\text{-}18)$$

In the special case in which the electron and hole conductivities are equal, no steady-state space charge field can be produced. Whenever the hole mobility is nonzero, the space charge field given by (2-17) will be smaller than that predicted by the single charge carrier solution (2-11).

2.3 Two Beam Coupling

When two beams interfere in a photorefractive material they create a space charge field. The space charge field modifies the index of refraction of the material via the electro-optic effect. The index ellipsoid is modified by an amount:

$$\Delta\beta_{ij} = \Delta\left(\frac{1}{n_{ij}^2}\right) = r_{ijk}E_k + g_{ijkl}\varepsilon_0^2(\varepsilon_k - 1)(\varepsilon_l - 1)E_kE_l \ , \quad (2\text{-}19)$$

where $\Delta\beta_{ij}$ are the electric field induced changes in the "axis lengths" of the index ellipsoid, and n_{ij} are the components of the index of refraction tensor. r_{ijk} and g_{ijkl} are components of the linear and quadratic electro-optic tensors, respectively. ε_i is the dielectric constant and E_i is the electric field along the axis i.

In general, r_{ijk} is nonzero in a non-centersymmetric material. The quadratic electrooptic coefficients are usually much smaller and can be neglected in these materials. Consider a simple case in which the space charge field is directed along the c axis of a photorefractive crystal. Equation (2-19) then reduces to:

$$\Delta\left(\frac{1}{n_{ij}^2}\right) = r_{ij3}E_{sc} \quad (2\text{-}20a)$$

$$\Delta n_{ij} \cong -\frac{n_0^3}{2}r_{ij3}E_{sc} \ , \quad (2\text{-}20b)$$

where n_0 is the nominal index of refraction with no applied field, and the relation $\Delta(1/n^2) = -(1/n^3)\Delta n$ has been used. The tensor element "3" corresponds to the c axis.

The linear electro-optic coefficient is required to be zero in a centrosymmetric material. The quadratic electro-optic coefficient is

nonzero in all materials, although it may be small. If the space charge field is directed along the c axis and an external field E_0 is applied along the same axis, then we have $E_3 = E_{sc} + E_0$. The change in the refractive index is given by:

$$\Delta n_{ij}(E_0 + E_{sc}) - \Delta n_{ij} E_0 = -\frac{n_0^3}{2} g_{ij33} \varepsilon_0^2 \varepsilon_3^2 ((E_{sc} + E_0)^2 - E_0^2) \ . \tag{2-21a}$$

The Bragg matched part of the index grating is

$$\Delta n_{ij} = n_0^3 g_{ij33} \varepsilon_0^2 \varepsilon_3^2 E_{sc} E_0 \ . \tag{2-21b}$$

This result indicates that the Bragg matched contribution to the index grating in a centrosymmetric crystal is present only with, and is proportional to, an applied electric field. The relative dielectric constant also plays an important role in the index grating. For example, in a paraelectric material the relative dielectric constant obeys the Curie-Weiss law and near the Curie temperature ε can reach values as high as 10^5 [12].

When an external field is applied, the large dielectric constant can lead to large index gratings. If the external applied field varies in time, the photorefractive response is modulated. This has been demonstrated in KTN and KLTN at frequencies up to 20 kHz [12, 13].

The phase of the index grating is typically shifted with respect to the intensity grating (formed by two interfering beams) by a nonzero amount

[14]. This leads to energy transfer between the two incident beams. The energy coupling enables several applications, including the amplification of a weak signal beam by a pump beam as well as optical signal processing. Beams coupling in a thick material can be described by the coupled mode equations derived from the wave equation. This analysis was first performed by Kogelnik [15].

Consider two coherent optical beams [16]:

$$E(r)=\frac{1}{2}A(r)e^{-i\vec{k}_1\cdot\vec{r}\hat{e}_1}+\frac{1}{2}B(r)e^{-i\vec{k}_2\cdot\vec{r}\hat{e}_2}+c.c.\,, \qquad (2\text{-}22)$$

where $\vec{k}_1$, $\vec{k}_2$, and $\vec{e}_1$, $\vec{e}_2$ are polarization and propagation directions of the two beams. The polarizations are taken to be parallel. The beams propagate in a medium with a spatially modulated index grating

$$n(r)=n_0+\frac{n_1}{2}\cos[\vec{K}\cdot\vec{r}+\phi]\,, \qquad (2\text{-}23)$$

where ϕ is the net shift in phase between the index grating and the intensity grating. The beams obey the scalar wave equation:

$$\nabla^2E+\omega^2\mu\varepsilon(r)E=0 \qquad (2\text{-}24)$$

$$\nabla^2E=\frac{1}{2}(-\vec{k}_1^{\,2}A-2i\vec{k}_1\frac{dA}{dr_1})e^{-i\vec{k}_1\vec{r}}+\frac{1}{2}(-\vec{k}_2^{\,2}B-2i\vec{k}_2\frac{dB}{dr_2})e^{-i\vec{k}_2\vec{r}}\,. \qquad (2\text{-}25)$$

The paraxial approximation of

$$\frac{d^2A}{dr^2} << k\frac{dA}{dr} \quad ; \qquad \frac{d^2B}{dr^2} << k\frac{dB}{dr} \tag{2-26}$$

are used to obtain (2-25). The high frequency dielectric constant is given by

$$\varepsilon(\vec{r}) = \varepsilon_0 n^2(\vec{r}) \approx \varepsilon_0[n_0^2 + \frac{1}{2}(n_0 n_1 e^{-i(\vec{K}\vec{r}+\phi)} + c.c.)] \,. \tag{2-27}$$

Plug (2-25) and (2-27) into (2-24)

$$\frac{1}{2}(-\vec{k}_1^2 A - 2i\vec{k}_1 \frac{dA}{dr_1})e^{-i\vec{k}_1\vec{r}} + \frac{1}{2}(-\vec{k}_2^2 B - 2i\vec{k}_2 \frac{dB}{dr_2})e^{-i\vec{k}_2\vec{r}} +$$

$$\omega^2\mu\varepsilon_0[n_0^2 + \frac{1}{2}(n_0 n_1 e^{-i(\vec{K}\vec{r}+\phi)} + c.c.)]\times$$

$$[\frac{1}{2}Ae^{-i\vec{k}_1\cdot\vec{r}} + \frac{1}{2}Be^{-i\vec{k}_2\cdot\vec{r}} + c.c.] = 0 \tag{2-28}$$

It is clear by inspection that cumulative power exchange occurs only when

$$\vec{k}_1 - \vec{k}_2 - \vec{K} \approx 0. \tag{2-29}$$

Thus only synchronous terms need to be considered in (2-28). Using $k_i=\omega\mu\varepsilon_0 n_0$ (2-28) simplifies to

$$A(z)\cos\beta = \frac{i\pi n_1}{2\lambda} e^{i\phi} B(z) - \frac{\alpha}{2} A(z) \qquad \text{(2-30a)}$$

$$B(z)\cos\beta = \frac{i\pi n_1}{2\lambda} e^{-i\phi} A(z) - \frac{\alpha}{2} B(z) \qquad \text{(2-30b)}$$

where α is the optical absorption, λ is the wavelength in the medium, β is the half angle of beam incidence inside the material, and z is the distance along the bisector of the beam angles.

2.4 Diffraction from a Fixed Grating

The diffraction observed from the grating (2-30) is relatively easy to determine when the grating has an index modulation of constant amplitude [15]. The diffraction efficiency then simplifies to:

$$\eta = \exp\left(-\frac{\alpha z}{\cos(\beta/2)}\right)\sin^2\left(\frac{\pi n_1 z}{\lambda\cos(\beta/2)}\right). \qquad \text{(2-31)}$$

This equation is used to calculate the index modulation n_1 by measuring the diffraction efficiency. Consequently, the photorefractive space charge field can be determined as well.

It has been mentioned in chapter one that electronic gratings formed by two beams interfering in a photorefractive material are not permanent.

This grating can be erased by illuminating the material with a uniform beam. In order to store optical information in a photorefractive material, a fixing process has been developed and demonstrated in a wide range of materials [17]. The goal of hologram fixing is to transform the electron grating into an optically inactive grating. Two methods which are used to achieve the fixing of holograms are discussed in this thesis. One technique is to heat the photorefractive medium during or after the hologram recording process. The ion mobility increases as the temperature increases so that ions redistribute in a relatively short time under the influence of local space charge fields. The ions are typically optically inactive and can not be displaced by exposure. Another fixing technique is based on ferroelectric domain reversal. If the space charge field is larger than the local coercive field, the polarization of local domain can be switched. This domain grating can extend throughout entire crystal. The grating period can be smaller than one micrometer. It is important to notice that the fixed hologram is 180 degrees out-of-phase with original grating in the first technique and is in-phase in second technique.

2.5 Thermally Assisted Ionic Fixing

Lithium niobate is the most popular material thermally fixing holograms. The first demonstration was done by Amodei and Staebler in 1971 [18]. In their experiment, the lithium niobate crystal was heated to 100 - 200 °C either during or after the hologram recording process. After cooling the material to room temperature, a fixed grating was revealed.

This fixed grating was 180 degrees out of phase with the electronic grating. They reported that at elevated temperatures, the optically inactive species drifts under the force of the local space charge field and tries to compensate it. In the absence of illumination, the electronic charge responsible for the index grating remains trapped even at elevated temperatures. When the crystal is cooled to room temperature in the dark, the optically inactive species are rendered immobile. A uniform light erases the electronic grating and a fixed grating can be revealed.

Several subsequent studies have followed Amodei and Staebler's original work to determine the ionic species reponsible for the fixed grating. Protons have been identified as the mobile ions responsible for fixing in lithium niobate crystal [19]. We have found that copper may reduces proton concentration in KLTN crystals. A. Yariv suggested to reduce the proton concentration in lithium niobate crystal and then to repeat the fixing experiment [20]. The experimental result shows that the similar fixed grating still can be generated even the protons concentration has been reduced by an order. This indicates that a mobile species other than proton is also involved fixing process in lithium niobate crystals.

Thermal fixing has also been demonstrated in $LiTaO_3$ [21], $Bi_{12}TiO_{20}$ [22], $KNbO_3$ [23], KTN [24], and KLTN [25], etc. The largest fixed diffraction efficiency reported in lithium niobate crystal is 98% for a reflection spectral filter [26].

2.6 Ferroelectric Domain Fixing

In ferroelectric materials, the spontaneous polarization exists in every unit cell. The polarization of each unit cell may by directed along one of many possible directions. The poling process is used to align all polarizations along one direction. This enables us to produce a monodomain sample. Chapter three gives a detailed discussion of the poling process for KLTN crystals.

Photorefractive space charge fields can produce both a poling field and a depoling field in a monodomain crystal. When the space charge field is in the same direction as the spontaneous polarization it is a poling field, otherwise it is a depoling field. The story happens in depoling regions since the space charge field may cause spontaneous polarization to invert in some unit cells depending on the strength of the space charge field and the local coercive field. This results in the formation of a polarization grating in-phase with the electronic grating. After erasing the electronic grating, the polarization grating caused by local domain reversal remains in this configuration as long as certain conditions are satisfied (keeping the temperature well below T_C, for example).

Evidence for polarization fixing can be traced back to the early work on optical damage. Ashkin et al. observed antiparallel domains in $BaTiO_3$ following the illumination of an initially poled crystal [27]. Rudyak reported the optical generation of needle shaped 180 degree domains in $LiNbO_3$:Fe following illumination with a single beam at 440 nm, at room

temperature. These experimental observations suggest that the interaction of light and domains is indeed a common phenomenon shared by many photoferroelectrics. Fixing of volume holograms in both SBN and $BaTiO_3$ in the head to head domain configuration has been demonstrated during the early work on volume holographic memories [28-30] and has been confirmed by later work [31,32]. A. Kewitsch published a series of papers regarding ferroelectric domain fixing in SBN [33]. More recently, KLTN has been shown to exhibit ferroelectric domain fixing [25, 34]. In general, the crystal need not be heated to high temperatures in ferroelectric domain fixing as in thermal fixing.

2.7 Summary

The band transport theory of the photorefractive effect was discussed. Photorefractive rate equations were introduced and solved to yield the photorefractive space charge field magnitude and phase. The electronic grating in a photorefractive crystal only persists for a short time and can be erased by illumination. To develop these grating into permanent replicas, a fixing process must be applied. Fixing has been achieved in a large number of ferroelectric crystals and in some paraelectric crystals over the past three decades. Thermal fixing and ferroelectric domain fixing are two techniques which are used in these crystals. Thermal fixing requires elevated temperatures to heat the crystal. Ferroelectric domain fixing requires that the temperature remain well below the Cuire temperature at all times. KLTN has been found to be a good material for

both thermal fixing and ferroelectric domain fixing. This will be discussed later in the thesis.

References for Chapter Two

[1] M. E. Lines, A. M. Glass, Principles and Applications of Ferroelectrics and Related Materials. (Clarendon Press, Oxford, 1977).

[2] M. H. Francombe, Acta Cryst. **13**, 131 (1960).

[3] E. Ochoa, F. Vachss, and L. Hesselink, J. Opt. Soc. Am. B, **3**, 181 (1986).

[4] A. Bledowski, J. Otten, and K. H. Ringhofer, Opt. Lett. **16**, 672 (1991).

[5] N. V. Kukhtarev, V. B. Markov, S. G. Odulov and V. L. VinetskII, Ferroelectrics, **22**, 949, (1979).

[6] K. Sayano, Ph.D. Dissertation, California Institute of Technology, Pasadena, California (1990).

[7] A. Yariv, Optical Electronics, Saunders College Publishing, Philadelphia, (1991).

[8] G. C. Valley, J. Appl. Phys. **59**, 3363 (1986).

[9] M. B. Klein, G. C. Valley, J. Appl. Phys. **57**, 4901 (1985).

[10] M. C. Bashaw, T. P. Ma, R. C. Baker, S. Mroczkowski, and R. R. Dube, J. Opt. Soc. Am. B **7**, 2329 (1990).

[11] G. Rakuljic, Ph.D. Dissertation, California Institute of Technology, Pasadena, California. (1987).

[12] A. Agranat, V. Leyva, and A. Yariv, Opt. Lett. **14**, 1017 (1989).

[13] R. Hofmeister, Ph.D. Dissertation, California Institute of Technology, Pasadena, California. (1993).

[14] V. Kondilenko, V. Markov, S. Odulov, and M. Soskin, Optica Acta, **26**, 239 (1979)

[15] H. Kogelnik, Bell Syst. Tech. J. **48**, 2909 (1969).

[16] A. Yariv, IEEE J. Q. Elec. **9**, 919 (1973)

[17] H. M. Smith, Ed., Holographic Recording Materials, Vol. 20 (Springer- Verlag, Berlin, 1977)

[18] J. J. Amodei, D. L. Staebler, Appl. Phys. Lett. **18**, 540 (1971).

[19] R. Muller, L. Arizmendi, M. Carrascosa, J. M. Cabrera, Appl. Phys. Lett. 60, 3212 (1992).

[20] Private communication, (1994).

[21] E. Kratzig, R. Orlowski, Appl. Phys. **15**, 133 (1978).

[22] S. W. McCahon, D. Rytz, G. C. Valley, M. B. Klein, B. A. Wechsler, Appl. Opt. **28**, 1967 (1989).

[23] X. Tong, M. Zhang, A. Yariv, and A. Agranat, Appl. Phys. Lett. **69**, 3366 (1996).

[24] L. A. Boatner, E. Kratzig, R. Orlowski, Ferroelectrics, **27**, 247 (1980).

[25] X. Tong, R. Hofmeister, M. Zhang, A. Yariv, and A. Agranat, V. Leyva. Opt. Lett. **21**, 1860 (1996).

[26] V. Leyva, G. A. Rakuljic, B. O' Conner, Appl. Phys. Lett. **65**, 1079 (1994).

[27] A. Ashkin, G. D. Boyd, J. M. Dziedzik, R. G. Smith, A. A. Ballman, and K. Nassan, Appl. Phys. Lett. **9**, 72 (1966).

[28] F. Micheron, G. Bismuth, Appl. Phys. Lett. **20**, 79 (1972).

[29] F. Micheron, G. Bismuth, Appl. Phys. Lett. **23**, 71 (1973).

[30] J. B. Thaxter, M. Kestigian, Appl. Opt. **13**, 913 (1974).

[31] Y. Qiao, S. Orlov, D. Psaltis, R. R. Neurgaonkar, Opt. Lett. **18**, 1004 (1993).

[32] R. S. Cudney, J. Fousek, M. Zgonik, P. Gunter, M. H. Garret, D. Rytz, Appl. Phys. Lett. **63**, 3399 (1993).

[33] A. Kewitsch, A. Yariv, M. Segev, Chapter 9, The photorefractive Effect, Ed. D. Nolte, (Kluwer Academic, 1995).

[34] X. Tong, A. Yariv, M. Zhang, A. Agranat, R. Hofmeister, and V. Leyva. Appl. Phys. Lett. **70**, 28 April (1997).

Chapter Three

Properties of Potassium Lithium Tantalate Niobate (KLTN)

3.1 Introduction

KLTN is a new type of crystal which has been developed at Caltech. The motivation behind the crystal growth effort is to develop materials with potential applications to volume holography for the construction of memory systems and computer interconnects. These photorefractive materials should possess three proteries: 1) high diffraction efficiency; 2) methods for permanent fixing of holograms; and 3) control of readout diffraction efficiency by an external electric field. It was found that KLTN has all three properties. Moreover, the study of KLTN itself provides a better understanding of the fixing mechanisms and liquid/solid inferface dynamics during crystal growth.

Crystal growth is introduced in section 3.2. Basically, the growth temperature is a function of the flux composition. High optical quality crystals can be grown by selecting the right temperature. The phase transition point is another parameter that must be considered in order to achieve a convenient operating temperature. The temperature dependence of the dielectric constant was determined from measurements of the low frequency capacitance of the sample. The temperature for which the capacitance peak occurs corresponds to the ferroelectric phase transition

temperature. These measurements are disscussed in section 3.3. In section 3.4, we present a model which explains the liquid/solid interface dynamics during KLTN crystal growth.

3.2 Growth Temperature and Composition

Potassium niobate is one of the most promising photorefractive materials, but it cannot be operated at room temperature in the paraelectric phase because its primary phase transition occurs at 425 °C; and the single crystal exhibits poor optical quality after cooling through 210 °C, upon which a phase transition between tetragonal and orthogonal symmetry occurs. In order to overcome this problem, tantalum was added to partially replace niobium in the crystal. In a preliminary set of experiments at Caltech, potassium tantalate niobate (KTN) crystals were grown [1]. The object was to add enough tantalum to the material to achieve a phase transition at or near room temperature. This condition is desired because the paraelectric photorefractives operate most efficiently about 10 °C above the phase transition. Unfortunately, it was found that in KTN the operating point could not be raised above 220K because the phase transtion becomes first order [2] and the optical quality deteriorates substantially. The additional lithium was found to improve the optical quality of the single crystal[3]. $K_{1-y}Li_yTa_{1-x}Nb_xO_3$ forms a solid solution for all values of x between 0 and 1 [4], and for $y < 0.13$. The crystals have the cubic perovskite structure in paraelectric phase and are readily doped with transition metals.

The Curie temperature increases with increasing niobium concentration [5]. For very small values of the lithium concentration the material undergoes successive phase transition on cooling, from cubic to tetragonal, then orthorhombic, and finally rhombohedral.

The KLTN crystals are grown using the top seeded solution growth method [6-11]. A non-stoichiometric flux containing an excess of potassium carbonate was used since both potassium tantalate and potassium niobate melt incongruently. The pure platinum crucible is placed in the center of the growth furnace and its contents heated and melted together. The molten flux is soaked at a high temperature to ensure thorough mixing. It is then cooled to approximately thirty degrees above the anticipated growth temperature. Meanwhile a seed crystal is attached to a ceramic pulling tube with pure platinum wire, and is lowered into the furnace through an opening at the top. After the seed and pulling tube are allowed to reach the temperature of the furnace (~ 1 hour), the seed is touched to the surface of the flux for about one minute. The seed is then raised to see if melting has occurred, the temperature is dropped two degrees. This process is repeated until the rounded edges of the slightly melted seed transform into a square outline. This indicates that growth has started. The seed is then re-dipped and rotated using a motion described by a triangle wave form (constant accelerating and decelerating). The maximum rate is about 25 rpm.

The seeding temperature is found to depend only on the flux composition. The most important factor is the ratio of tantalum/niobium. The phase diagram for $KNbO_3/KTaO_3$ [12] shows the crystalization

temperatures . We found that only a small change occurs in the presence of trace amount of lithium (~ 2% Mole). Table 3-1 list the ratio of Nb/Ta and seeding temperatures.

Table 3-1

Flux Composition (Nb/Ta)	Seeding Temperature (°C)
30/70	1250
35/65	1241
45/55	1238
50/50	1221
55/45	1197
60/40	1183
65/35	1170
70/30	1153

3.3 Influence of Ta/Nb on Phase Transition

KTN crystals are ferroelectric materials which have a high temperature paraelectric phase and became tetragonal below the Curie temperature T_C.

The low frequency capacitance of the KLTN sample was measured by using a lock-in amplifier (Stanford SR830 DSP) at a frequency of 25 Hz. The temperature dependence of the dielectric constant can be then calculated. The curves of dielectric constant vs temperature exhibit a peak, which roughly coresponds the Curie temperature T_C. The Curie temperature of KLTN is the function of the crystal composition, the most important factor is the ratio of Ta/Nb. Table 3-2 shows the composition and the coresponding Curie temperature for some of the KLTN crystals.

Table 3-2

Crystal Composition (Ta/Nb)		**Curie Temperature (°C)**
0.86	0.13	-143
0.827	0.176	-112
0.777	0.223	-90
0.748	0.29	-40
0.708	0.293	-21
0.644	0.34	5
0.634	0.36	20

The relative dielectric constants versus temperature of a few of KLTN crystals are illustrated in figure 3-1 through 3-3. The composition of these crystals is summarized in table 3-3.

Table 3-3 The flux composition of #180, #201, and #207

Material	#180	#201	#207
K_2CO_3	56.5%	55%	55%
Li_2CO_3	1.5%	3%	3%
Ta_2O_5	11.1%	11.1%	10.3%
Nb_2O_5	25.9%	25.9%	25.4%

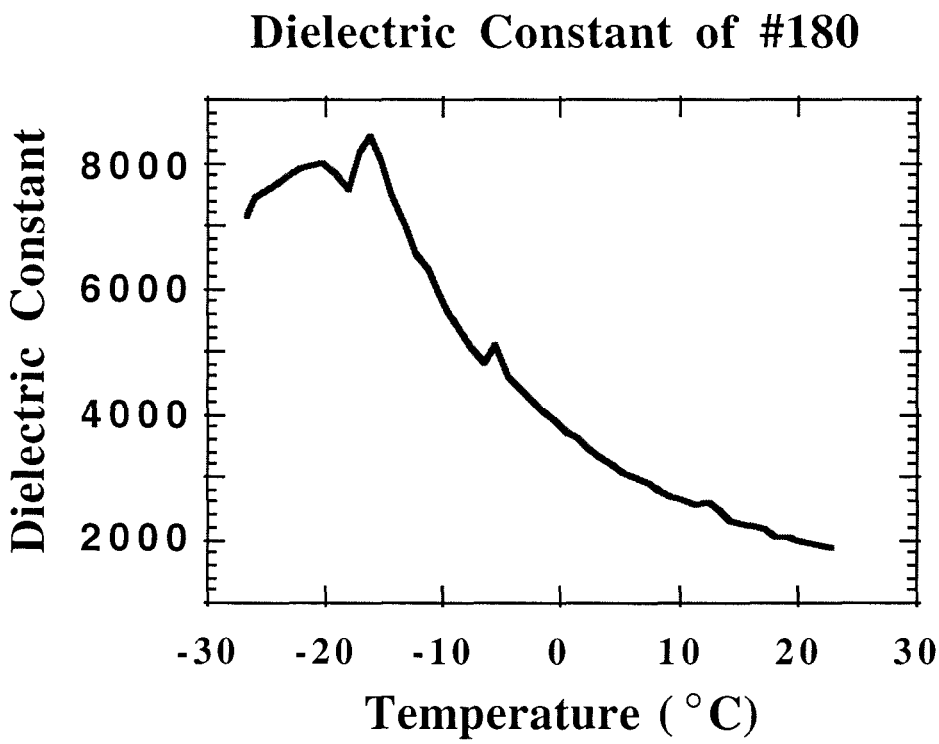

Figure 3-1. The relative dielectric constant versus temperature of KLTN #180. T_C is about -15 °C.

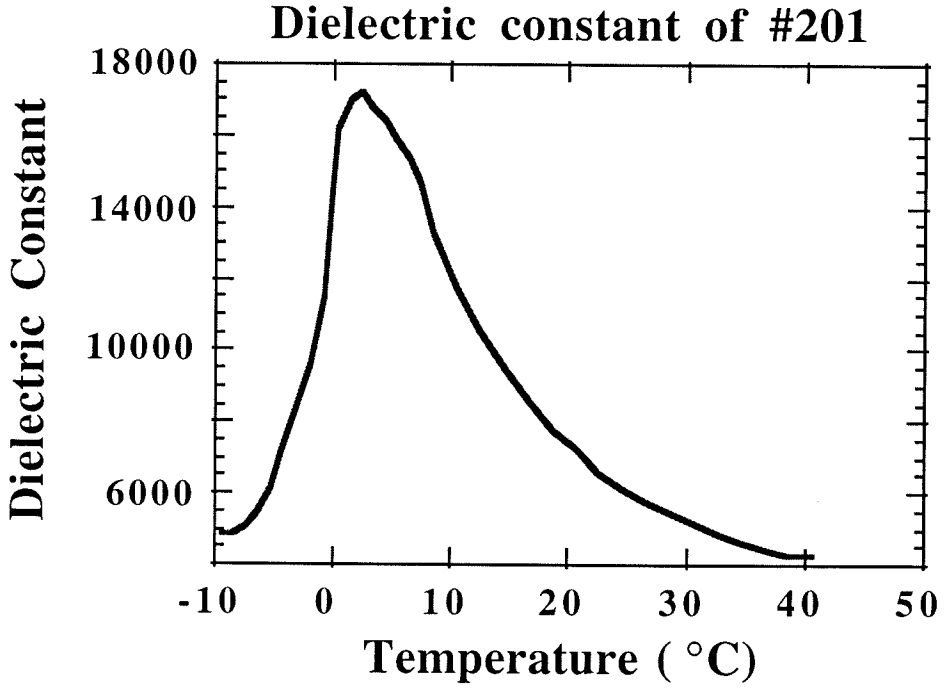

Figure 3-2. The relative dielectric constant versus temperature of KLTN #201. T_C is about -5 °C.

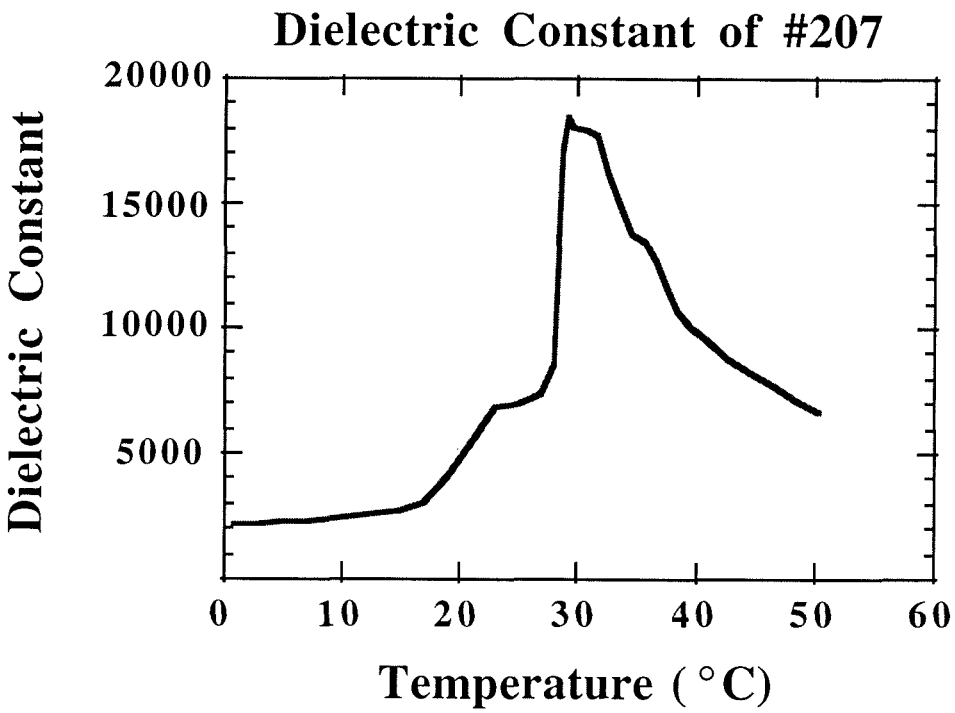

Figure 3-3. The relative dielectric constant versus temperature of KLTN #207. T_C is about 30 °C.

Figure 3-4 shows the dependence of phase transition temperature vs niobium concentration in the flux.

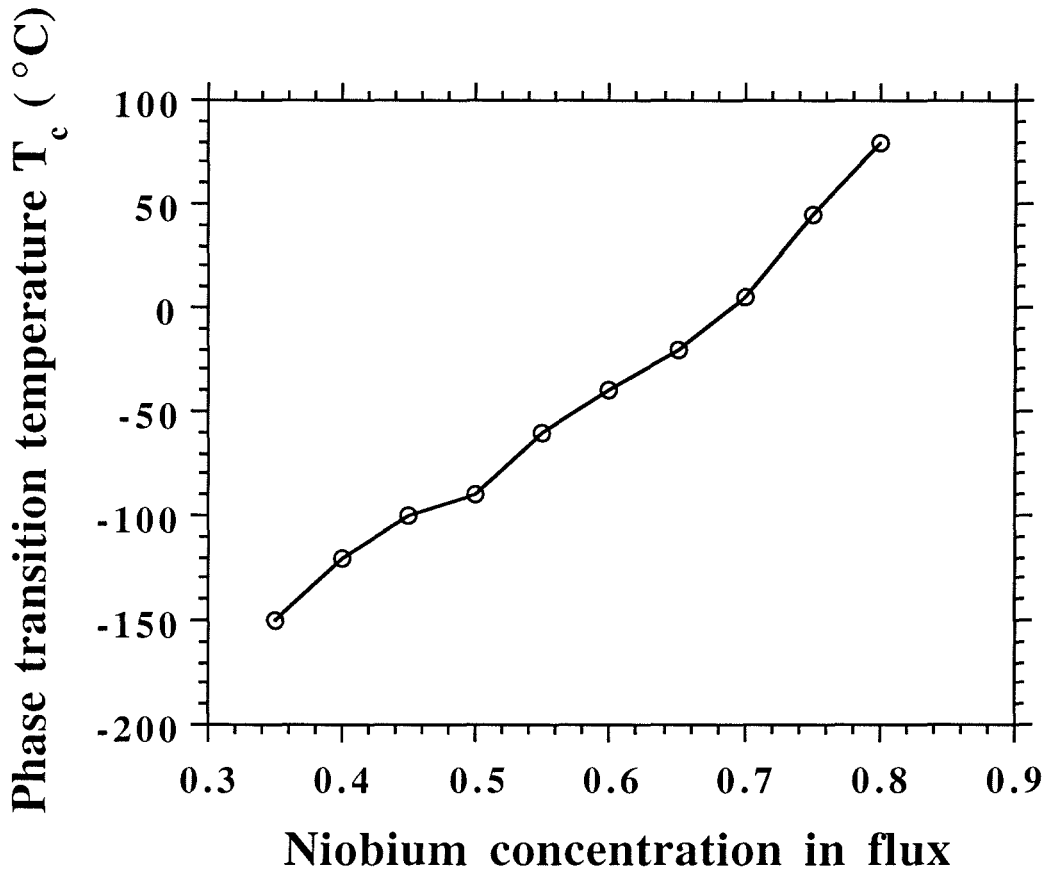

Figure 3-4

The experimental results of the dependence of the phase transition temperature vs niobium concentration in the flux.

3.4 Liquid/Solid Interface Dynamics

Hydrogen ions that are incorporated into "as-grown" crystals have been observed in many ABO_3 type crystals. These crystals include $BaTiO_3$, $LiNbO_3$, $KTaO_3$, $SrTiO_3$ and $K_{1-y}Li_yTa_{1-x}Nb_xO_3$ (KLTN) doped crystals [12-15]. An interstitial proton combines with an adjacent oxygen ion to form an [OH^-] center, giving rise to a stretching-mode absorption in the infrared [16]. The integrated absorption intensity is proportional to the hydrogen concentration. This enables us to compare the hydrogen concentration between different types of crystals or the same type of crystals with different types of dopants. Hydrogen ions that are present in the crystals have a strong influence on the physical properties and applications of these crystals. It is necessary to determine the process by which hydrogen enters the crystals. In a published paper [17] we reported the observation that copper is able to reduce the hydrogen concentration in as-grown $K_{1-y}Li_yTa_{1-x}Nb_xO_3$ (KLTN) doped crystals in the absence of titanium. In the presence of titanium, copper is unable to perform the same role. Here we advance a model for the diffusion of Cu, H, and Ti crossing through the liquid/solid interface during crystal growth. This model describes the mechanism through which the copper reduces the hydrogen concentration in as-grown KLTN doped crystals in the absence of titanium.

All KLTN crystals were co-doped with two to three transition-metal ions. The as-grown crystals were cut to (5-10) x (5-10) x (5-10) mm^3 along the crystallographic axes and polished for the IR absorption spectra measurements. The IR absorption spectra of the stretching vibration of

[OH] were monitored using an FTIR spectrometer(Mattson Instruments Inc. Gl-2020). All spectra were recorded at room temperature. Linearly polarized light was used. The data were averaged over 50 measurements. We observed strong [OH^-] band absorption peaks in most "as-grown" KLTN doped samples except in those doped with Cu and V (Fig.3-5).

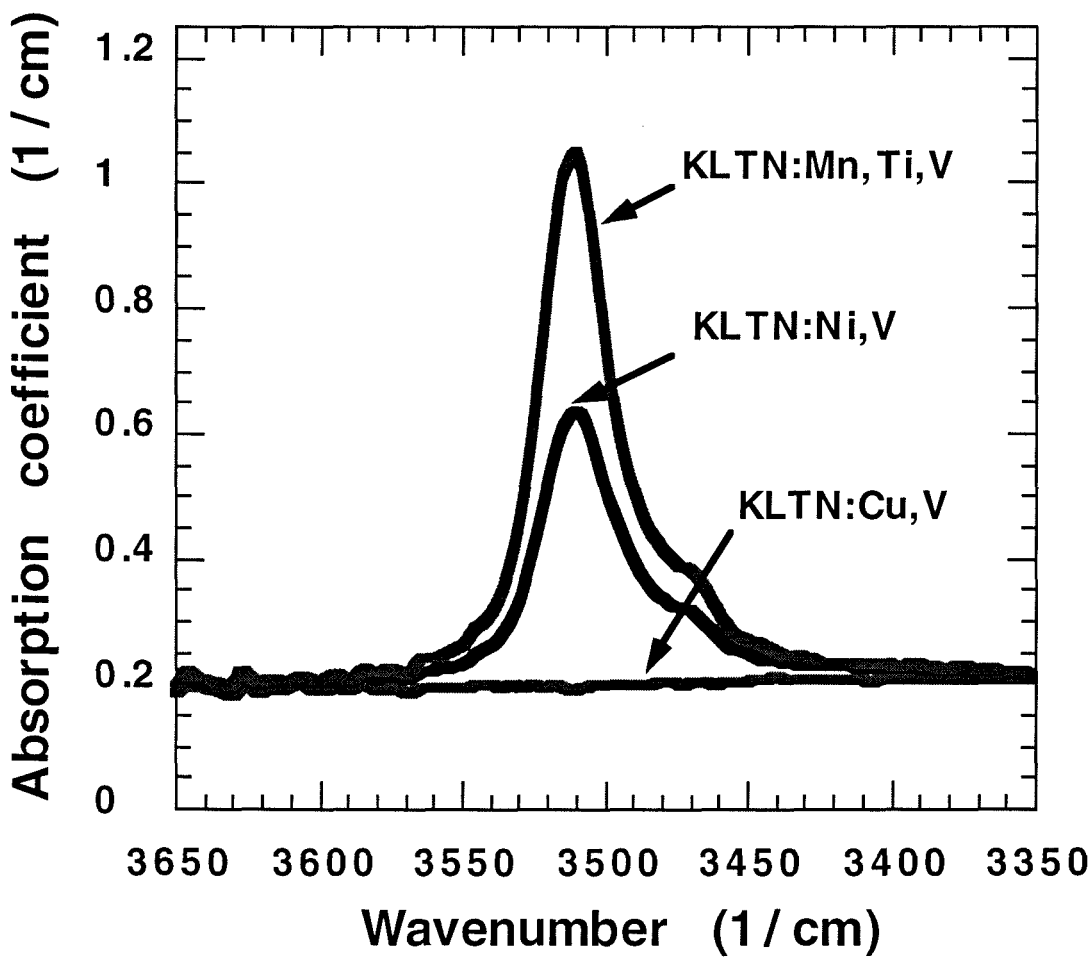

Figure 3-5 (previous page)

The [OH] absorption spectrum of KLTN doped crystals. (a) the top curve is for KLTN: Mn, Ti, V; (b) the middle curve is for KLTN: Ni, V; (c) the bottom curve is for KLTN : Cu, V. The spectrum was obtained using an FTIR spectrometer. Absorption intensity of (a) is about 1.7 times that of (b) between 3450 cm^{-1} and 3550 cm^{-1}. (c) shows no peak.

Comparing the integrated absorption intensity among the as-grown samples, we found that the hydrogen concentration of KLTN:X,Y,Ti samples is always higher than that of KLTN:Cu,X,Ti and KLTN:X,Y by a factor of 1.6 to 2. The last two types of samples had very similar hydrogen concentrations. We noticed that no [OH^-] absorption peak can be observed in KLTN : Cu,X,Y crystals (X,Y are any first row transition metal but not Ti,Cu) between 3450 cm^{-1} and 3550 cm^{-1}. The microscopic mechanism proposed to explain these observations is as follows.

[Cu^+] and [H^+] may occupy the [K/Li^+] vacancy because of a charge neutrality requirement and ionic radii allowance. [Ti^{4+}] + [H^+] may form a [5^+] complex to replace the [Ta/Nb^{5+}] vacant site. [Ti^{4+}] + [Cu^+] cannot form a [5^+] complex because their ionic radius are much bigger than the space allowance inside an oxygen octahedron (Fig. 3-6 next page).

During the crystal growth, [Cu^+] and [H^+] pass through the liquid/solid interface from the solution into the crystal, and they may occupy a [K/Li^+] vacant site or return to the solution (Fig. 3-7), obeying a diffusion equation.

The relevant transport equations are:

$$J_{in}^{H} = \rho^{H} u \qquad (3\text{-}1.a)$$

$$J_{in}^{Cu} = \rho^{Cu} u \qquad (3\text{-}1.b)$$

$$J_{out}^{H} = D^{H} \nabla C^{H} \qquad (3\text{-}2.a)$$

$$J_{out}^{Cu} = D^{Cu} \nabla C^{Cu} \qquad (3\text{-}2.b)$$

$$J_{net}^{H} = J_{in}^{H} - J_{out}^{H} \qquad (3\text{-}3.a)$$

$$J_{net}^{Cu} = J_{in}^{Cu} - J_{out}^{Cu} \quad . \qquad (3\text{-}3.b)$$

$J_{in}^{H}(J_{out}^{H})$ is the current density of hydrogen ions flowing across the interface from liquid(solid) to solid(liquid). Similar quantities are defined for the copper ion. ρ is the concentration in the flux, C is the concentration in the crystal, D is the diffusion constant, and u is the average velocity of the dopant passing through the interface.

$$C_{Vacance}^{K/Li} = C^{H} + C^{Cu} \qquad (3\text{-}4)$$

In the absence of $[Ti^{4+}]$, the $[K/Li^{+}]$ vacancy is the only type of 1^{+} vacancy for both $[Cu^{+}]$ and $[H^{+}]$. Under these conditions, eqn.(3-4) is valid. In equilibrium, the net dopant current density flowing across the liquid/solid interface is zero. This leads to:

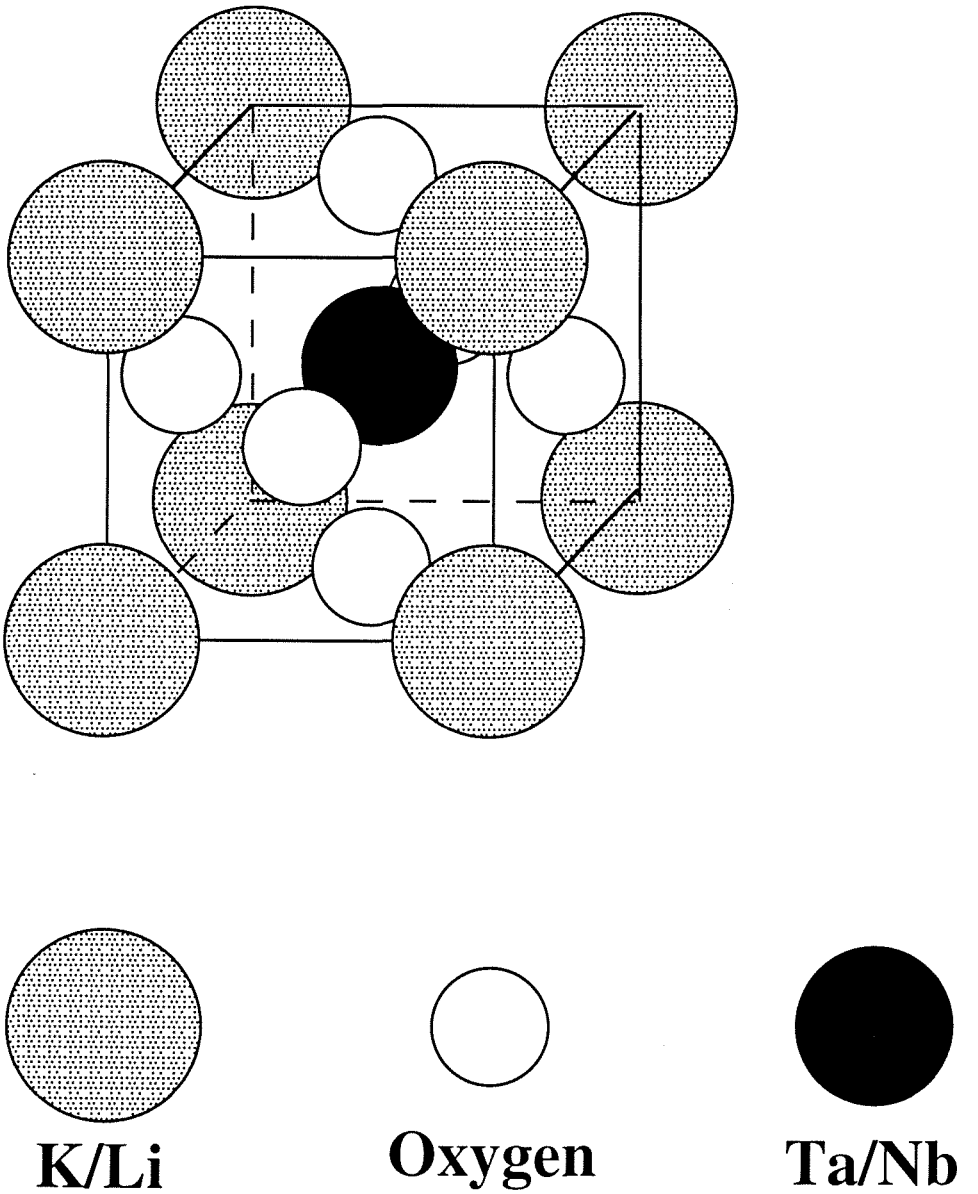

Figure 3-6.

The unit cell of a KLTN crystal. The biggest gray circles, situated at corner sites, are the [K/Li^{+}] ions. The small open circles, located at face center, represent the oxygen ions. The black circle, at the body center, is the [Ta/Nb^{5+}] ion.

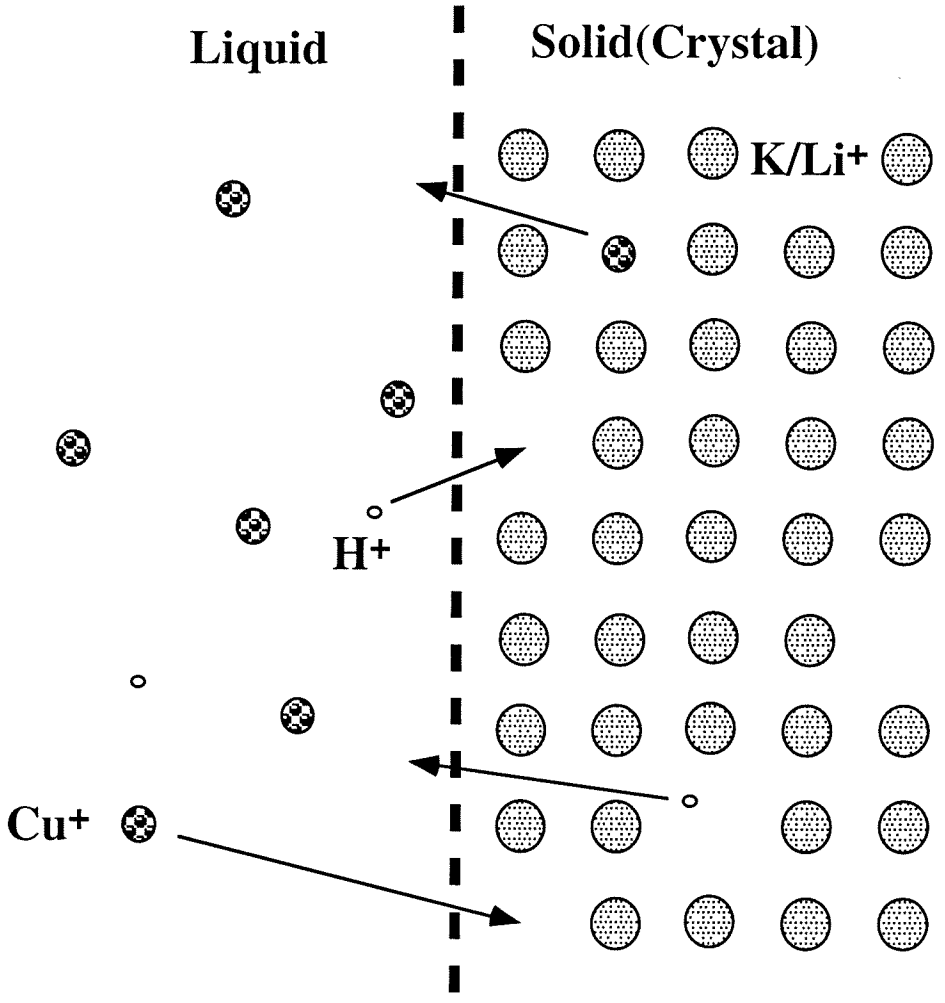

Figure 3-7.

Two dimensional idealized liquid/solid interface. In the absence of $[Ti^{4+}]$, $[Cu^{+}]$ and $[H^{+}]$ may occupy the $[K/Li^{+}]$ vacant site as liquid passes through the interface. $[Cu^{+}]$ and $[H^{+}]$ may also return to the solution from the solid.

$$\rho^{H} u = D^{H} \nabla C^{H} \tag{3-5.a}$$

$$\rho^{Cu} u = D^{Cu} \nabla C^{Cu} , \tag{3-5.b}$$

where

$$D^{H} = D_0^{H} \exp(-\frac{E_A^{H}}{K_B T}) \tag{3-6.a}$$

$$D^{Cu} = D_0^{Cu} \exp(-\frac{E_A^{Cu}}{K_B T}) . \tag{3-6.b}$$

E_A is the activation energy of [H^+] and [Cu^+]. From eqns. (3-5.a) to (3-6.b), we obtain the ratio of the concentration of the [H^+] to the [Cu^+] :

$$\frac{C^{H}}{C^{Cu}} = \frac{\rho^{H} D_0^{Cu}}{\rho^{Cu} D_0^{H}} \exp(-\frac{E_A^{Cu} - E_A^{H}}{K_B T}) . \tag{3-7}$$

In solution, the copper density is about 0.1 mol%, so that the concentration of [Cu^+] is much larger than that of [H^+]. The exact value of the diffusion constant pre-exponential factor of copper is unknown. In general, the copper ion vibrates in the lattice with a zero point energy near 0.05 eV, so that the attempt frequency V is about 10^{13} Hz. The diffusion constant pre-exponential factor $D_0 = Vd^2$ (d=0.399 nm for KLTN crystals), therefore $D_0^{Cu} \approx 1.6 \times 10^{-6}$ m^2/s and $D_0^{H} \approx 2 \times 10^{-9}$ m^2/s [19]. Roughly speaking,

the pre-exponential factor in eqn. (3-7) is near unity. The concentration ratio of $[Cu^{+}]$ to $[H^{+}]$ at a particular temperature will be determined by the activation energies of both the copper and hydrogen ions. We have reported a 0.72 eV activation energy for hydrogen ions [19]. Copper is much heavier and has an ionic radius which is four times larger than that of the proton. The activation energy of copper is about 2 eV [20]. The temperature of the liquid/solid interface during crystal growth was kept between 1100°C and 1180°C. From eqn.(3-7), we have $C^{H}/C^{Cu} \approx 10^{-6}$, so that most of the $[K/Li^{+}]$ vacancies are occupied by copper rather than hydrogen. This explains why no $[OH^{-}]$ absorption peak is observed in FTIR spectra in KLTN:Cu,X,Y crystals.

In the presence of $[Ti^{4+}]$, all of the $[Ta/Nb^{5+}]$ vacancies are accessible to $[H^{+}]$ as discussed above. There are enough hydrogen ions in the crystals and those ions show a specific absorption peak in FTIR spectra. It is important to notice that $[K/Li^{+}]$ and $[Ta/Nb^{5+}]$ vacancies accept hydrogen ions during the crystal growth. Incorporated protons are not stationary but are able to hop from one site to another. Most hydrogen ions are situated close to an oxygen ion as discussed in detail in [19]. The findings of this paper are not limited to KLTN doped crystals. It may apply to other crystal families such as $(K/Li)TaO_3$, $(K/Li)NbO_3$ and KTN etc. For example, no $[OH^{-}]$ observed absorption peak is observed in as-grown SBN crystals because of the lack of a $[Metal^{+}]$ defect site. In $BaTiO_3$ crystals, a $[Ti^{3+}]$ is able to accept a $[H^{+}]$ to form a $[4^{+}]$ complex, so that hydrogen ion is always present in barium titanate.

To examine the interface interaction between hydrogen and copper in $LiNbO_3$ crystals, another experiment was carried out: pure lithium niobate samples were cut from one crystal. Each sample was placed in a silica tube. Each sample was covered by the fine powder of either ZnO, MnO, Fe_2O_3, CoO, or CuO, respectively. These tubes were then placed in an oven and heated from 25°C to 900°C at a rate of 2°C/min. They were maintained at 900°C for 12 hr, and then cooled down to room temperature at a rate of 2°C/min. Following this heat treatment, the integrated [OH^-] absorption intensity of the samples was essentially unchanged except for the CuO sample, which decreased to 10% of original value. This result indicates that similar interface dynamics take place in a lithium niobate crystal.

Other explanations for the experimental results may be considered. For example, at the liquid/solid interface, copper incorporation in the liquid boundary layer may inhibit hydrogen from entering the lattice. In the presence of titanium, the "copper effect" is no longer a dominant factor. Uda and Tiller have given a detailed discussion for lithium niobate crystals [21-23].

3.5 Summary

A technique has been developed for the preparation of high quality crystals of KLTN. The top seed solution growth method is used. The effect of a wide range of compositions as well as different dopants has been

investigated in the growth process of KLTN crystals. We have observed that, hydrogen cannot be observed in the Cu, V doped KLTN crystals. Also, we propose a model to describe the microscopic mechanism for liquid/solid interface dynamics during KLTN crystal growth. Copper and hydrogen ions occupy potassium/lithium vacancy sites during crystal growth because of the charge neutrality requirement. The activation energy of copper ions and hydrogen ions in KLTN crystals is about 2 eV and 0.7 eV, respectively. The result is that the hydrogen ion concentration is about 10^{12} cm^{-3} in KLTN :Cu, X, Y crystals. This density level is lower than the sensitivity of the FTIR spectrometer so that no [OH^-] absorption peak could be observed. In the presence of titanium, hydrogen ions are able to associate with tantalate/niobate vacancy sites, while copper ions are unable to do so. The hydrogen concentration in this case can be 10^{17} cm^{-3} or higher. As a result, a specific [OH^-] absorption peak shows up in the FTIR spectra. This model explains how the hydrogen concentration can be dramatically reduced in KLTN : Cu,X,Y crystals (X,Y are any first row transition metal but not Ti,Cu), in agreement with experimental results.

References for Chapter Three

[1] A. Agranat, V. Leyva, and A. Yariv, Opt. Lett. **14**, 1017 (1989).

[2] J. P. Wilde and L. Hesselink, Opt. Lett. **17**, 853 (1992).

[3] A. Agranat, R. Hofmeister, and A. Yariv, Opt. Lett. **17**, 713 (1992).

[4] M. E. Lines and A. M. Glass, Principles and Applications of Ferroelectricx and Related Materials, Clarendon Press, Oxford (1979).

[5] A. Reisman, S. Triebwasser, and F. Holtzberg, J. Am. Chem. Soc. **77**, 4228 (1955).

[6] V. Belruss, J. Kalnajs, and A. Linz, Matl. Res. Bull. **6**, 899 (1971).

[7] P. A. C. Whiffen and J. C. Brice, J. Crystal Growth, **23**, 25 (1974).

[8] H. J. Scheel and P Gunter, Crystal Growth of Electronic Materials, Elsevier Science Publishers, (1984).

[9] W. A. Bonner, E. F. Dearborn, and L. G. Van Uitert, Am. Ceram. Soc. Bull., **44**, 9 (1965).

[10] J. Y. Wang, Q. C. Guan, J. Q. Wei, M. Wang, and Y. G. Liu, J. Crystal Growth,. **116**, 27 (1992).

[11] S. L. Hou, R. B. Lauer, and R. E. Aldrich, J. Appl. Phys. **44**, 2652 (1973).

[12] V. Leyva, D. Engin, X. Tong, M. Zhang, A. Yariv and A. Agranat, Opt. Lett. **20**, 1319, (1995).

[13] J. Amodei and D. Staevler, Appl. Phys. Lett. **18**, 540 (1971).

[14] S. Kapphan, J. Koppitz, G. Weber, Ferroelectrics **25**, 585 (1980).

[15] H. Iwahara, T. Esaka, H. Uchida, N. Maeda, Solid State Ionics 3/4, 359 (1981).

[16] T.Scherban, A.S. Nowick, L.A. Boatner, and M. M. Abraham, Appl. Phys. A **55**, 324 (1992).

[17] X. Tong, M. Zhang, A. Yariv, A. Agranat, R. Hofmeister V. Leyva, Appl. Phys. Lett. **69**, 479 (1996).

[18] R. Hofmeister, A. Yariv, and A. Agranat, J. Cryst. Gr. **131**, 486 (1993).

[19] X. Tong, M. Zhang, A. Yariv, and A. Agranat, Appl. Phys. Lett. **69**, 3345 (1996).

[20] See, Charles Kittel, Introduction to Solid State Physics, John Wiley & Sons, Inc., 1986.

[21] S. Uda and W. Tiller, J. Cryst. Gr. **121**, 93 (1992).

[22] S. Uda and W. Tiller, J. Cryst. Gr. **126**, 396 (1993).

[23] S. Uda and W. Tiller, J. Cryst. Gr. **129**, 328-361 (1993).

Chapter Four

Infrared Absorption, Dark Conductivity, and Hydrogen Ion Diffusion

4.1 Introduction

Infrared absorption bands due to O-H vibration has been observed in many ABO_3 type crystals which were grown in the open atmosphere. Examples include $BaTiO_3$, $LiNbO_3$, $KTaO_3$, $SrTiO_3$ and KLTN crystals [1-4]. Hydrogen is incorporated into "as-grown" crystals due to defects in crystal structure. Since the interstitial proton associates strongly with an adjacent oxygen ion, [H+] and [OH-] defects are equivalent [5]. An interstitial proton combines with an adjacent crystal oxygen ion to form an [OH-] center, giving rise to a stretching-mode absorption in the infrared. This absorption agrees well with the anharmonic diatomic oscillator model [6, 7]. It was found that the peak-position, bandwidth and polarization dependence of [OH-] dipoles can be affected by changes in crystal composition and doping.

[OH-] absorption accordingly plays a strong role in physical properties of those crystals studied herein; namely KLTN. For instance, the dc conductivity of KLTN crystals is temperature dependent. The activation energy is strongly influenced by hydrogen. The ac conductivity is affected by the Curie temperature T_C but not hydrogen concentration. This indicated that hydrogen is the dominant factor for dc conductivity in KLTN crystals for $270\ K < T < 350\ K$.

Based on the infrared spectra and protonic conductivity measurements, we propose a model of hydrogen ion migration in $K_{1-y}Li_yTa_{1-x}Nb_xO_3$ (KLTN) doped crystals and use it to obtain a theoretical estimate of the diffusion constant pre-exponential factor D_0 that is in reasonable agreement with the experimental result. This model shows that the transition energy of the second and higher overtones of the [OH] vibration can be higher than the activation energy of hydrogen ion migration.

4.2 Heat Treatment

There are a number of ways to change the properties of crystal samples after growth. Heat treatment in controlled atmospheres is widely used for different applications.

Single crystals of doped KLTN were grown using a modified flux technique as discussed in chapter three. All crystals were co-doped with two to three transition-metal ions. Each "as-grown" crystal was cut in three. One was subjected to a reduction treatment, one to oxidation treatment and one was left untreated. The heat treatment was performed to increase (or decrease) the hydrogen concentration in the crystals. The process of reduction is as follows: the samples were placed in a sealed silica tube filled with hydrogen gas under a pressure of 0.25 Atm. at room temperature. The silica tube was then heated from 25 °C to 900 °C at a rate of 2 °C/min. The temperature was held at 900 °C for 12 hr, and then reduced to room temperature at a rate of 2 °C/min.. The same process was

used for oxidation, except that oxygen gas was used instead of hydrogen. After the heat treatment the KLTN samples were carefully polished and Cr/Au electrodes were deposited. For paraelectric phase KLTN crystals, The electrodes were deposited on an arbitrary pair of opposite faces.

4.3 Infrared Spectrum of KLTN Crystals

The IR absorption spectra characteristic of the stretching vibration of the [OH] were monitored using an FTIR spectrometer (Mattson Instruments Inc. Gl-2020). All spectra were recorded at room temperature with linearly polarized light. The IR beam was incident normal to the surface of the sample. All the data were averaged over 50 to 1000 measurements dependent on the signal to noise ratio. We observed strong [OH^-] band absorption peaks in most "as-grown" KLTN doped samples except in those doped with Cu and V (Figures 4-1 through 4-5). The hydrogen concentration in as-grown KLTN crystals could be changed by heat treatment. Compared to as-grown samples, the concentration of [OH^-] was increased by up to 80% by heat treatment in the hydrogen ambient, and it was decreased by up to 40% in the oxygen ambient. Table 4-1 shows the results of the [OH^-] absorption intensity for as-grown, reduction treated, or oxidation treated samples.

The maximum of the [OH^-] absorption band at room temperature was found to lie between 3490 cm^{-1} and 3525 cm^{-1}. These broad bands

have FWHM of 25 cm^{-1} to 50 cm^{-1} indicating a weak interaction of [OH^-] with the neighboring atoms.

Table 4-1

[OH] integrated absorption intensity (cm^{-2}) between 3470 and 3525 cm^{-1} in some of KLTN doped samples

KLTN dopant	[OH^-]						
	Fe, Ti	Cu, V	Cu,Ti	Co, V	Ni, Ti	Cr, V	Mn, Ti
as-grown	83.9	L/N	34.2	79.1	78.5	36.7	72.2
reduction	138.5	small	55.6	155.3	131.9	70.4	137.2
oxidation	44.1	L/N	20.7	44.7	40.8	18.5	33.3

L/N: less than noise

By using a Morse-type potential and the anharmonic oscillator model, the transition frequency between E_0 and E_1 was found to be the 3500 cm^{-1} [6, 7]. Compared to the [OH^-] absorption intensity of as-grown samples, we found that the hydrogen concentration of KLTN : X, Y,Ti samples is always higher than that of KLTN : Cu, X, Ti and KLTN : X, Y by a factor of 1.6 to 2. The last two types of samples had very similar hydrogen concentrations. We noticed that no [OH^-] absorption peak can be observed in KLTN : Cu,X,Y crystals (where X,Y are any first row transition metal but not Ti, Cu) between 3450 cm^{-1} and 3550 cm^{-1}. One explanation is that hydrogen atoms locate close to the center (Ta/Nb) site only in the presence of Ti, and close to the corner (K/Li) site only in the absence of Cu. The microscopic mechanism was explained in the last

chapter for this combination, in general, [Ti^{4+}] + [H^+] may form a [5^+] complex to replace the [Ta/Nb^{5+}] defect site, the [K/Li^+] defect site prefers [Cu^+] to [H^+].

Figures 4-1 through 4-5 illustrate the absorption around 3500 cm^{-1} for KLTN crystals. The shape of curves and the integrated absorption intensity are slightly different from sample to sample.

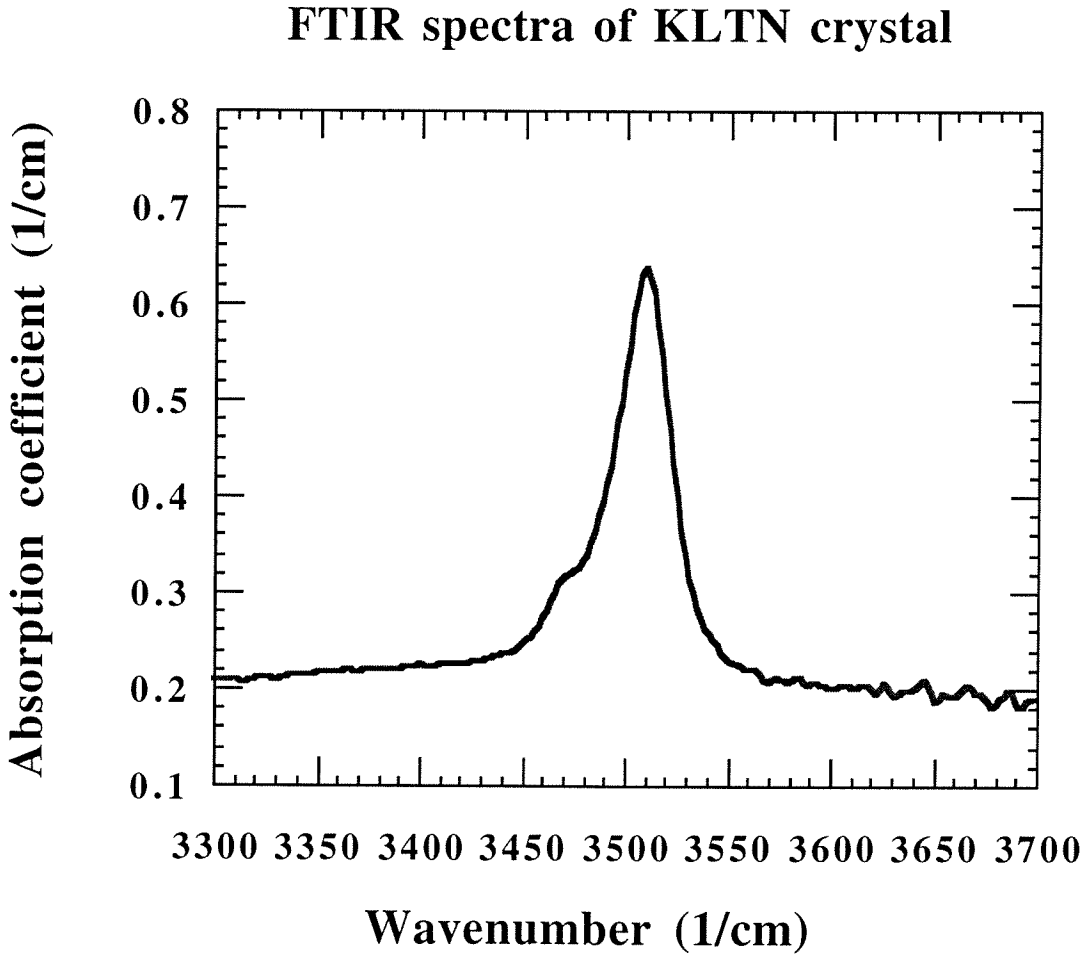

Figure 4-1(previous page)

FTIR spectra of KLTN : Ni, V. A small side band appears on the lower energy side due to the perturbation of neighbor atoms. The color of the crystal is light oval green.

Figure 4-2

FTIR spectra of KLTN : Ti, V, Co. There are two small side bands that can be seen on the lower energy side. This sample is deep red color.

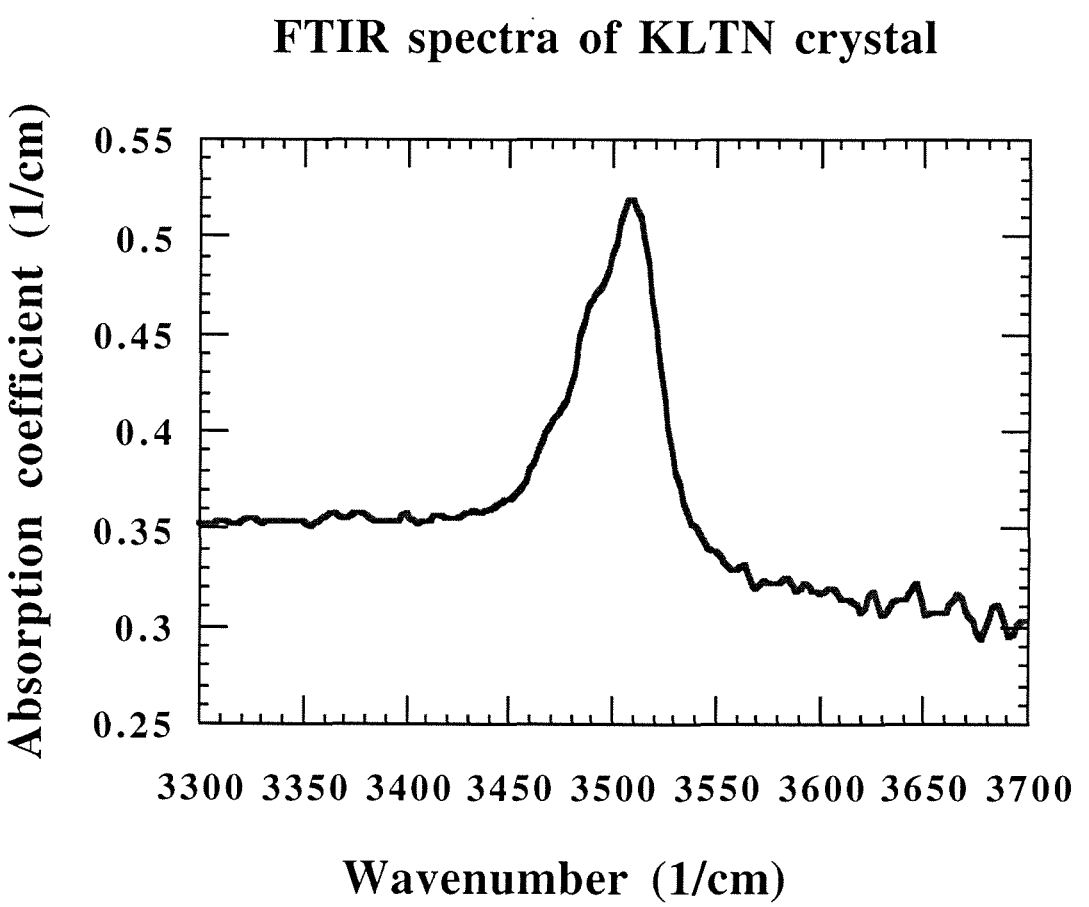

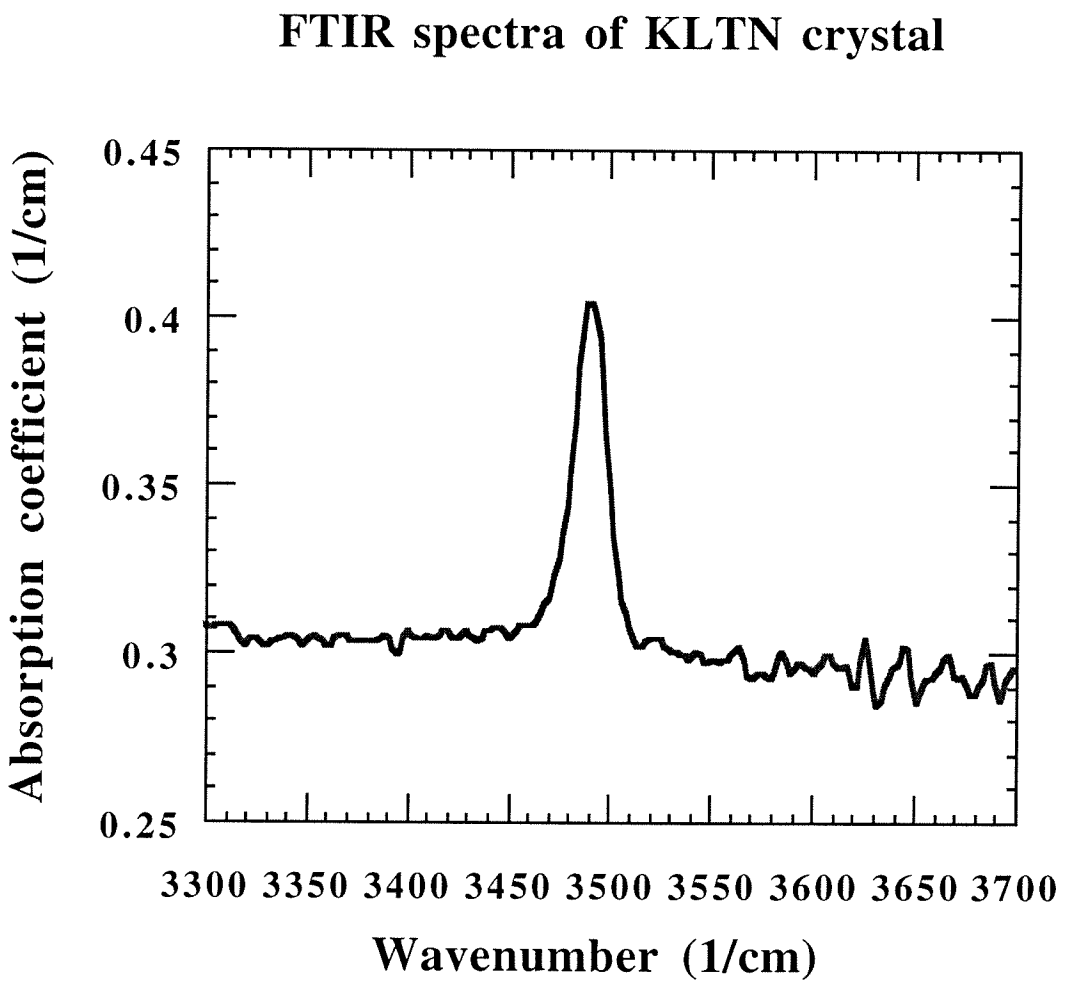

Figure 4-3

FTIR spectra of KLTN : Ti, V, Cu. No side band appears on either lower or higher energy side. The color of the crystal is between green-brown.

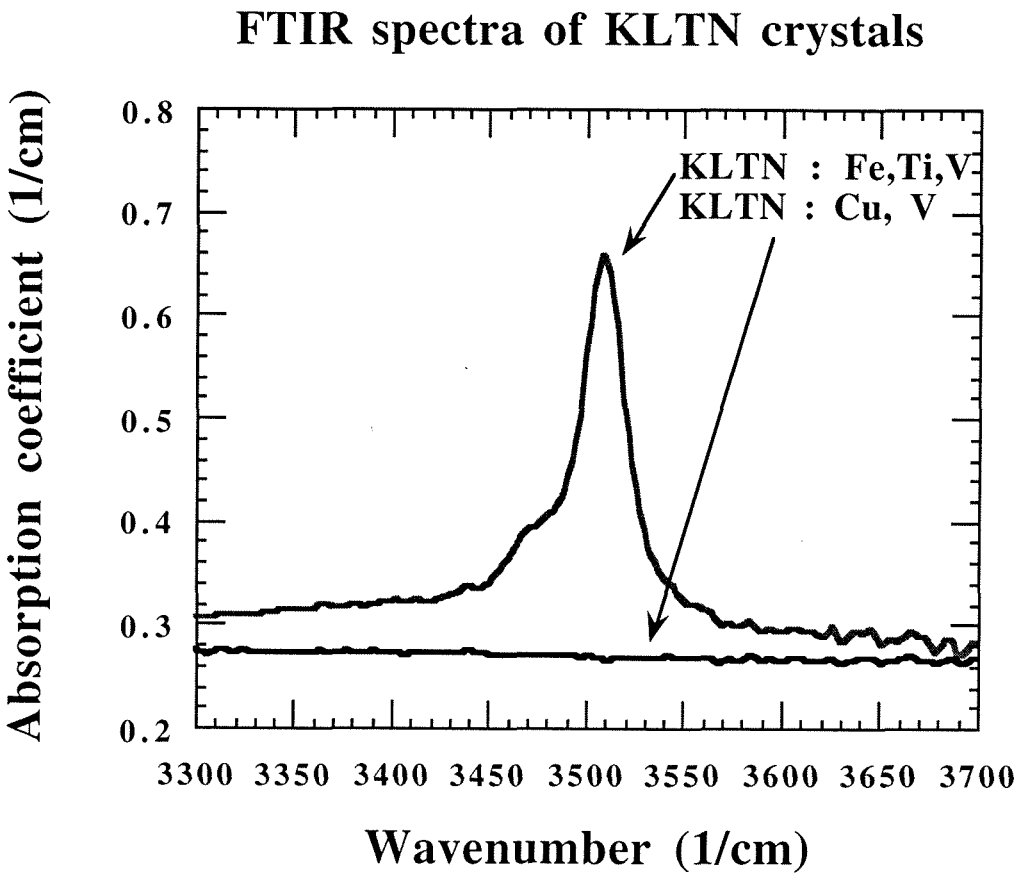

Figure 4-4

FTIR spectra of KLTN doped crystals. No absorption peak is apparent for Cu, V doped samples.

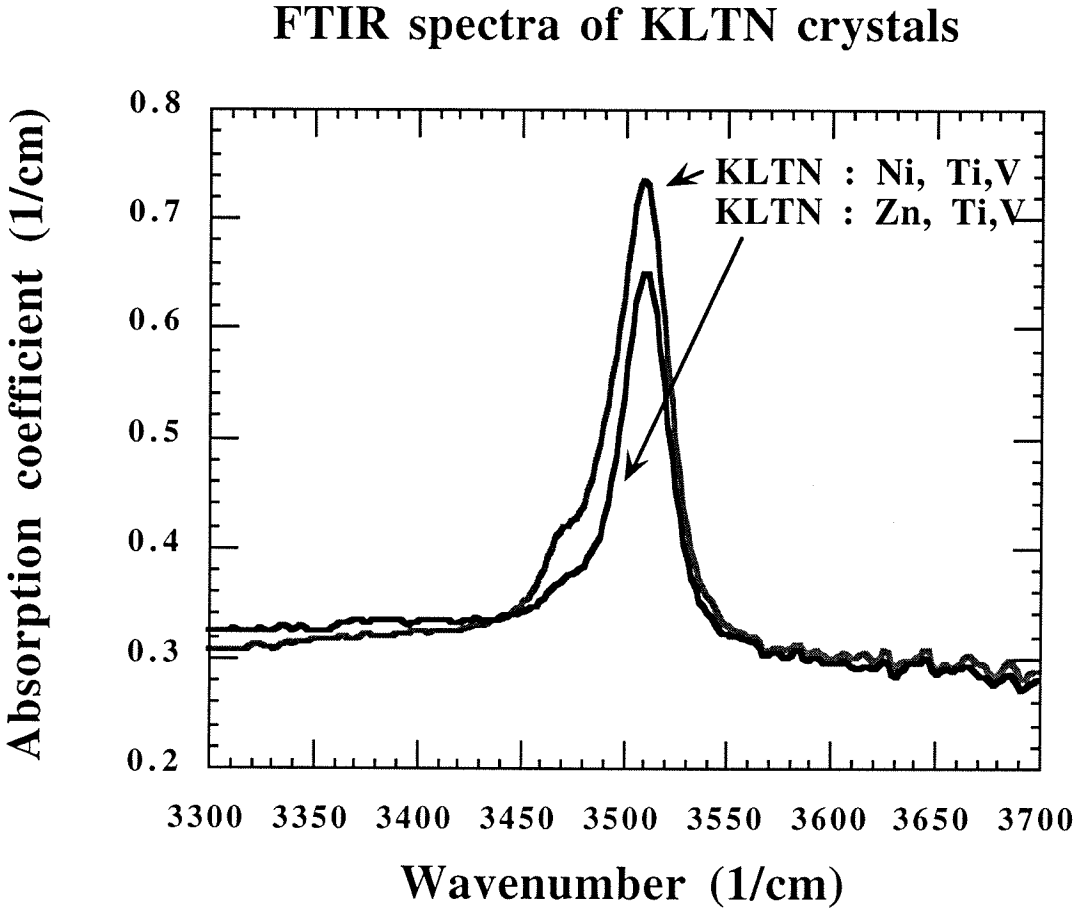

Figure 4-5

FTIR spectra of KLTN doped crystals. The shape of the two curves are slightly different because of compositions and dopant.

The absorption peaks around 4450 cm^{-1} are the combination of vibration plus libration of OH bands. We will explain it later in this chapter. Figures 4-6 through 4-9 exhibit these absorption curves.

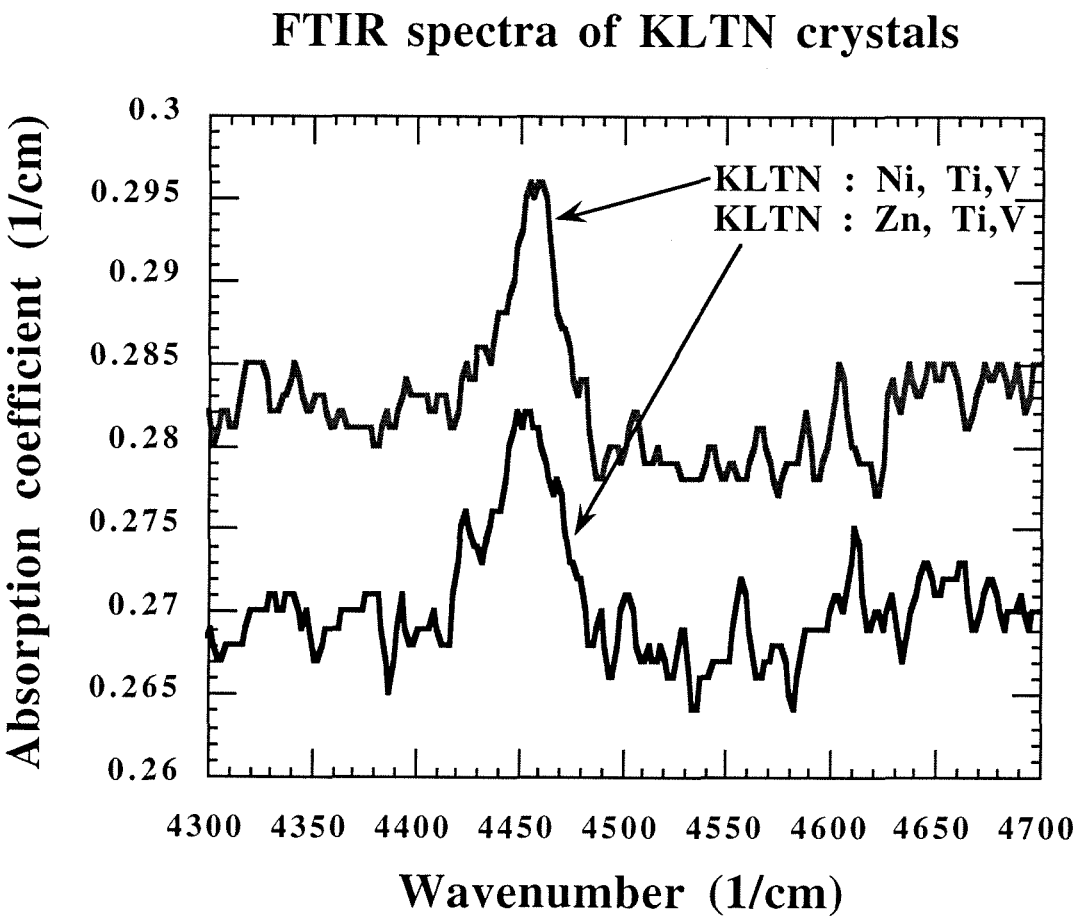

Figure 4-6

FTIR spectra of KLTN doped crystals. These absorption peaks are due to the combination of OH vibration plus libration. It is evidence to support the hydrogen diffusion model which will be presented in the section of 4.5.

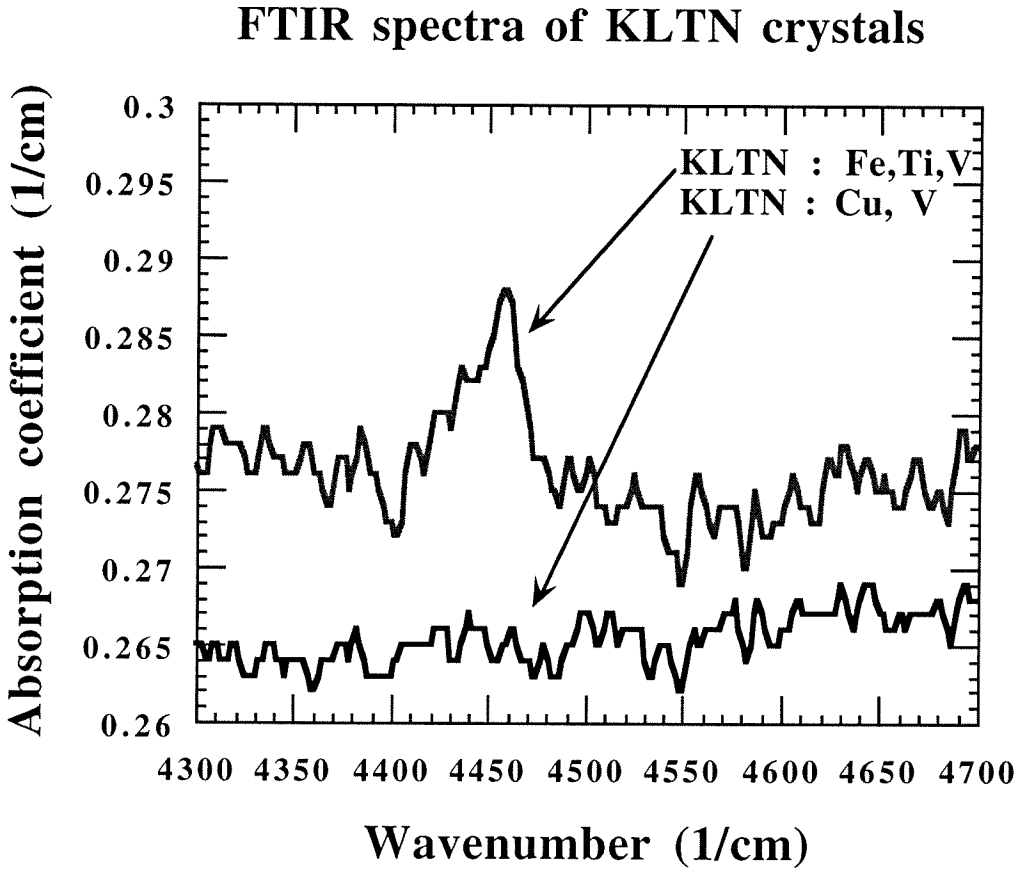

Figure 4-7

The absorption peak of the combination of OH vibration plus libration cannot be observed in KLTN : Cu, V sample.

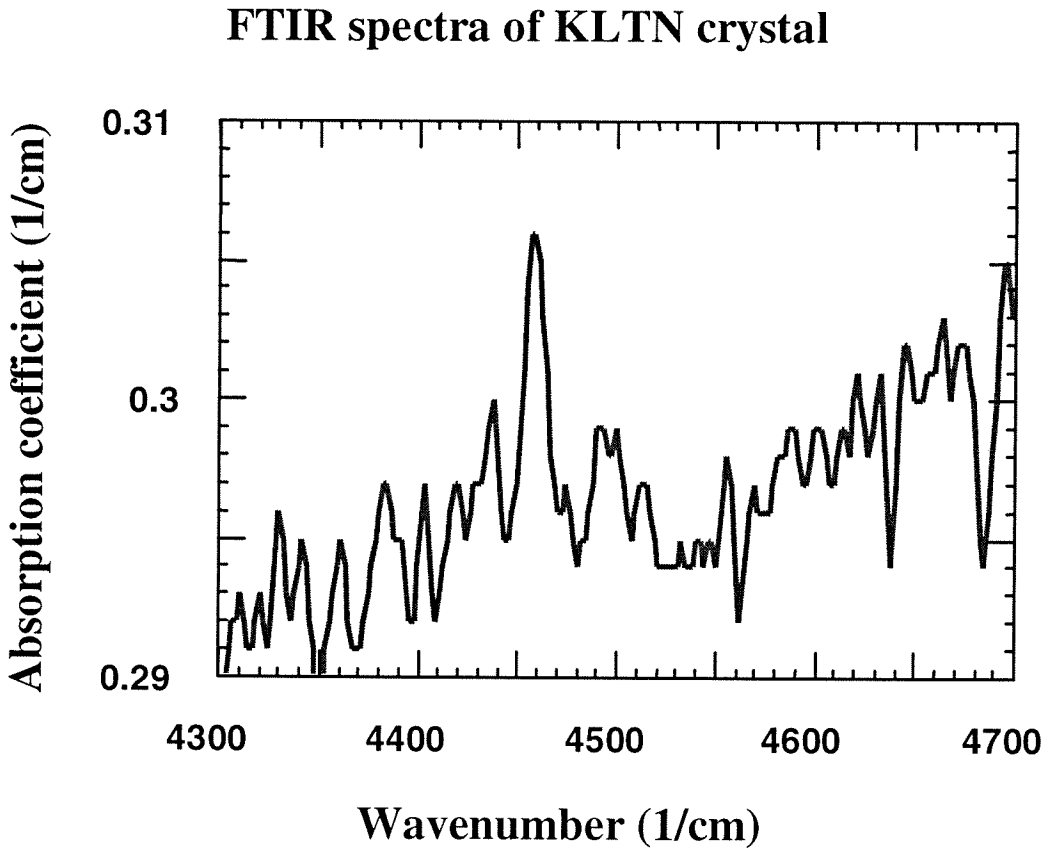

Figure 4-8

FTIR spectra of KLTN : Ti, V, Co.

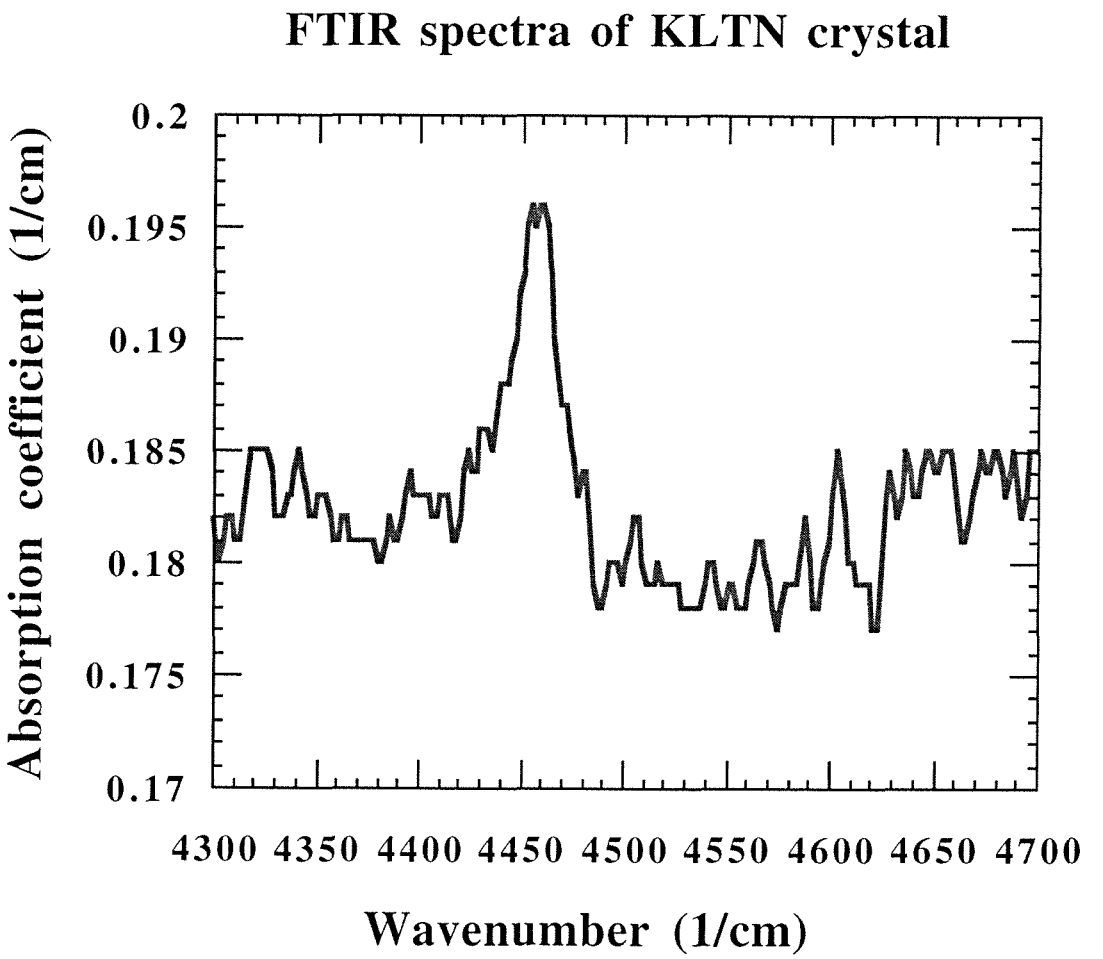

Figure 4-9

FTIR spectra of KLTN : Ni, V between 4300 and 4700 cm^{-1}.

4.4 Dark Conductivity of KLTN Crystals

The ac response of the KLTN sample was measured using a lock-in amplifier at a frequency of 10 Hz. The in and out-of-phase measurements show that the behavior of ac conductivity was determined by the dielectric constant for temperatures between 250 K and 350 K . The in-phase conductivity vs temperature is shown on figure 4-10.

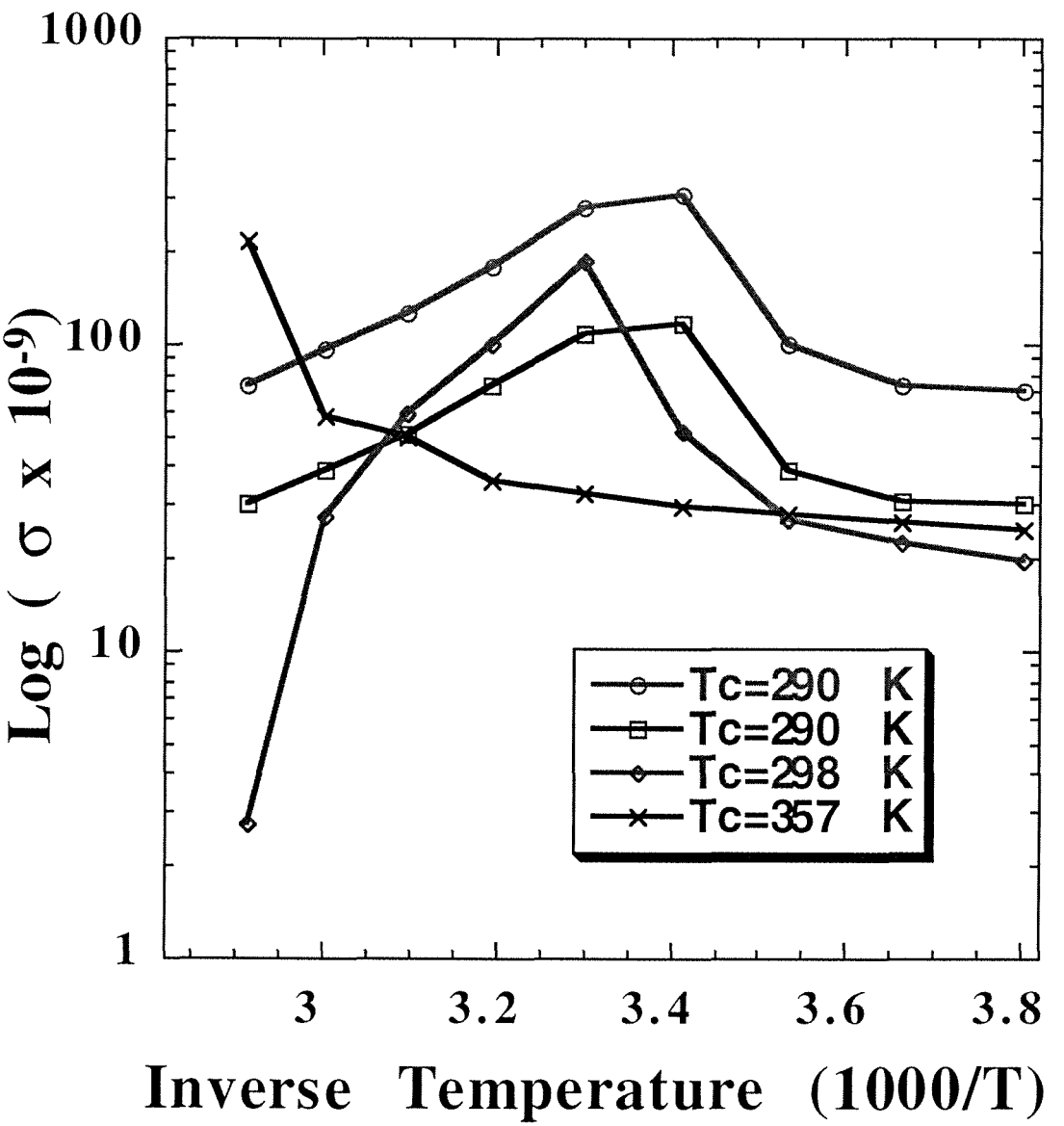

Figure 4-10

Ac conductivity vs. inverse temperature between 260 K and 350 K in KLTN: doped crystals. The broad peak corresponds to the Curie temperature. Typically, the in-phase ac conductivity is about $10^{-8}\ \Omega^{-1}m^{-1}$.

Direct measurements of dc conductivity were performed using a high voltage power supply (Stanford Research System PS350) and a picoammeter (Keithley 485). External voltages less than or equal to 1 KV were applied to avoid voltage break-down. Corresponding to a maximum electric field of 2.5 KV/cm. Dc conductivity was typically near $10^{-13}\ \Omega^{-1}m^{-1}$ (Figure 4-11, next page). Both ac and dc conductivity were measured in vacuum for temperatures between 270 K and 350 K.

The temperature dependence of the dc conductivity showed an Arrhenius-like behavior. Consider the Nernst-Einstein relation:

$$\sigma = \frac{nq^2 D}{K_B T} \tag{4-1}$$

$$D = D_0 \exp\left(-\frac{E_a}{K_B T}\right) \tag{4-2}$$

where n is the concentration of the mobile species, q the charge of the mobile species, D the diffusion constant, and E_a the activation energy.

Figure 4-11

Dc conductivity vs. inverse temperature between 260 K and 350 K in KLTN: doped crystals. The slope of each curve represents the activation energy. For hydrogen ions, it is between 0.6 and 0.7 eV, otherwise the activation energy is about 0.1 eV, attributed by shallow trapped species.

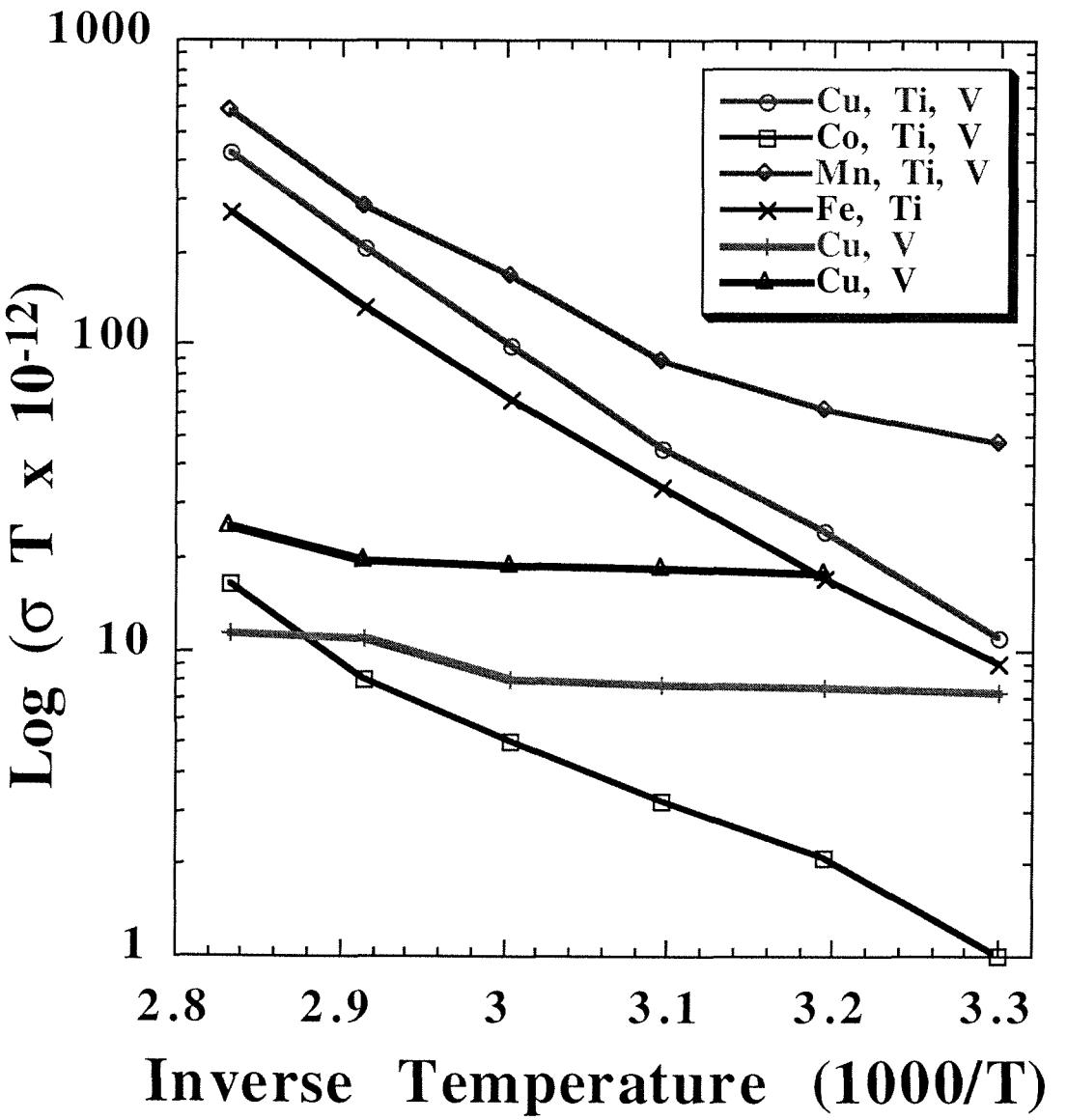

Expressing the conductivity by

$$\sigma = \sigma_0 \exp\left(-\frac{E_a}{K_B T}\right) \qquad (4\text{-}3)$$

$$\sigma_0 = \frac{nq^2 D_0}{K_B T} \,. \qquad (4\text{-}4)$$

The activation energy E_a for ion migration of the samples with [OH^-] absorption peaks was found to be between 0.6 and 0.7 eV, even though the difference of hydrogen concentration among the samples varied by a factor of 4. In the samples which did not possess an [OH^-] absorption peak between 3450 cm^{-1} and 3550 cm^{-1}, the activation energy for the dc conductivity was typically 0.1 eV.

4.5 Hydrogen Ion Diffussion

Hydrogen, which is present in most of ABO_3 type crystals, has a strong influence on the physical properties and applications of these crystals [2,4,8-12]. For example, in KLTN:doped crystals, it affects the thermal fixing of volume phase holograms and the dark conductivity [4, 5]. A detailed understanding of the hydrogen diffusion processes is crucial in a wide variety of contexts. Hydrogen diffusion depends on the specifics of the lattice structure and there is no general model to fit all of the crystals. Bates et al. [13] gave a good but quite complicated interpretation of this

problem in TiO_2 (rutile) with space group D_{4h}. An anisotropic activation energy was calculated, in agreement with experiment. But the librational absorption spectrum which follows from this model could not be verified experimentally. Here we advance a simple model for the hydrogen diffusion process in cubic KLTN:doped crystals and use the infrared spectra and protonic conductivity measurements to characterize the proton motion in the lattice.

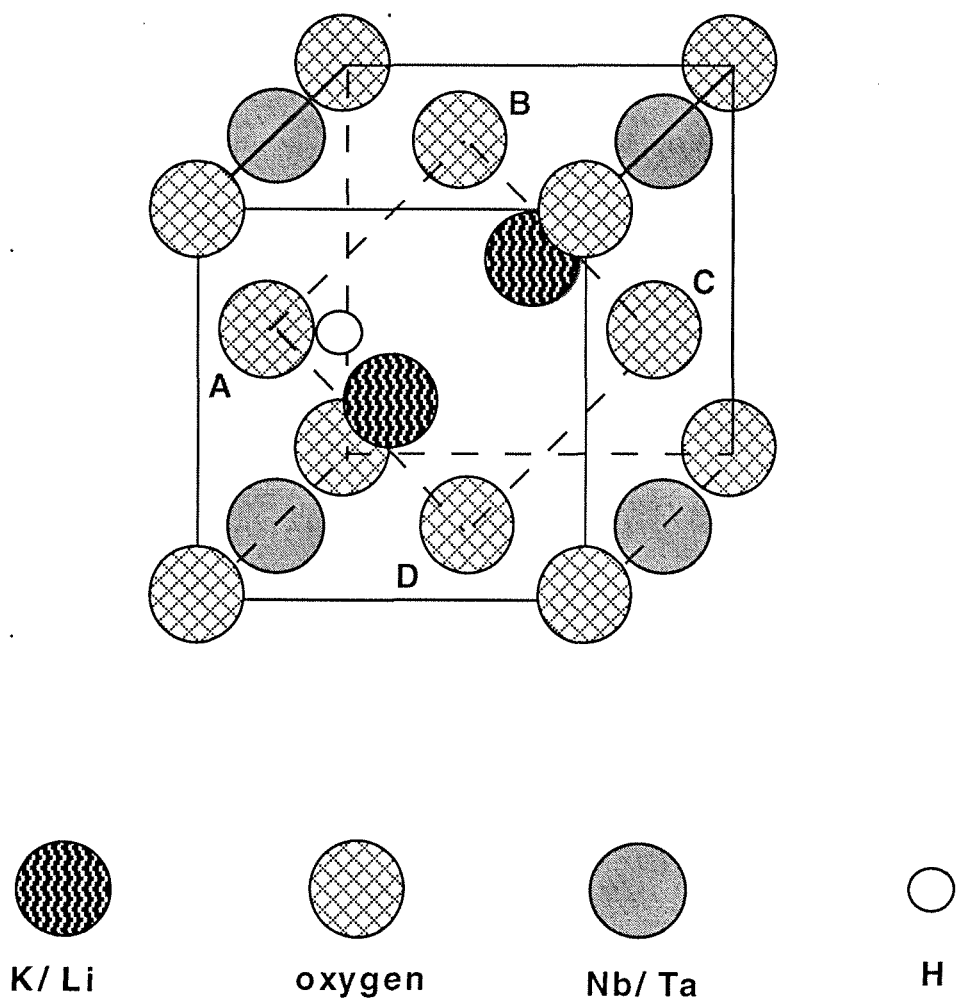

Figure 4-12

Figure 4-12 (previous page)

The cubic cell of KLTN crystal is about 4x4x4 $Å^3$. The small open circle represents a hydrogen ion. It is situated at the site along the two second nearest oxygen ions (A and C) without a Nb/Ta ion in the middle. A proton may appear at the site along the two nearest oxygen ions (AB or AD).

The infrared absorption spectra were obtained using a FTIR spectrometer (Mattson Instruments Inc. Gl-2020) in the range of 2000 - 10000 cm^{-1} with a resolution up to 2 cm^{-1}. The fundamental [OH] stretching vibration absorption peak is at 3512 cm^{-1} in KLTN:Fe,Ti, V with an integrated intensity I_0 = 108 cm^{-2}. The first overtone absorption peak is at 6825 cm^{-1} with integrated intensity I_1 = 0.63 cm^{-2}.

We propose a model in which the hydrogen ion is situated near an oxygen ion (ion A in Figure 4-12, last page) along a line connecting the two second-nearest oxygen ions without a Nb/Ta ion in the middle, that is along the line AC in Figure 4-12. The proton is able to move around (Figure 4-13) not only in the radial direction (vibration; θ is fixed) but also in the azimuthal direction(libration; r is fixed). The dominant contribution potential energy fuction describing the libration comes from the two Ta/Nb ions on both sides of the [OH] band (Figure 4-13). This potential is proportional to the inverse distance between the proton and the Ta/Nb ion. By considering the symmetry of the lattice structure, we use a harmonic oscillator potential to describe the hydrogen libration [14].

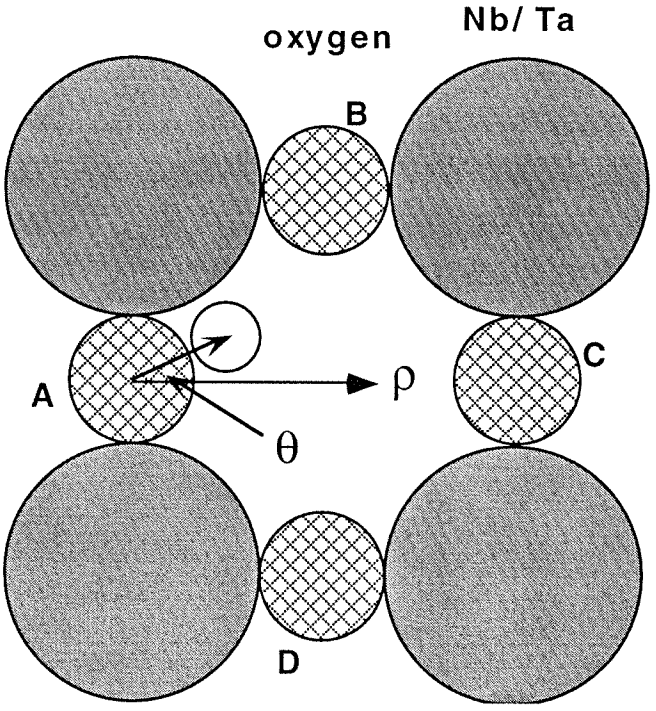

Figure 4-13

The proton (small open circle) is able to move around not only in the radial direction (vibration; θ is fixed) but also in the azimuthal direction (libration; r is fixed). The two motions are treated as independent. Jumping between AB(or AD) gives E_a=0.72 eV, D_0=2.07x10^{-9} m^2/s, in agreement with experimental results.

To first order we neglect the interaction between the vibration and libration and treat the two motions as independent. This is valid because the total potential for hydrogen motions is then the sum of a Morse type vibrational potential V(r) [15,16] and a librational potential V(θ):

$$V(r,\theta) = V(r) + V(\theta) \qquad (4\text{-}5)$$

$$V(r) = D_e(1 - e^{-a(r - r_0)})^2 \ . \qquad (4\text{-}6)$$

Here D_e is the dissociation energy and r_0=0.97 Å is the [OH] equilibrium internuclear distance [15].

$$V(\theta) = \frac{1}{2}\mu_m \omega'^2 r_0^2 \theta^2 \ , \qquad (4\text{-}7)$$

where θ is the angle between the [OH] band and the principal axis of the crystal (Figure 4-13), ω' is the [OH] librational frequency and μ_m the reduced mass of [OH]. The wavefunction of the proton motion and the eigenvalue of the total energy levels are; respectively:

$$\psi_{nl}(r,\theta) = \psi_n(r)\psi_l(\theta) \qquad (4\text{-}8)$$

$$E_{nl} = E_n^r + E_l^\theta \ . \qquad (4\text{-}9)$$

An exact solution of vibration to Schrodinger's equation follows from the change of variables $V(x)=D_e(1-x)^2$. The equation can then be solved in terms of the associated Laguerre polynomials. The resulting vibrational energy levels are given by:

$$E_n^r = hc(\omega(n+1/2) - \omega\chi(n+1/2)^2) \qquad (4\text{-}10)$$

and

$$\omega = \frac{a}{2\pi c}\sqrt{\frac{2D_e}{\mu_m}}, \qquad \omega\chi = \frac{a^2 h}{4\pi^2 c \cdot 2\mu_m}, \tag{4-11}$$

where h is Planck's constant, c the velocity of light and μ_m the reduced mass of [OH]. The measurement of the fundamental and the first overtone of [OH] vibration gives E_{01}/hc=3512 cm^{-1} and E_{02}/hc=6825 cm^{-1},(which corresponds to E_0=0.22, E_1=0.65, and E_2=1.06 eV) and consequently, ω=3711 cm^{-1}, $\omega\chi$=99.5 cm^{-1}. D_e and a were determined to be 4.29 eV and 2.36 $Å^{-1}$, respectively.

The wavefunction and energy levels of libration are [17]:

$$\psi_l(\theta) = N_l \exp(-\beta^2\theta^2/2) H_l(\beta\theta) \tag{4-12}$$

$$\beta = \sqrt{\frac{\mu_m \omega'}{\hbar}} r_0 \tag{4-13}$$

$$E_l^\theta = (l + 1/2)\hbar\omega' . \tag{4-14}$$

$\hbar\omega'$ was determined from the FTIR spectra to be 0.119 eV. N_l is the normalization factor. H is the Hank function in equation (4-12). The ground state probability of a proton in position (r_0,θ) is $P(r_0,\theta) = |\psi_{00}(r_0,\theta)|^2$.

According to Fick's law, the net flux of ions is proportional to the concentration gradient and diffusion constant $D=D_0\exp(-E_a/K_BT)$. The pre-exponential factor D_0 is [13]:

$$D_0 = \nu \bar{d}^2 \qquad (4\text{-}15)$$

where ν is the attempt frequency and $\bar{d}$ the mean "jump" distance. In KLTN crystals, we consider two cases of hydrogen ion hopping:

I) $\theta \sim 0$, the hydrogen ion "jumps" from A to C (Figure 4-13). The attempt frequency ν is 5.3 x 10^{13} Hz (corresponding to a zero point energy 0.22 eV), $\bar{d}$=4 Å, and D_0=8.5x10^{-6} m^2/s, in contrast to the experimental results (Table 4-2), because this jumping hardly happens in KLTN crystals;

II) $\theta > \pi/6$, the proton jumps from A to B (Figure 4-13). The mean distance $\bar{d}$ is 2 Å [11], the probability ratio of $P(r_0,\pi/6)/P(r_0,0)$ is 9.8 x 10^{-4} and the attempt frequency ν = 5.17 x 10^{10} Hz. The pre-exponential factor D_0 in this case is calculated to be 2.07 x 10^{-9} m^2/s, in agreement with experimental results (Table 4-2).

Table 4-2

Comparison of theoretical expected values and experimental results. E_a represents the activation energy of hydrogen, D_0 is the diffusion constant pre-exponential factor. Numbers 1 - 4 represent different samples.

Parameter	Theory	Exp.(#1)	Exp.(#2)	Exp.(#3)	Exp.(#4)
E_a (eV)	0.72	0.65	0.67	0.70	0.75
D_0 (10^{-9}m2/s)	2.07	1.6	2.4	2.5	1.74

The energy barrier for proton hopping over two oxygen ions could be obtained using a double minimum well potential function [19]:

$$V(r) = D_e\{2e^{[-2a(R-r_0)]}Cosh(2ar) - 4e^{[-a(R-r_0)]}Cosh(ar)\}\ , \quad (4\text{-}16)$$

where 2R is the internuclear distance between two oxygen ions, and r is the distance between hydrogen and the center point of the two oxygen ions. In KLTN:doped crystals, the nearest oxygen ions' internuclear distance is about 2.82 Å and that of the second nearest oxygen ions' is 4 Å. The energy barrier between the two nearest oxygen ions (AB or AD in Figure 4-13) is about 0.94 eV, which with a zero point energy of E_0= 0.22 eV results in an activation energy of 0.72 eV .

The energy barrier between the two second nearest oxygen ions (A and C in Figure 4-13) is higher than 2 eV. Comparing both E_a and D_0 to the experimental results, we conclude that the hydrogen hops only between the two nearest oxygen ions.

Direct measurements of protonic conductivity, and consquently the hydrogen ion diffusion constant, were performed at temperatures between 350 K and 270 K. Protonic conductivity was typically near 10^{-13} $\Omega^{-1}m^{-1}$ [12]. The temperature dependence of the protonic conductivity showed an

Arrhenius-like behavior. From the Nernst-Einstein relation (4-1), We can express the pre-exponential factor D_0 by:

$$D_0 = \frac{K_B T \sigma}{nq^2} \exp(\frac{E_a}{K_B T}) . \qquad (4\text{-}17)$$

The proton concentration was calculated from the [OH] band integrated absorption intensity [20].

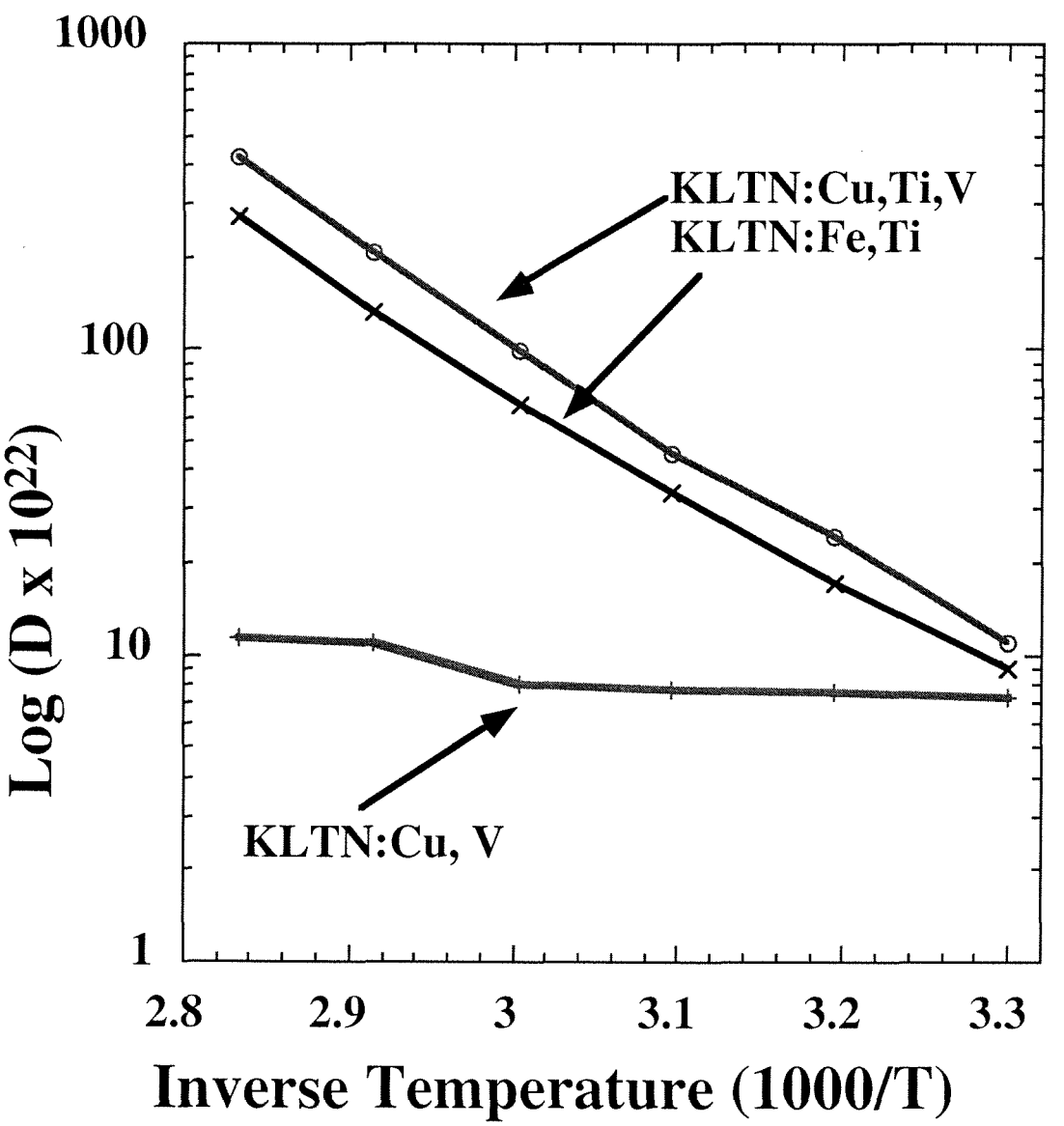

Figure 4-14 (previous page)

Measured temperature dependence of the hydrogen ion diffusion constant between 260 K and 350 K in KLTN doped crystals. The activation energy, proportional to the slope of the curve, is about 0.7 eV for hydrogen ions.

Table 4-2 shows the theoretical and experimental results for activation energy and the diffusion constant pre-exponential factor. Figure 4-14 shows the temperature dependence of the hydrogen ion diffusion constant. Theoretical and experimental results are in good agreement.

4.6 Summary

We found that hydrogen plays an important role on the ionic conductivity in KLTN : doped crystals. In crystals which display an [OH^-] absorption peak around 3500 cm^{-1}, the activation energy for conductivity is between 0.6 and 0.7 eV, otherwise it is 0.1 eV. These results correspond, respectively, to hydrogen and electron migration. Since the holographic ionic grating decay yields an activation energy between 0.67 and 0.76 eV, we believe that hydrogen must be the primary ionic species involved in hologram thermal fixing. Secondly, we observed a strong [OH^-] absorption peak in most KLTN crystals, except those with Cu doping in the absence of Ti co-doping. Hydrogen ions are located near the center site (Ta,Nb) of a single unit cell in the presence of Ti, and near the corner (K/Li) site only in the absence of Cu.

Based on the infrared spectra and protonic conductivity measurements, we propose a model of hydrogen ion migration in KLTN:doped crystals. Hydrogen ions are mostly bounded along a line connecting the two second nearest oxygen ions. Hopping, however, occurs only between the two nearest oxygen ions. Besides the vibration, the [OH] bands also show a librational motion, which can be described by a harmonic oscillator potential. The diffusion model gave the expected value of the diffusion constant pre-exponential factor $D_0=2.07x10^{-9}$ m^2/s, in agreement with the experimental results.

References for Chapter Four

[1] J. Amodei and D. Staevler, Appl. Phys. Lett. 18, 540 (1971).

[2] S. Kapphan, J. Koppitz, G. Weber, Ferroelectrics 25, 585 (1980).

[3] H. Iwahara, T. Esaka, H. Uchida, N. Maeda, Solid State Ionics 3/4, 359 (1981).

[4] V. Leyva, D. Engin, X. Tong, M. Zhang, A. Yariv and A. Agranat, Opt. Lett. 20, 1319, (1995).

[5] T.Scherban, A.S. Nowick, L.A. Boatner, and M. M. Abraham, Appl. Phys. A55, 324 (1992).

[6] G. Herzberg, Molecular Spectra and Molecular Structure I, Spectra of Diatomic Molecules (Van Nostrand, New York, 1950).

[7] A. Grone, and S. Kapphan Ferroelectrics, V125, 307 (1992).

[8] R. Gonzalez, M. M. Abraham, L. A Boatner, and Y. Chen, J. Cham. Phys. **78** 660 (1983).

[9] H. Engstrom, J. B. Bates, and L. A. Boatner, J. Cham. Phys. **73** 1073 (1983).

[10] W. K. Lee, A. S. Nowick, and L. A. Boatner, Solid State Ionics, **18/19**, 989 (1986).

[11] D. M. Smith, Ann. Rev. Mater. Sci. **15** 329 (1985).

[12] X. Tong, M. Zhang, A. Yariv, A. Agranat, R. Hofmeister, and V. Leyva , Appl. Phys. Lett. **69** 479 (1996).

[13] J. B. Bates, J. C. Wang and R. A. Perkings, Phys. Rev. B **19** 4130 (1979).

[14] M. V. Klein, B. Wedding and M. A. Levine, Phys. Rev. **180** 902 (1969).

[15] G. Herzberg, Molecular Spectra and Molecular Structure I, Spectra of Diatomic Molecules (Van Nostrand, New York, 1950).

[16] A. Grone and S. Kapphan, J. Phys. Chem. Solids **56** 5 687 (1995).

[17] A. Yariv, Quantum Electronics (John Wiley & Sons, New York, 1989).

[18] R. Hofmeister, Ph.D. thesis, Caltech (1993).

[19] M. C. Lawrece, G. N. Roberston, Ferroelectrics **25**, 363 (1980).

[20] T.Scherban, A.S. Nowick, L.A. Boatner, and M. M. Abraham, Appl. Phys. A **55**, 324 (1992).

Chapter Five

Thermal Fixing of Volume Hologram in KLTN Doped Crystals

5.1 Introduction

Volume holograms in photorefractive materials are formed by the redistribution of charge carriers which are photoinduced by optical standing waves. This charge distribution induces a space-charge field which causes a refractive index grating due to the linear electro-optic effect. This grating can be converted to a fixed grating composed either of a mobile (at high temperature) non-photoactive species, usually ions, [1-3] or of reversed domains [4-6] which partially compensate the electronic space-charge field. In this chapter only thermal fixing will be discussed. Two of the important issues in hologram fixing are the liftime of fixed grating and diffraction efficiency of developed holograms. In general the thermal fixing requires lower dark electronic conductivity and higher ionic conductivity at elevated temperature. At room temperature the ionic conductivity is very low so that the ionic grating may persist over a relatively long time.

Potassium lithium tantalate niobate ($K_{1-y}Li_yTa_{1-x}Nb_xO_3$, KLTN) is a photorefractive crystal [7-9] with a perovskite structure. The ferroelectric phase transition temperature ranges from 100K to 400K, depending on the K/Li and Ta/Nb ratios. The dominant charge carriers are

either holes or electrons for 514.5 nm wavelength excitation and can be changed by oxidation/reduction treatment.

5.2 Poling Process

The direction of the spontaneous polarization is not the same throughout the as-grown ferroelectric phase KLTN crystals, it may occur along any one of the three crystallographic, leading to six possible directions for the spontaneous polarization. The poling process aligns all of the domains along a single direction.

In our experiments, the ferroelectric phase transition temperature of the sample (KLTN:Co,V,Ti) was determined by monitoring the temperature dependence of the low frequency dielectric constant. The cubic to tetragonal transition occurred at T_C=25 °C for the sample used in the experiment. The sample was 7 x 6 x 2 mm, cut along the crystallographic axes, and optically polished. Ni and then Au were evaporated on the 2 x 6 mm faces. We used a thermoelectric controller to provide a temperature stable mount enclosed in a vacuum chamber. We set the temperature to 35 °C and cooled the sample to 5 °C at a rate of 1 °C/min. Upon cooling through the phase transition, the crystal became opalescent as light scattered from the domain walls. A field of 2000 V/cm was then applied across the sample. The domains grew at 45 degrees to the direction of the applied field. After several minutes, the individual domains coalesced into

a single domain. By integrating the current flow through the sample, the spontaneous polarization of the sample was determined to be 5 $\mu C/cm^2$.

Figures 5-1a through 5-1f illustrate the evolution of the domains changing from time to time during the process of poling.

Figure 5-1a

As the temperature cools down to the phase transition point, domain walls (45 degree) begin to appear inside the crystal.

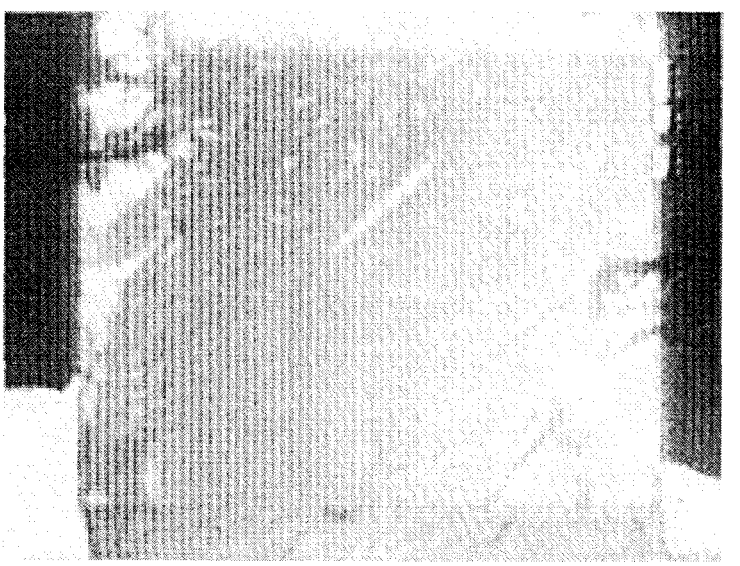

Figure 5-1b

The number of domain walls appearing in the sample increase with time.

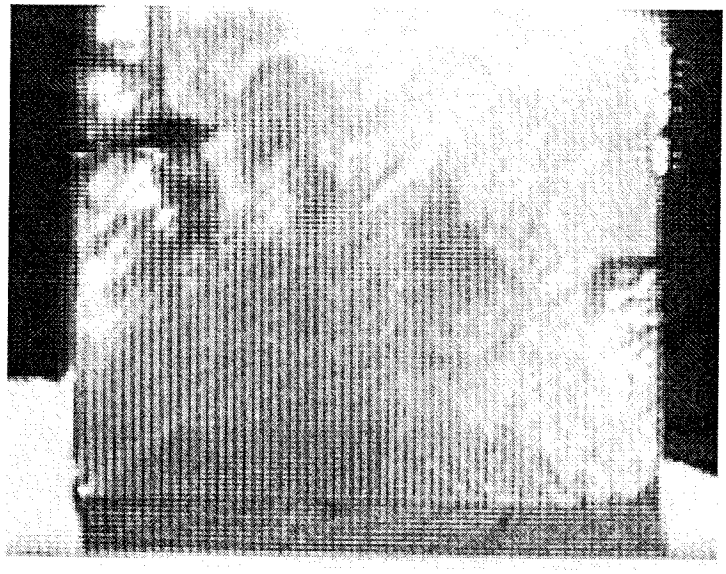

Figure 5-1c

As domain wall formation proceeds, the upper right part of the sample became opalescent.

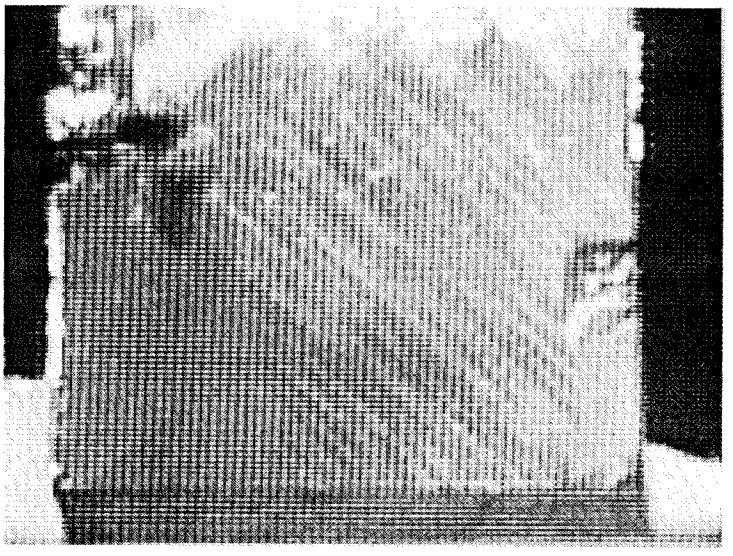

Figure 5-1d

A field of 2000 V/cm was applied across the sample, causing the growth of domains at an angle of 45 degree to the c axis..

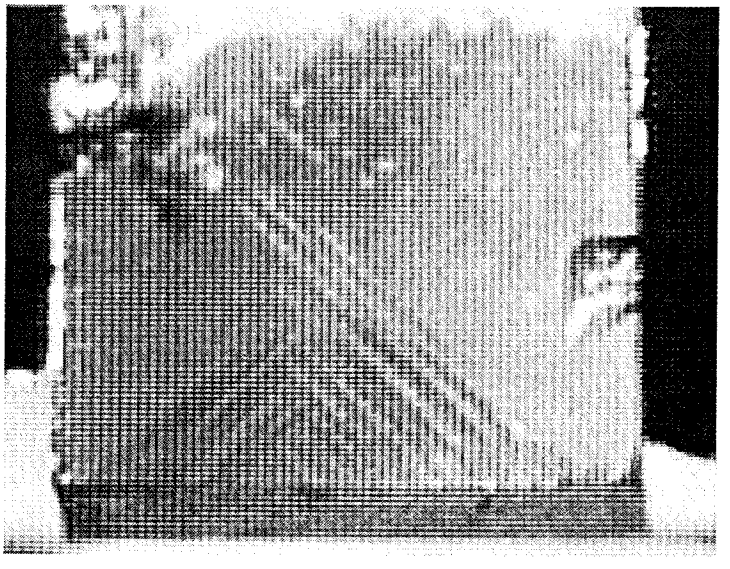

Figure 5-1e

As the domain continues to align under application of the electric field, the domain walls begin to merge.

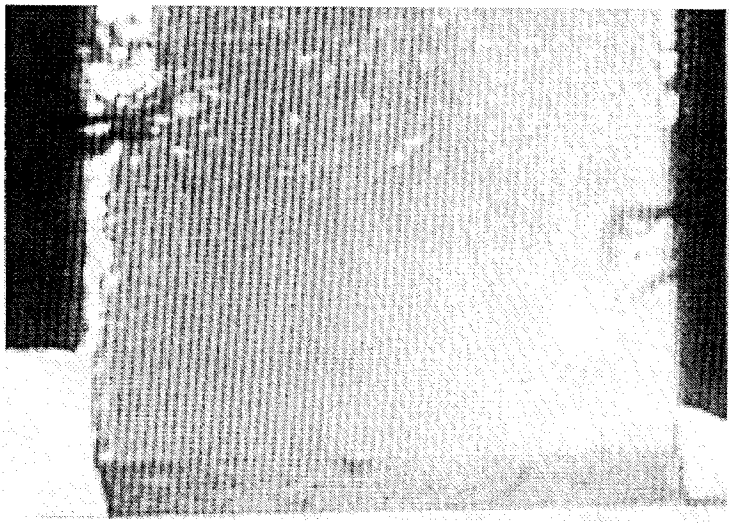

Figure 5-1f

After several minutes the individual domains have coalesced into a single domain. The sample becomes transparant within this ferroelectric phase.

5.3 Electronic Grating

Recording electronic gratings is the first step of the hologram thermal fixing technique. As discussed in chapter two, the electron transport equations in a photorefractive medium are:

$$\frac{\partial N_D^+}{\partial t} = (I_0 \frac{s_e}{h\nu} + \beta_e)(N_D - N_D^+) - \gamma_e N_D^+ n_e \qquad (5\text{-}1)$$

$$\frac{\partial n_e}{\partial t} = \frac{\partial N_D^+}{\partial t} + \frac{1}{e}\frac{\partial}{\partial x}(e\mu_e n_e E_{sc} + eD_e \frac{\partial n_e}{\partial x} n_e) \qquad (5\text{-}2)$$

$$\frac{\partial E_{sc}}{\partial x} = \frac{e}{\varepsilon\varepsilon_0}(N_D^+ - N_A - n_e)\,, \tag{5-3}$$

where N_D^+ is the density of ionized donor, n_e is the density of the mobile electron, I_0 is the optical beam intensity, s_e is the cross section of photoexcited electrons. β_e is the thermal excitation rate, γ_e is the recombination constant for electrons, and μ_e is the mobility of the electrons. Einstein relation

$$\frac{D}{\mu} = \frac{k_B T}{e} \tag{5-4}$$

are used here. The photovoltaic current is neglected because there is no photovoltaic effect observed in KLTN crystals. The transient space charge field at the fundamental grating component is

$$E_{sc} = -im\frac{E_N(E_0 + iE_d)}{E_0 + i(E_N + E_d)}(1 - e^{-t/\tau}) \tag{5-5}$$

$$E_N = \frac{eN_A}{\varepsilon K_g}(1 - \frac{N_A}{N_D}) \tag{5-6}$$

$$E_d = \frac{k_B T K_g}{e}\,, \tag{5-7}$$

where E_N is the charge limited space charge field, E_d is the diffusion field, and E_0 is the spatially uniform applied field. The time constant τ is given by:

$$\tau = t_0 \frac{E_0 + i(E_{\mu_e} + E_d)}{E_0 + i(E_N + E_d)} \tag{5-8}$$

$$t_0 = \frac{h\nu N_A}{s_e I_0 (1 + \beta_e h\nu / (s_e I_0)) N_D} \quad , \tag{5-9}$$

where

$$E_{\mu_e} = \frac{\gamma N_A}{\mu_e K_g} \, . \tag{5-10}$$

In the absence of an external field, the time varying space charge field can be determined by measuring the diffraction of the electronic grating.

In our experiment, an electronic grating was recorded at -30 °C. A weak beam (0.1 W/cm^2) and short writing times were used to prevent domain reversal. A Tektronix 2440 Digital Oscilloscope was used to monitor the displacement current flowing through the crystal. The writing period was 10 seconds, and no external field was applied. We changed the temperature at each point to measure the decay of electron gratings. An external field of 1000 V/cm was applied while measuring the decay rate.

When the temperature was lower than 10 °C, the ionic mobility was negligible during the measurement of the decay rate of electronic gratings . At this stage, when the electron gratings were erased, with a non-Bragg matched Ar ion laser beam, no other grating was revealed. This indicated that it was the electron grating which decayed.

An activation energy of E_a=0.12 eV and a time constant of τ=166 s were determined (Figure 5-2) using eqn. (5-12). We believe this decay is due to the diffusion and drift of shallow trapped electrons which compensate the photorefractive space charge field.

5.4 Ionic Grating

At elevated temperature the ions mobility is much higher than the dark electronic conductivity and cannot be neglected. The transport equation is

$$\frac{\partial n_i}{\partial t} = -\frac{1}{e}\frac{\partial}{\partial x}(e\mu_i n_i E_{sc} - eD_i \frac{\partial n_i}{\partial x}) , \qquad (5\text{-}11)$$

where n_i is the ion density and μ_i is the mobility of ions. The ions drift under the electronic space charge field. At room temperature the electronic grating can be erased by illuminating an uniform beam. This leaves behind an ionic grating. The ionic grating is quasi-stabilized due to partial compensation by electronic grating and diffusion of ions.

Lifetime of electronic and ionic gratings at different temperatures in KLTN:Co,V,Ti crystal

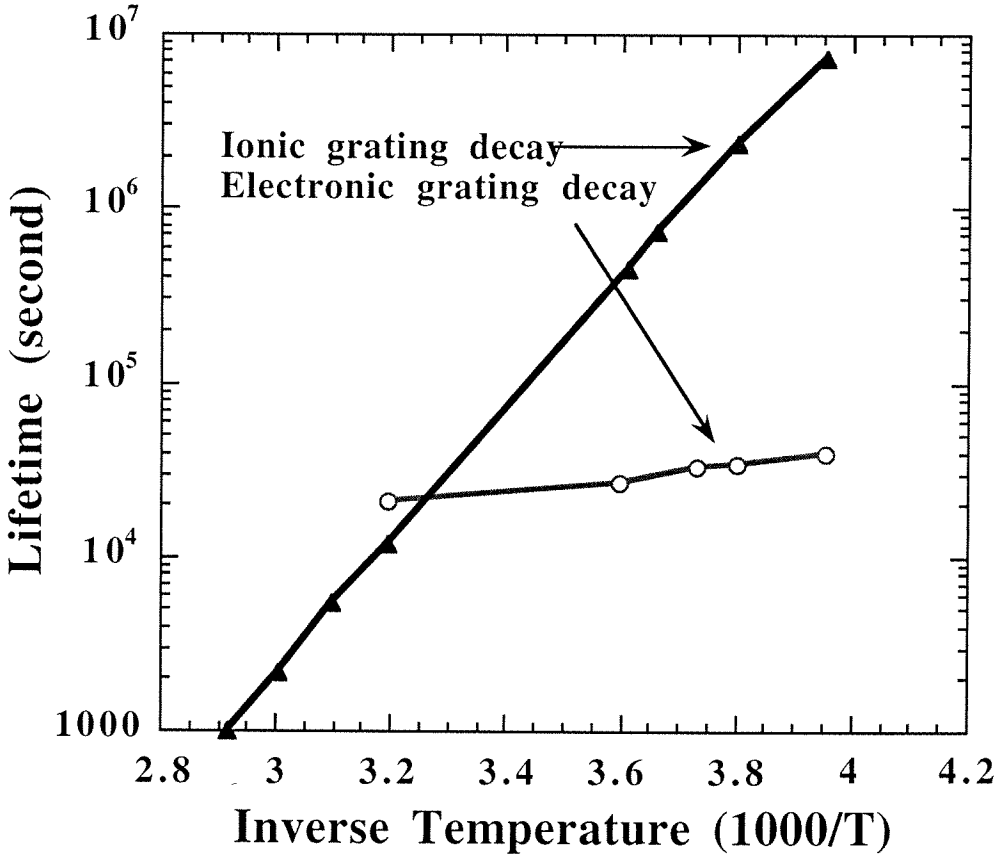

Figure 5-2

Decay rate of ionic and electronic gratings in KLTN : Co, Ti, V crystal. The solid triangles represent ionic gratings and the circles represent electronic gratings.

An Ar ion laser beam at λ=514.5 nm at a total intensity of 1 W/cm^2 was used to write a hologram (Figure 5-3). The polarization of the writing beams was normal to the applied field in order to minimize beam coupling effects, including beam fanning.

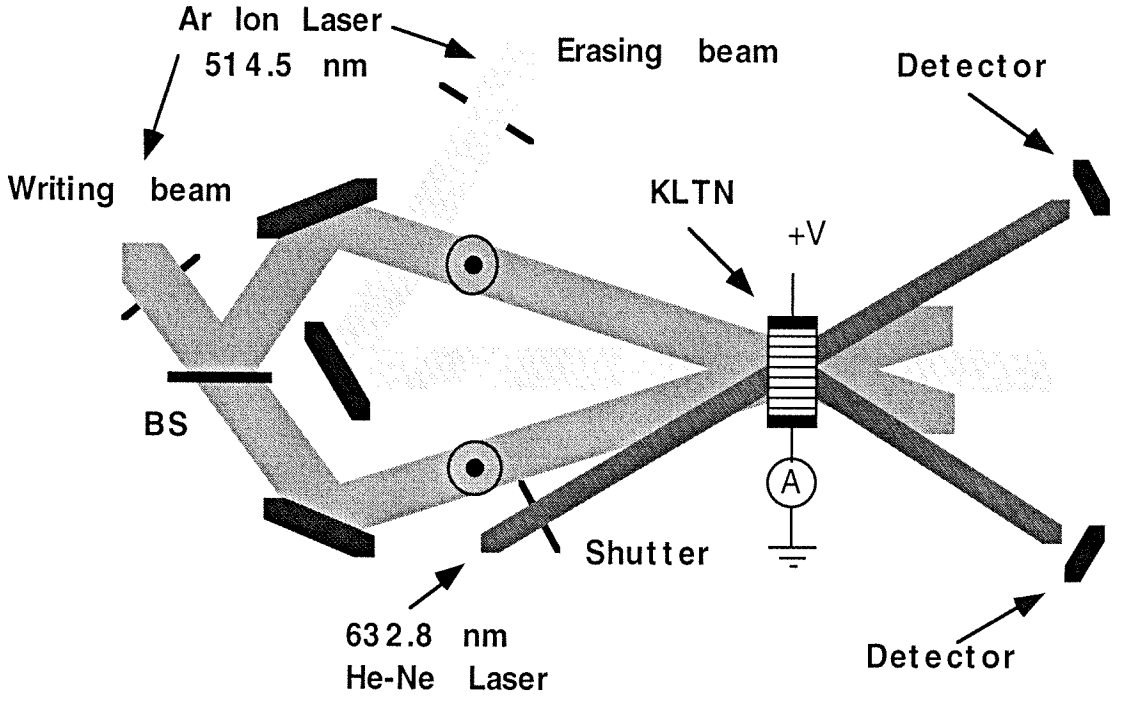

Figure 5-3

The experimental setup. The writing beam and erasing beam have the same optical intensity. The KLTN sample was placed on a thermoelectric temperature-controlled mount enclosed in a vacuum chamber. The intensity of the probe beam was 10 μW/cm^2, and a computer-controlled shutter was used to block the beam between measurements.

5.5 Decay of Fixed Volume Hologram

The decay of fixed volume holograms is due to the ions transport. This transport can be determined by measuring the diffraction of ionic gratings at different temperatures. In our experiment, the grating period was 1 μm. We calculate the diffraction efficiency as the ratio of the diffracted power to the power incident on the crystal corrected for losses from facet reflections. An external field of 2000 V/cm was applied to increase the diffraction efficiency.

We recorded holographic gratings at 70 °C for 20 minutes. The diffraction efficiency increased to a maximum in several minutes and then decreased to a lower level indicating that the ionic grating was partially compensating the electronic space change field. After recording the hologram, the sample was cooled to different temperatures to measure the decay rate of the ion gratings . The fixed grating was read out by an extraordinary polarized He-Ne laser aligned at the Bragg angle. A non-Bragg matched Ar ion laser beam was used to erase the electron gratings. The dielectric constant of the KLTN sample changes dramatically when the temperature is close to T_C. To avoid this dependence, we measured the diffraction when the temperature of the sample was stable. The decay of the ionic gratings obeyed the Arrhenius form

$$\tau_T = \tau_0 \exp(\frac{E_a}{k_B T}) . \qquad (5\text{-}12)$$

An activation energy of E_a=0.76 eV and a pre-exponential constant τ_0 =5x10^{-9} s were fitted to the decay measurements (Figure 5-2). This result differs slightly from the results obtained with KLTN:Cu, Ti, V [9].

In a KLTN : Cu, Ti, V sample with a phase transition temperature of -17°C, the overall efficiency of the fixing process was investigated. A hologram with a diffraction efficiency of 17% was stored at 5°C with an applied field of 2000 V/cm. The sample was then heated to 70°C for 10 min and subsequently cooled to 5°C. The fixed hologram was revealed under uniform illumination with an applied field of 2000 V/cm. The fixed diffraction efficiency reached a value of 11%. The modulation amplitude of the spatially perodic refractive index change of the hologram for extraordinarily polarized light was Δn=1.75 x 10^{-5} before fixing and Δn =1.38 x 10^{-5} after fixing. Thus about 80% of the electronic grating is converted to a fixed grating. This indicates that the electronic dark conductivity, which could lead to thermal erasure of the optically written grating at the fixing temperature, can be neglected.

Unlike $LiNbO_3$ and $KNbO_3$ crystals, there is no photovoltaic effect in cubic KLTN. Diffusion and drift of the photoexcited charge carriers under the externally applied field act to reveal the fixed grating effectively.

5.6 Identification of Protons as the Mobile Ions

To identify a species as mobile ion, one has to show the correlation between the species and the hologram fixing results. In $LiNbO_3$ crystal, the hydrogen ion has been identified [1] as the mobile ion which is responsible for the thermal fixing process. After we found that copper is able to reduce the hydrogen concentration in KLTN crystals, We reduced the hydrogen concentration in $LiNbO_3$ crystals and attempted thermal fixing. Thermal fixing is observed even after the hydrogen concentration has been reduced. Apparently, another species is also responsible for the thermal fixing in $LiNbO_3$ crystal.

To support this claim, the fixing experiments have been carefully done in a few KLTN : Cu, V samples. No fixed grating can be revealed even though the electronic grating has a strong diffraction efficiency.

In the last two chapters, we have described a hydrogen diffusion mechanism. Hydrogen ions exhibit an activation energy of 0.72 eV. The dc conductivity measurement independently indicates a 0.7 eV activation energy for the KLTN samples with hydrogen present. Otherwise the activation energy is about 0.1 eV, which corresponds to shallow trapped electrons. In the samples of KLTN : Cu, V, no hydrogen ions can be observed. Based on this correlation, we believe that hydrogen ions are the mobile ions responsible for the thermal fixing process in KLTN crystals.

5.7 Summary

We have demonstrated fixing of holograms with high efficiency in several samples of KLTN of varying dopant concentrations. Thermal fixing occurs by screening of a photorefractive space charge field by a mobile species (hydrogen ions in this case) at elevated temperatures followed by the revealing of the fixed grating under illumination at lower temperatures. The thermal decay of the hologram exhibited an Arrhenius type dependence with an activation energy near 0.7 eV. For electron grating decay, an activation energy E_a=0.12 eV and time constant τ=166 s were obtained.

References for Chapter Five

[1] Amodei J. J. and D. L. Staebler, Appl. Phys. Lett. **18**, 540 (1971).

[2] Arizmendi L., J. Appl. Phys. **65**, 423 (1989).

[3] Micheron F. and G. Bismuth, Appl. Phys. Lett. **20** , 79 (1972).

[4] M. Horowitz, A. Bekker, and B. Fischer, Appl. Phys. Lett. **62**, 2619 (1993).

[5] F. Kahmann, R. Pankrath, and R. A. Rupp, Opt. Commun. **107**, 6 (1994).

[6] A. S. Kewitsch, M. Segev, A. Yariv, and R. R. Neurgaonkar, Opt. Lett. **18**,1262 (1993).

[7] Agranat A., R. Hofmeister, A. Yariv , Opt. Lett. **17**, 713 (1992).

[8] Hofmeister R., A. Yariv, S. Yagi, A. Agranat, **69**, 9, 1459 (1992).

[9] Leyva V., D. Engin, X. Tong, A. Yariv, A. Agranat, Opt. Lett. **20**,1319-1321(1995).

[10] M. Segev, A. S. Kewitsch, A.Yariv, G. Rakujic, Appl. Phys. Lett. **62**, 907, (1993).

[11] G. J. Fulcher, J. Am. Cer. Soc. **8**, 339 (1925)

Chapter Six

Ferroelectric Domain Grating and Barkhausen Noise in KLTN Doped Crystals

6.1 Introduction

Ferroelectric domain gratings induced by photorefractive space charge fields have been reported in several ABO_3 type crystals[1-3]. Domain gratings can also be generated by the application of external de-poling electric fields during or after optical exposure[4-8]. Barkhausen current spikes arise during domain switching. They have been observed in $LiNbO_3$ [9], $BaTiO_3$ [10], SBN [11], and KLTN crystals. KLTN is a photorefractive crystal [12-14] with a perovskite structure. In the temperature range from 100 K to 400 K the ferroelectric phase transition temperature is determined by the K/Li and Ta/Nb ratios. Above the Curie temperature, KLTN is in cubic phase. The Ta/Nb ion is inside the oxygen octahedron. In the ferroelectric phase, oxygen ions are slightly squeezed between the K^+ ions, and the stable position of Ta/Nb ions is off center along the c axis by about 0.01Å. The distortion of the oxygen octahedron and the displacement of the Ta/Nb ions contribute to the spontaneous polarization of the unit cell of the KLTN crystals.

In a monodomain crystal, if the local electric field is stronger than the local coercive field and in the opposite direction, the local domain can be switched. The photorefractive effect in the presence of a nonuniform

optical illumination can cause a space charge field, which can be larger than the local coercive field in KLTN crystals resulting in locally switched domains. In this chapter we characterize domain gratings in KLTN by measuring the diffraction efficiency and Barkhausen current spikes.

6.2 Ferroelectric Domain Grating

A domain grating was formed in the ferroelectric phase at T=0 °C (T_C=25 °C). We used a monodomain sample for this experiment with the poling procedure described in chapter five. The holographic recording duration was 30 seconds. The displacement current across the sample was monitored simultaneously with the exposure.

The total beam intensity was 1 W/cm^2. We measured displacement current in two stages: 1) one incident beam and 2) two incident beams with the same total intensity. The Barkhausen current spikes were observed in stage 2 only (Figure 6-1), which indicated that domain switching occurred due to the optically induced space charge field.

Figure 6-1(next page)

Barkhausen jumps while recording the hologram in KLTN:doped crystal. a) Total beam intensity is 0.3 W/cm^2. Time scale is one second. The upper curve represents current cross the crystal, the buttom curve is the diffraction efficiency; b) Total beam intensity is 0.4 W/cm^2.

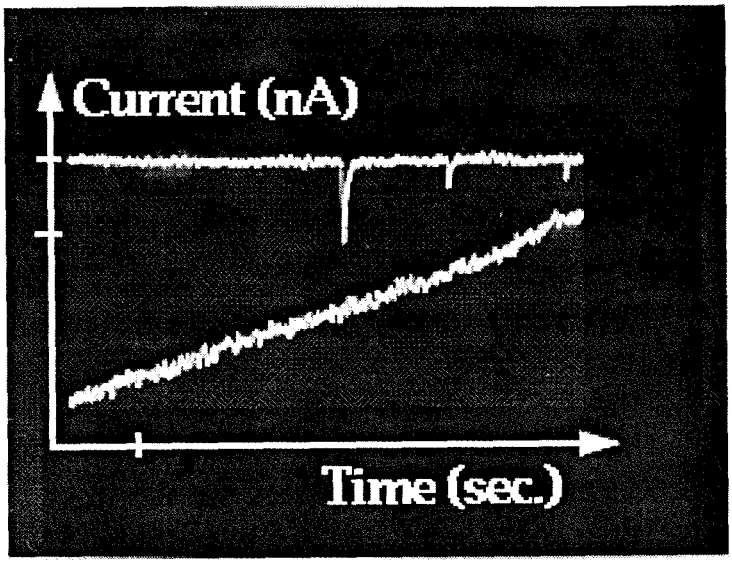

(a)

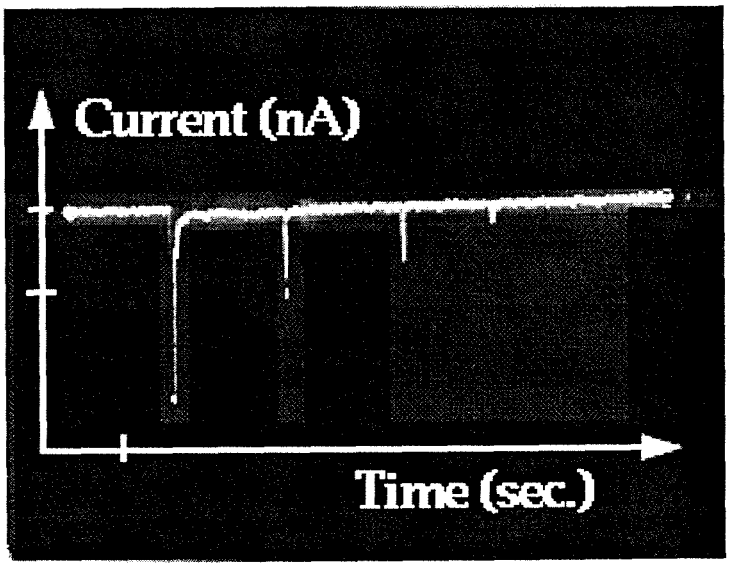

(b)

Exactly what configuration the domain walls took to compensate the space charge distribution is unknown. Both 90° and 180° domains exist in ferroelectric KLTN. We consider the 180 degree domains as the more likely candidate. We shone a 0.01 mW/cm^2 He-Ne beam to measure the diffraction from the domain gratings and used a 0.5 W/cm^2 514.5 nm beam to eliminate the electronic grating. The modulation of any self enhancement [15] was severely diminished with the 514.5 nm beam thus the diffraction was primarily from the domain grating. The diffraction efficiency of the domain gratings was measured to be 55% . The domain grating was electrically erasable with a 3000 V/cm external field when $T>T_C$-20 °C. If the temperature was lower than T_C-30 °C, the electric field would damage the sample before realigning the domains. If the beam intensity was over ~4W/cm^2, the thermalelectric cooler was not effective and optical heating caused the sample local temperature to rise above T_C and the crystal to become the paraelectric. Under this circumstance, the domains would align randomly after the crystal was cooled to below T_C in the absence of an external field. Domain grating decay is shown in Figure 6-2. For $T_C > T >$ -20°C, the functional fit is an Arrhenius relation with E_a = 0.27 eV and a time constant = 0.22 s. For systems that have a polarization freezing temperature T_f, the Vogel-Fulcher law [16] describes a freezing that occurs when the activation energy diverges. For eqn. (5-1)

$$E_a = \frac{E' T}{T - T_f} \qquad (6\text{-}1)$$

where E' is the depth of a potential well. The data from figure 6-2 indicates that T_f = -35°C; then, E'= 13 meV agrees well with the data.

Apparently T_f rises if T_c is raised. This suggests that we may use high T_c crystals to store optical data in the ferroelectric phase by domain switching.

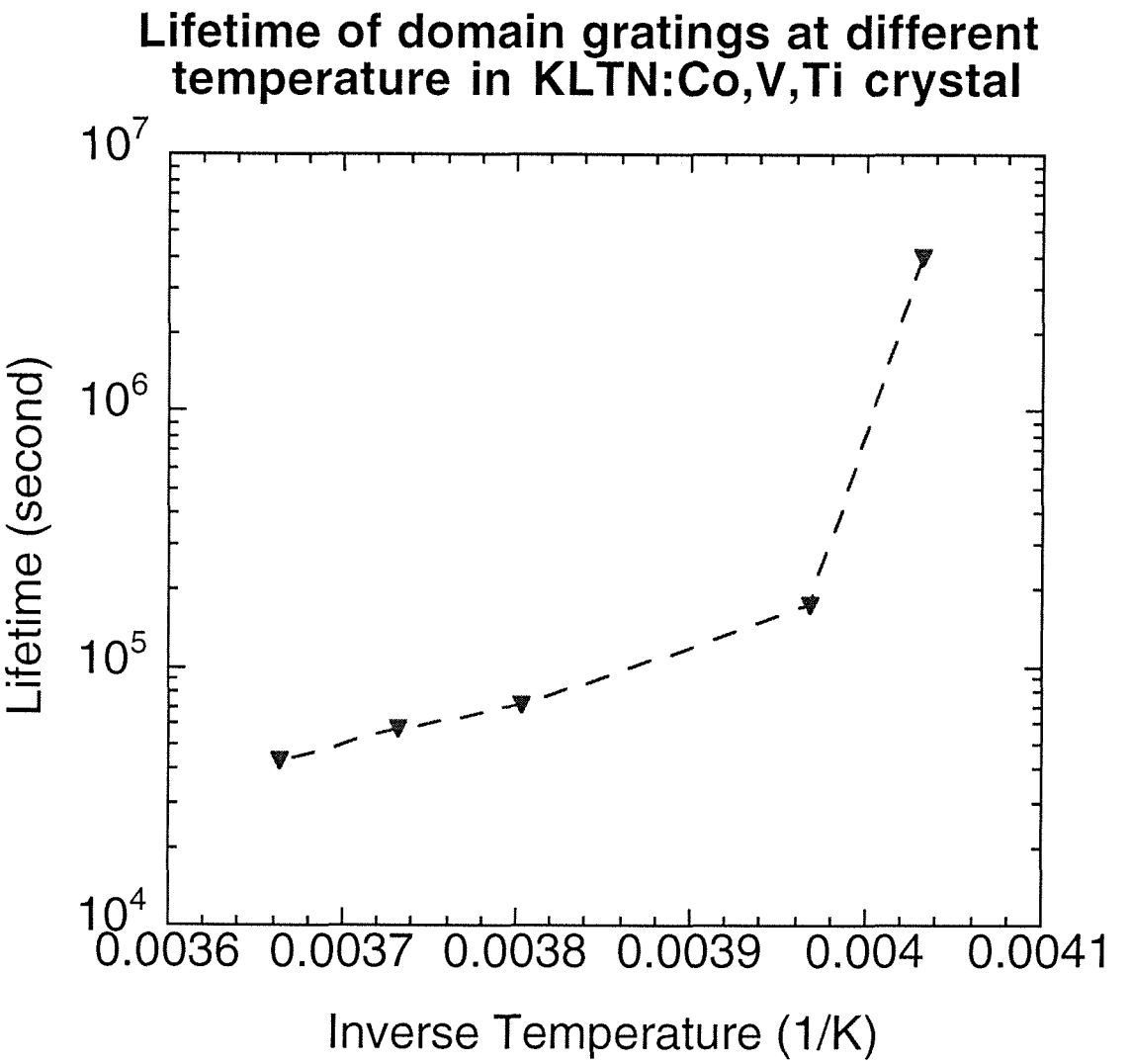

Figure 6-2

Lifetime of domain gratings at different temperature in KLTN:Co, V, Ti crystal.

6.3 Optical Barkhausen Noise

As a domain is inverted, induced time-varying charges cause a current transient, the so-called electrical Barkhausen noise. The walls between neighboring domains carry the bound charge density

$$\rho_{bound} = -\nabla \bullet P_s \ .$$

The free charge density is

$$\rho_{free} = \varepsilon_0 \varepsilon \nabla \bullet E_{sc} + \nabla \bullet P_s \ .$$

Both the bound and the free charges will contribute to the displacement current measured across the crystal [11].

In our experiments, a KLTN sample measuring 6.1 mm x 5.3 mm x 4.5 mm was cut and polished optically along the crystallographic axes. The KLTN crystal was doped with Co, V, and Ti. The ferroelectric phase transition temperature of the sample was determined by monitoring the temperature dependence of the low frequency capacitance. The cubic to tetragonal transition occurred at T_C = 25°C for the sample used in the experiment. We used a thermoelectric controller to provide a stable temperature mount enclosed in a vacuum chamber. We set the temperature to 35°C and cooled the sample to 5°C at a rate of 1°C/min. Upon cooling through the phase transition, the crystal became opalescent as light is scattered from the domain walls. When a field of 2000 V/cm was applied

across the sample along the direction [001], the domains grew at 45 degrees to the direction of the applied field. After several minutes, individual domains disappeared, indicating that the sample became monodomain.

Three types of current transients across the crystal were observed (Figure 6-3):

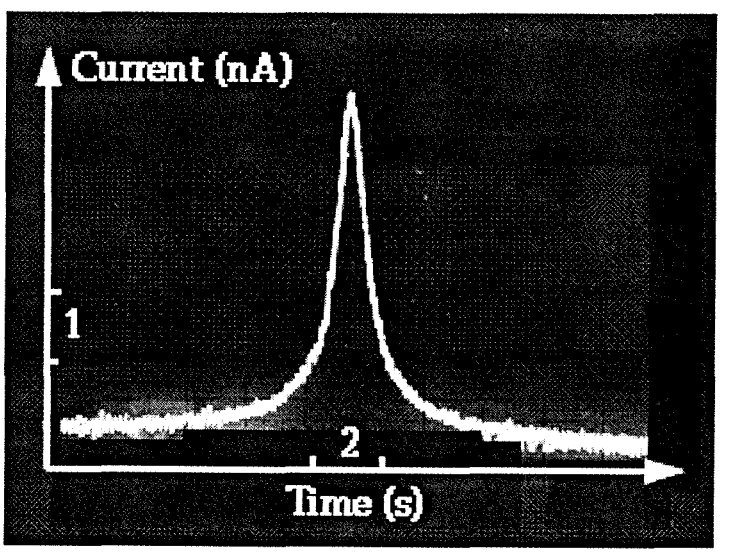

Figure 6-3a

Type I current jump observed in KLTN crystals. Both the rising edge and falling edge are smooth. Time period is about 2 seconds. The varying-charges are around 5 nC.

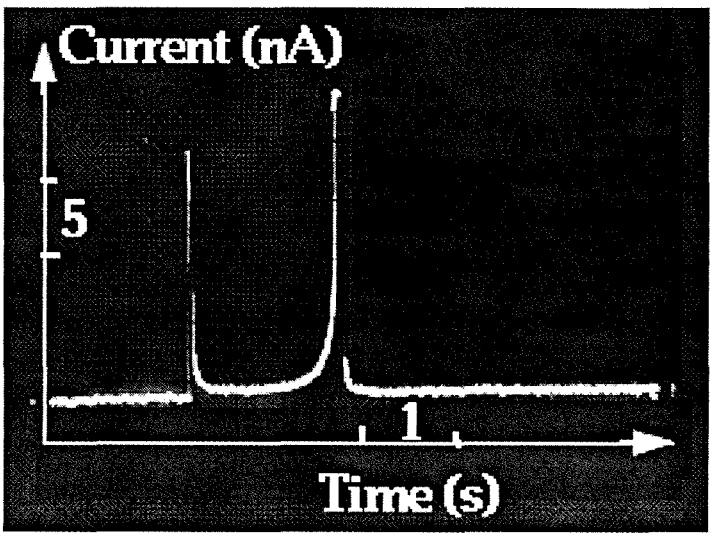

Figure 6-3b

Second and Third types current jumps. Leading edge is sharp in type II and falling edge is sharp in type III. Time duration is typical 0.1 s for type II, 0.5 s for type III.

The time duration of the first type of spike is on the order of a second, and both the rising edge and falling edge are smooth. The second type of jump has a sharp leading edge and an exponentially decay falling edge. The rising time is about 10 ms and falling time 100 ms. The third type of jump has a gentle rising edge but a sharp falling edge. Jumps of the first and second type jumps have been classified in reference [17]. Jumps of the first type appear for all values of the switching fields. It is expected during the relatively slow sideways (perpendicular to the c axis) growth of domains [18]. Jumps of the second type usually happen under strong fields. The sharp leading edge corresponds to a fast nucleation event, and the subsequent exponential decay is associated with the growth of the domain.

The third type of jump has not been reported previously. It may not be due to a single event but rather to multiple events happening in a relatively short time period. The time scale of current jumps in KLTN is much smaller than similar events in barium titanate [10] and strontium barium niobate (SBN) [11]. The possible explanation is that Ta/Nb ions in KLTN have more difficulty moving around the center point than Ti ions in the oxygen octahedron. SBN has a unit cell with tungsten bronze structure so that its Nb ions are less confined than in the perovskites unit cell of KLTN.

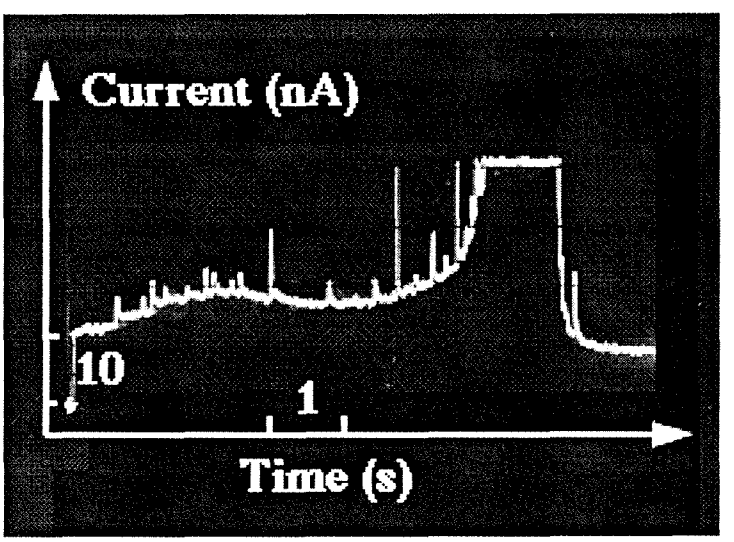

Figure 6-3c

Several current jumps can be seen in this picture.

When a domain grating is formed, significant depolarization fields are generated at the 180° domain walls. For the resulting domain

configuration to be stable, the depolarization fields must be compensated by free charges especially at T close to T_C(T_C-T~10°C, i.e.), otherwise the domains may realign even without external fields. When writing holograms, an electronic grating builds up a space charge field which modulates the domain configuration. Once the domain grating is saturated, the electronic grating provides a screening field to keep the domain configuration stable. When erasing the electronic gratings, the diffraction efficiency decreased to a lower value (but not zero) until saturated, which indicated that the electronic grating was gone (Figure 6-4a).

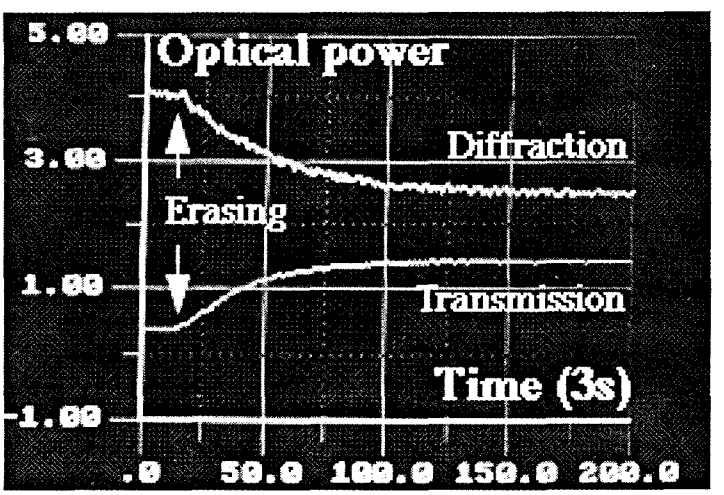

Figure 6-4a

The upper trace represents optical power of the diffraction beam and the lower trace the transmission beam. Because the electronic gratings and domain gratings are in phase, the diffraction efficiency does not pass through zero upon reconstruction, but decays to the remnant value.

Because the phase shift of spatial electric fields between the electronic grating and domain grating is near zero, the total space charge

fields as well as the diffraction efficiency are never equal to zero when erasing the electronic grating.

The domain grating can be erased by applying a 2000 V/cm external field (Figure 6-4b).

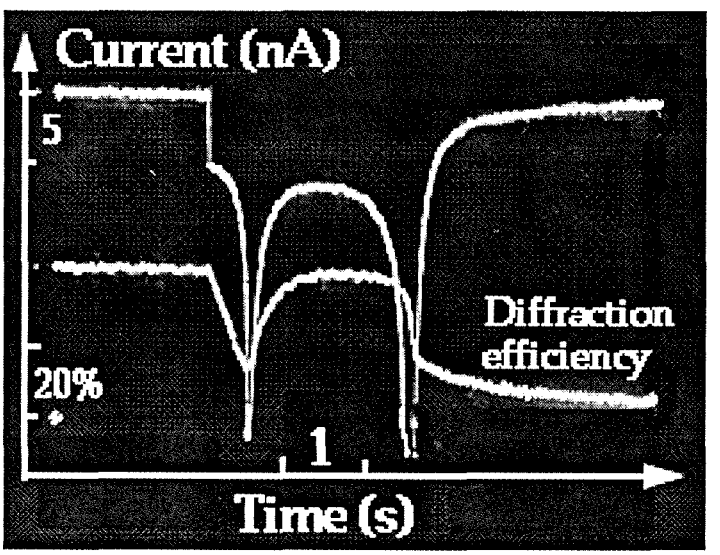

Figure 6-4b

Time scale is 2 seconds. The upper trace represents the current across the sample, the lower trace the diffraction efficiency of domain gratings. The domain realignment causes the domain grating to change and the diffraction efficiency goes down dramatically after an external field of 2000V/cm is applied across the crystal.

When most of the domains realigned, as evidenced by the appearence of a large current jump, the former domain grating was changed and the diffraction efficiency went down dramatically. Temperature is another factor which affects the stabilization of domain gratings. For example, if

temperature is close to the Curie temperature ($0 < T_C - T < 10$), a macrodomain may realign resulting in a current spike while the diffraction efficiency drops by nearly 50% (Figure 6-4c).

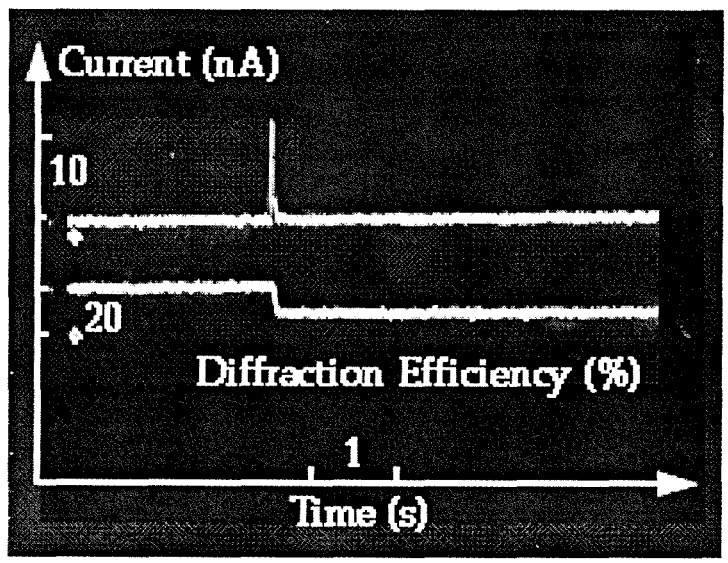

Figure 6-4c

The diffraction efficiency goes down by the order of 50% during a single Barkhausen current spike which corresponds to a macrodomain switching.

6.4 Summary

We have demonstrated domain switching due to the photorefractive space charge field in ferroelectric phase KLTN:Co,V,Ti crystals. The

diffraction efficiency of reversed domain gratings is about 55% in a 2mm thick crystal.

Three types of current pulse shapes associated with ferroelectric domain reversal induced by photorefractive space charge fields in KLTN crystals have been observed. Microdomain switching produces in a time varying-charges from 0.1 to 1 nC, Macrodomain reversal includes time varying-charges up to 0.1 μC. Domain gratings with head-to-head configuration are unstable when the temperature is close to the Curie temperature.

References for Chapter Six

[1] A. S. Kewitsch, M. Segev, A. Yariv, G. J. Salamo, T. W. Towe, E. J. Sharp, and R. R. Neurgaonkar, Phys. Rev. Lett. **73**, 1174 (1994).

[2] A. S. Kewitsch, M. Segev, A. Yariv, G. J. Salamo, T. W. Towe, E. J. Sharp, and R. R. Neurgaonkar, Appl. Phys. Lett. **64**, 1023 (1994).

[3] X. Tong , R. Hofmeister, M. Zhang, A. Yariv, A. Agranat, and V. Leyva, Opt. Lett. **21**, 1860, (1996).

[4] Y. Qiao, S. Orlov, D. Psaltis, and R. R. Neurgaonkar, Opt. Lett. **18**, 1004 (1993).

[5] M. Horowitz, A. Bekker, and B. Fischer, Opt. Lett. **18**, 1964 (1993).

[6] F. Micheron and G. Bismuth, Appl. Phys. Lett. **20**,79 (1972).

[7] F. Kahmann, R. Pankrath, and R. A. Rupp, Opt. Commun. **107,** 6 (1994).

[8] R. S. Cudney, J. Fousek, M. Zgonik, P. Gunter, M. H. Garrett, and D. Rytz, Phys. Rev. Lett. **72**, 3883 (1994).

[9] V. I. Kovalevich, L. A Shuvalov, and T. R. Volk, Phys. Status Solidi (a) **45,** 249 (1978).

[10] R. S. Cudney, J. Fousek, M. Zgonik, P. Gunter, M. H. Garrett, and D. Rytz, Appl. Phys. Lett. **63,** 3399 (1993).

[11] A. S. Kewitsch, A. Saito, A. Yariv, M. Segev, and R. R. Neurgaonkar, J. Opt. Soc. Am. B **12,** 1460 (1995).

[12] A. Agranat, R. Hofmeister, A. Yariv , Opt. Lett. **17**, 713 (1992).

[13] R. Hofmeister , A. Yariv, S. Yagi, A. Agranat, **69**, 9, 1459 (1992).

[14] V. Leyva , D. Engin, X. Tong, A. Yariv, A. Agranat, Opt. Lett. **20**, 1319 (1995).

[15] M. Segev, A. S. Kewitsch, A.Yariv, G. Rakujic, Appl. Phys. Lett. **62**, 907, (1993).

[16] G. J. Fulcher, J. Am. Cer. Soc. **8**, 339 (1925)

[17] A. G. Chynoweth, Phys. Rev. **110** ,1316 (1958).

[18] V. M. Ruduak, A. Y. Kudzin, and T. V. Panchenko, Sov. Phys. Solid State **14** , 2112 (1973).

Chapter Seven

Hydrogen ion and thermal fixing of volume hologram in Potassium Niobate

7.1 Introduction

The properties of thermally fixed holograms in pure $KNbO_3$ and $KNbO_3$:Fe samples have been investigated in this chapter. Potassium niobate is a ferroelectric crystal, and exhibits two-phase transition temperatures, one at 210°C and the second 425°C. At room temperature, a monodomain sample is a good material for dynamic holography due to its large electro-optic coefficients and high photoconductivity [1-5]. Thermal hologram fixing has also been reported [1]; in this material however, fixing efficiencies were less than 1% in a 2 mm thick sample and the fixing species was not identified. In this study, the time constant and activation energy of the fixing species were determined. The results agree with the hydrogen ion diffusion model in a perovskite crystal [6], indicating that hydrogen ions are involved in the thermal fixing process. Because potassium niobate crystal has an orthogonal structure with space group mm2, OH bands are three dimensional polarization dependent at room temperature.

A special cut of iron doped potassium niobate crystal was designed to achieve the maximum exponential gain coefficient for thermal fixing of

volume holograms. A significant enhancement of diffraction efficiency of the fixed grating 43% is measured.

7.2 Anisotropic Activation Energy of Hydrogen Ion

In chapter four, we discussed the double well potential energy model describing hydrogen ion hopping between the two oxygen ions. The activation energy for hydrogen ion diffusion is given by the difference of the energy barrier height and the zero point energy. The zero point energy is the same along a, b ,or c direction. The energy barrier is the dominate factor in the value of activation energy along each direction.

In potassium niobate crystals, oxygen octahedron distort in such a way that the short distance between the two nearest neighbor oxygen ions is 2.79 angstrom and the longer one is about 2.86 angstrom. This leads to an anisotropic activation energy for a hydrogen ion hopping in the crystal. Combining the theoretical model in chapter four and the FTIR spectra data in this chapter (section four), we find that the activation energy for hydrogen ion is 0.64 eV and 0.81 eV along b and c directions, respectively.

7.3 Special Cut Sample

In order to obtain the highest diffraction efficiency, the exponential gain coefficent Γ must be maximized by selecting the appropriate facet orientation. The value of Γ depends both on the material parameters (such

as the density of mobile charges N_A, the effective electro-optic coefficient γ_{eff}, and the dielectric constant ε) as well as external controlled parameters (such as the angle 2θ between the two beams, and the angle β between the bisector of the two beams and the c axis in the crystal). Assuming that the induced index grating is phase shifted by $\pi/2$ relative to the intensity distribution, the exponential gain coefficient Γ is [7]:

$$\Gamma = \frac{\omega}{2nc}\frac{E_{sc}\gamma_{eff}}{\cos\theta}, \qquad (7\text{-}1)$$

where ω is the optical angular frequency, c the velocity of light, and n the refractive index chosen according to the beam polarizarion. In the absence of an extenal electric field, the space charge field E_{sc} induced by the interference patten is :

$$E_{sc} = \frac{k_B T}{q}\frac{K\cos 2\theta}{1+K^2/K_0^2} \qquad (7\text{-}2)$$

$$K = \frac{4\pi n}{\lambda}Sin\theta \quad ; \quad K_0^2 = \frac{q^2 N_A}{K_B T\varepsilon\varepsilon_0}, \qquad (7\text{-}3)$$

where λ is the vacuum wavelength, $\varepsilon\varepsilon_0$ the dielectric constant along the grating vector, and 2θ the angle between the two beams. The γ_{eff} is the effective Pockel coefficient of the iron doped potassium niobate crystal. For the extraordinary polarized beam γ_{eff} in the c-b plane is [7]:

$$\gamma_{eff} = \frac{\cos\beta}{2}[n_b^4\gamma_{23}(\cos 2\theta - \cos 2\beta) + 4n_b^2 n_c^2\gamma_{42}\sin^2\theta + n_c^4\gamma_{33}(\cos 2\theta + \cos 2\beta)] \quad (7\text{-}4)$$

where γ_{ij} are the elements of the linear electro-optic tensor, n_b and n_c the principal indices of refraction at a wavelength λ. For potassium niobate crystals at λ=514.5 nm, n_b=2.395, n_c=2.211, γ_{23}=1.3 pm/V, γ_{33}=64 pm/V, and γ_{42}=380 pm/V [8]. The exponential gain coefficient can be obtained as a function of angles β and θ according to eqs (7-1)-(7-4). A computer-generated three dimensional plot of the exponential gain coefficient Γ versus the angles β and θ is presented in figure 7-1 to aid in visualizing the complicated behavior of the gain.

The optimum value of β corresponding to the maximum Γ is approximately 40° to the c axis and is nearly independent of N_A over the range from 10^{16} cm^{-3} to 10^{17} cm^{-3}. The angle θ is chosen to be 8° for our experiments.

An iron doped potassium niobate crystal is cut as 40° to the c axis in the c-b plane (Figure 7-2). The thickness of the sample is 4 mm. The sample was placed on a thermoelectric temperature-controlled mount enclosed in a vacuum chamber. Holographic gratings were written using two beams with 400 mW/cm^2 intensity from an Ar^+ laser operating at 514.5 nm. The beams were expanded to completely illuminate the sample and were ordinary polarized in order to minimize coupling effects. The full angle between the writing beams was 16 degrees (Figure 7-2), which

resulted in a grating period of 1.9 μm. The grating vector was oriented 40° to the c axis in the c-b plane.

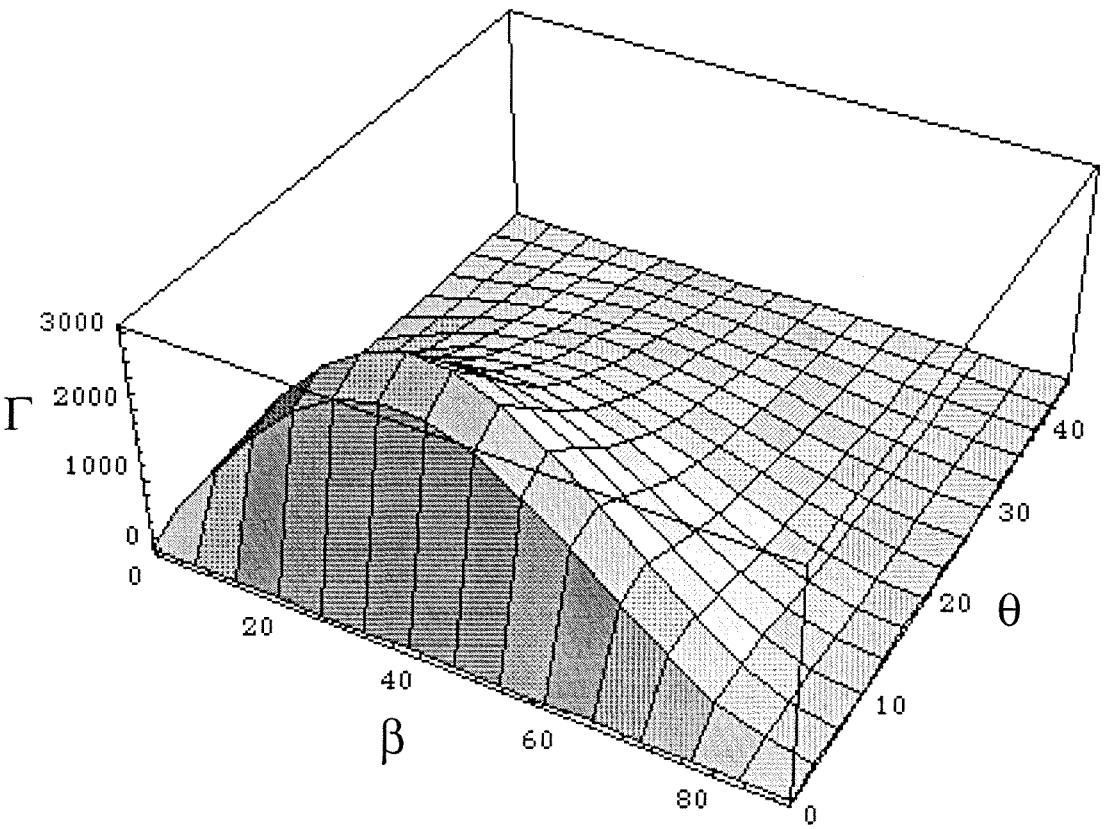

Figure 7-1

A computer-generated three dimensional plot of the exponential gain coefficient Γ versus the angle β and θ. Roughly speaking, the maxiumum Γ is corresponding to β=40° and θ=8°. Γ unit is m^{-1}.

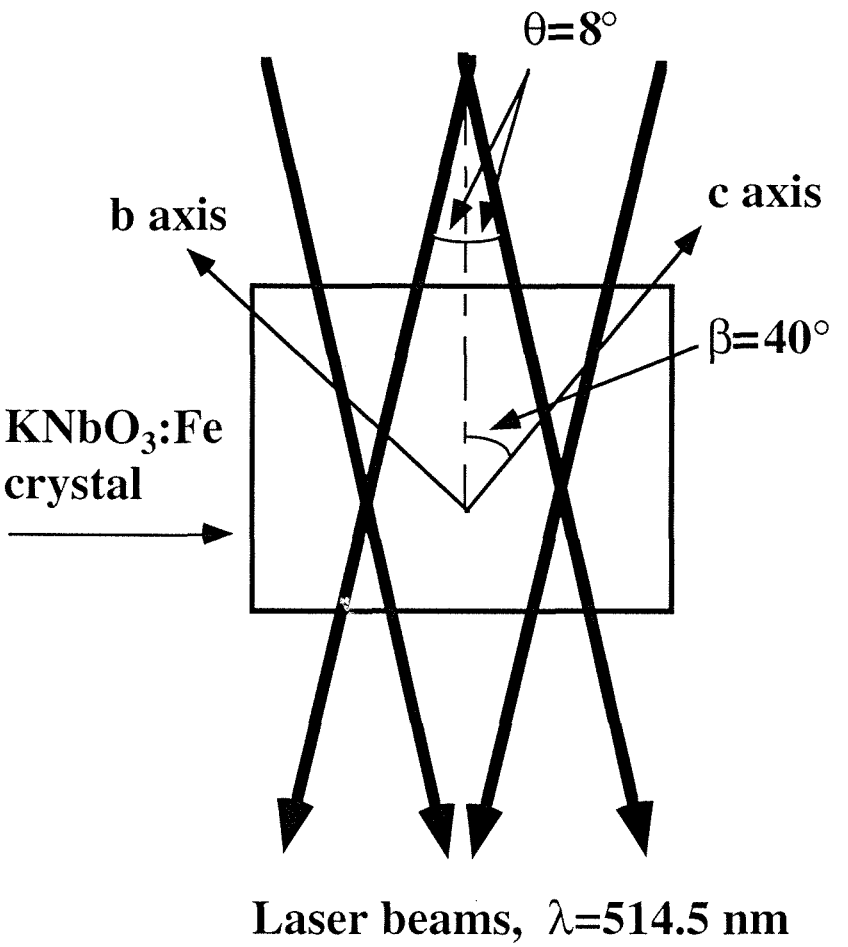

Figure 7-2

An iron doped potassium niobate crystal was cut as shown to reach the maximum gain. Two writing laser beams is at λ=514.5 nm with full angle 2β=16°. The angle β is about 40°.

The hologram was read out with a weak He-Ne laser beam (633 nm) aligned to the Bragg angle. No external field was applied to the sample. The diffraction efficiency is defined as the ratio of the diffracted to

incident intensities corrected for surface reflections. The intensity of the probe beam was 10 μW, and a computer-controlled shutter was used to block the beam between measurements.

The $KNbO_3$:Fe sample was heated to 110°C. The writing beam then illuminated the sample for a period of three hours. The diffraction efficiency increased to about 66% in a few seconds and then dropped due to ionic screening at a much slower rate. The electronic hologram was next erased by illuminating the crystal with a non-Bragg matched Argon ion laser. When this erasure of the electronic grating was complete, the diffraction efficiency first dropped in a short time and then rose, until it saturated at 43% (Figure 7-3). The sample was then quickly cooled to a lower temperature to measure the decay rate of the fixed ionic gratings. The decay rate at 110°C was also measured.

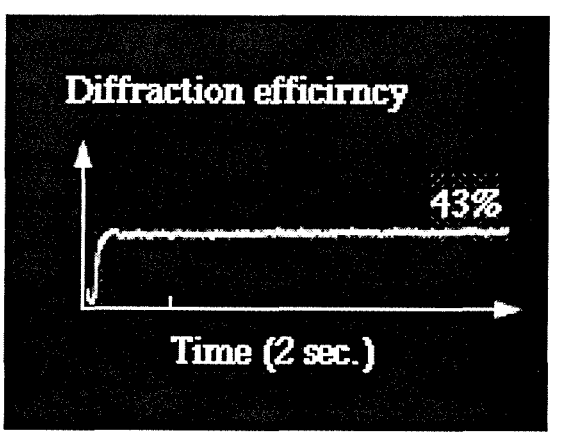

Figure 7-3a

The diffraction efficiency changes during the process of erasing the electronic gratings. When we started to erase the electronic grating, the diffraction efficiency first dropped and then rose until saturation which indicates that the electronic grating has disappeared.

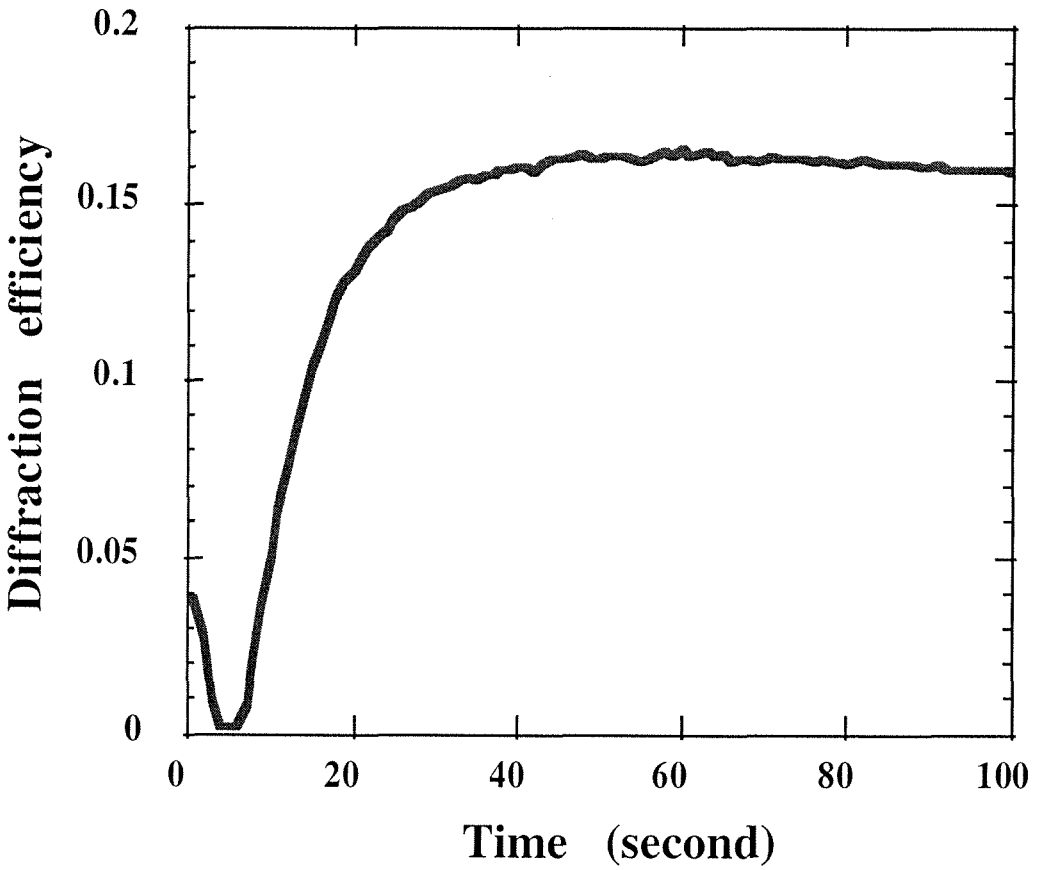

Figure 7-3b

In a regular cut sample, the thermal fixing experiments has also been done. The diffraction efficiency of fixed grating reached a value of 16%.

The fixed holograms were observed to decay at a rate that is independent of illumination. Neglecting the electronic dark conductivity, the decay time for fixing with an ionic species is essentially given by the dielectric relaxation time of the sample [9]:

$$\tau = (\omega_i + D_i K^2 + iK\mu_i E_0)^{-1},$$

where $\omega_i=(e\mu_i n_{i0}/\varepsilon)$ is the ionic dielectric relaxation frequency, μ_i is the ionic mobility, n_{i0} is the ionic density, ε is the dielectric constant, D_i is the ionic diffusion constant, K is the grating wave vector, and E_0 is the applied field. Hologram decay measurements were made in the temperature range of 50°C to 110°C. The fixed grating was read out by an extraordinarily polarized He-Ne laser aligned at the Bragg angle. Figure 7-4 shows the diffraction beam intensity vs. time. A function of $\{\exp(-t/\tau^b)+\exp(-t/\tau^c)\}^2$ was used to fit the decay curves, with excellent agreement.

In potassium niobate crystals, hydrogen ions are hopping between the two nearest oxygen ions. The distance between the two nearest oxygen ions are different along the three principal axes. This may cause different behavior for hydrogen ion hopping along the different directions. In other words, the ionic moblity is isotopic in potassium niobate crystals. This is confirmed in our experiments. In particular, the decay of the ionic gratings obey the Arrhenius form for both the b and c direction:

$$\tau_T^b = \tau_o^b \exp(E_A^b / K_B T) \qquad (7\text{-}5a)$$

$$\tau_T^c = \tau_o^c \exp(E_A^c / K_B T)\,. \qquad (7\text{-}5b)$$

For the c direction, the activation energy E_A is 0.81 eV, and the time constant τ_0 is 2.9×10^{-7} s. This result is similar to the result in reference [8]. For the b direction, the activation energy E_A is 0.64 eV, with a time constant τ_0 is 1.5×10^{-5} s. (Figure 7-5).

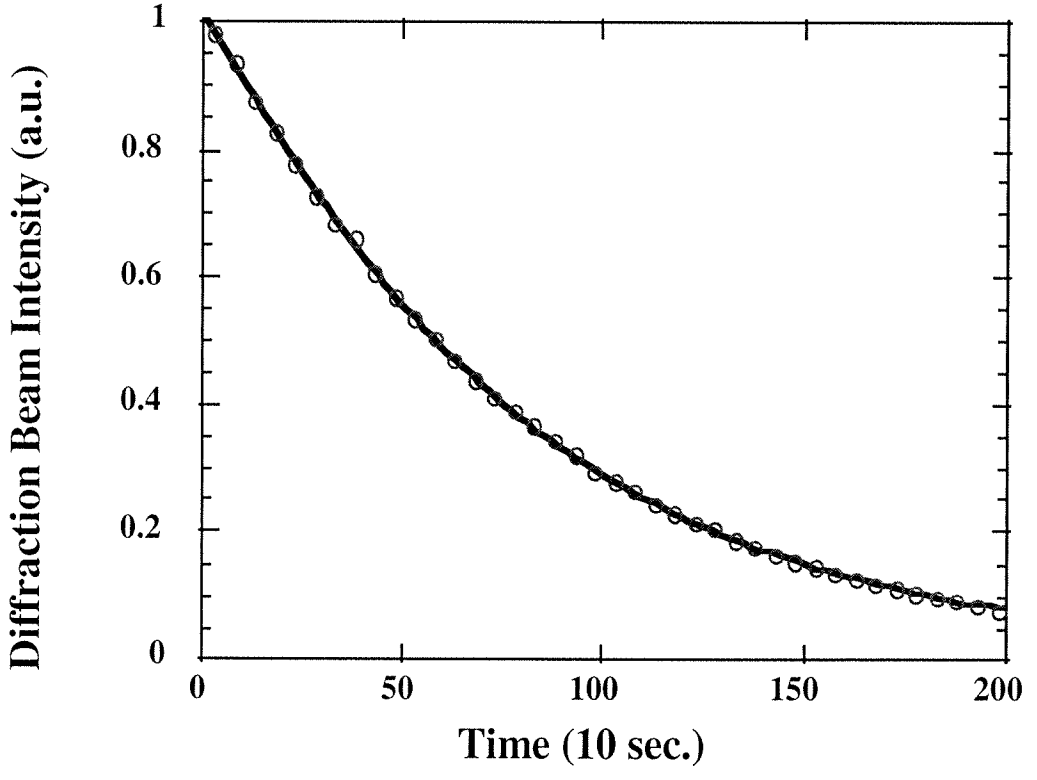

Figure 7-4

The diffracted beam intensity drops with time at 110°C. The function $\{\exp(-t/\tau^b)+\exp(-t/\tau^c)\}^2$ was used to fit the experimental data, (assuming protons correspond to the decay along two directions) with excellent agreement. The solid line is the theoretical curve and the open circles are the experimental data.

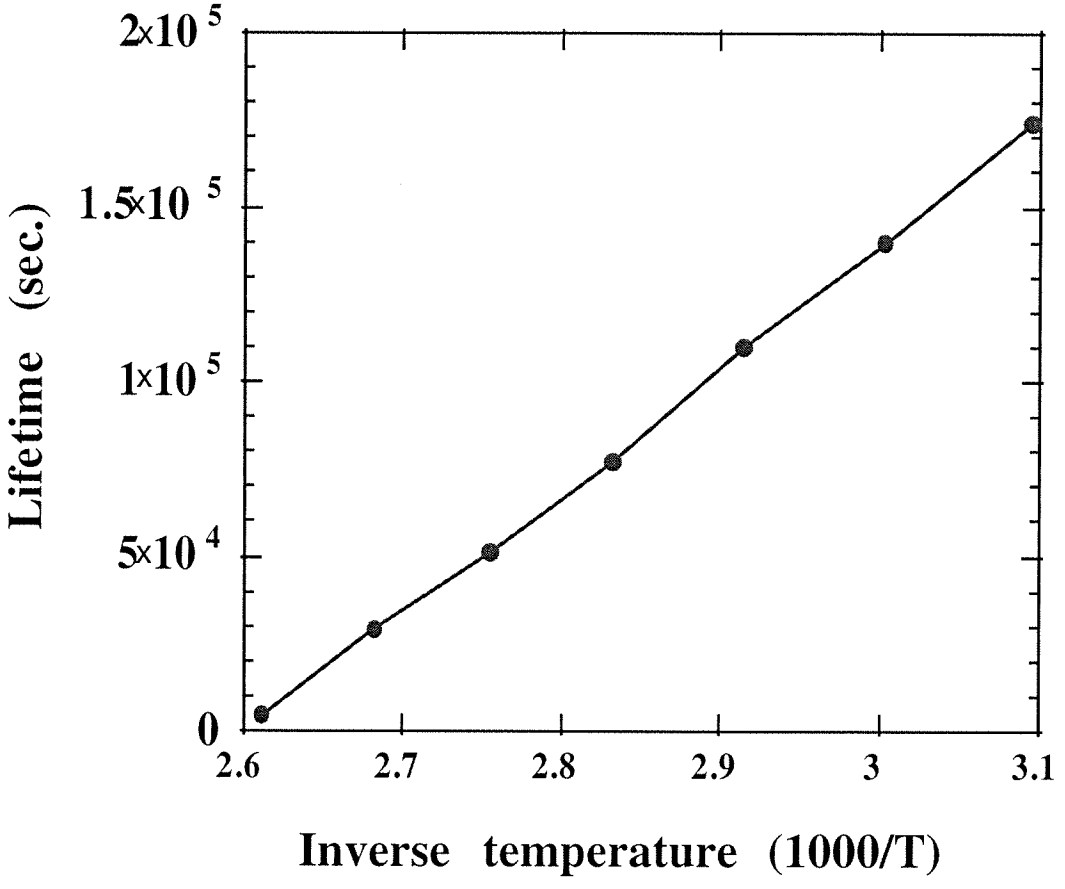

Figure 7-5

The decay rate of ionic gratings measured by the holographic method in an iron doped potassium niobate crystal. This decay corresponds to the hydrogen ions hopping along the b axis. The activation energy is about 0.64 eV with a time constant 1.5×10^{-5} s.

To verify the activation energy along the b direction, a dc conductivity measurement was performed in vacuum for temperatures between 283 and 383K. Expressing the conductivity by

$$\sigma = \sigma_0 \exp(-E_A / K_B T) . \qquad (7\text{-}6)$$

The activation energy E_A for hydrogen ion migration was found to be 0.64 eV (Figure 7-6), which is consistent with the hologram decay measurements.

Similar experiments along the c direction was unsuccessful because of strong current fluctuations. This may arise from domain switching when an external field is applied along the c direction, and is enhanced at elevated temperatures.

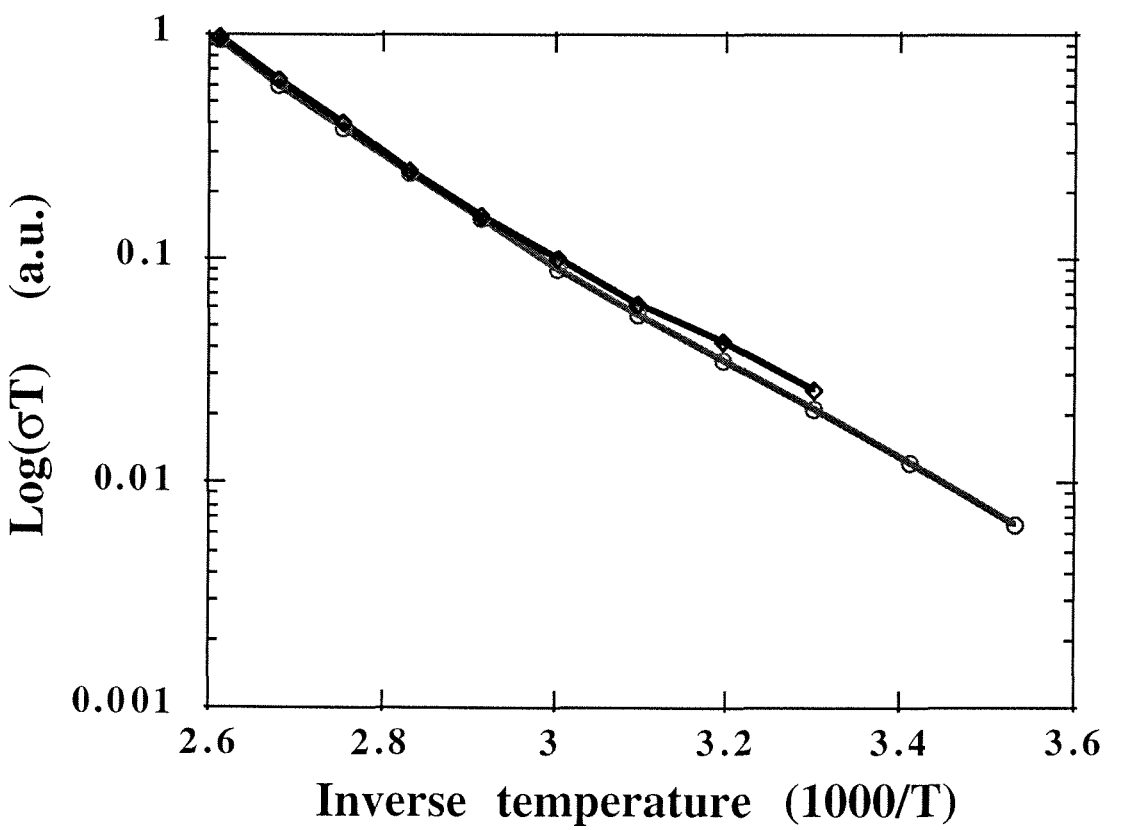

Figure 7-6 (previous page)

Measured temperature dependence of the hydrogen ion conductivity between 283 K and 383 K in iron doped potassium niobate crystal along the b direction. The activation energy, proportional to the slope of the curve, is about 0.64 eV. This data is consistent with the hologram decay experiments in figure 7-5.

7.4 3D Polarization of OH Band

Absorption bands countered at the wave-numbers 3504 cm^{-1} and 6843 cm^{-1} have been observed in potassium niobate crystals. These absorption bands correspond to the transition energies of O-H stretching vibration, from the ground state to the first excited state and to the second excited state, respectively. Absorption bands around 3992 cm^{-1} and 4476 cm^{-1} are attributed to the combination of O-H vibration plus libration. The integrated absorption intensities around 3504 cm^{-1}, 3992 cm^{-1}, and 4476 cm^{-1} arise from the dimensional polarization dependence which arises from the anisotrpic motion of hydrogen ions in the lattice.

Potassium niobate ($KNbO_3$) is an important optical material for both frequency conversion [2] and photorefractive [3, 4] applications. The best photorefractive properties are normally achieved in iron doped crystals [5]. The large photoconductivity of $KNbO_3$ is responsible for the observed fast recording times and for the relatively fast erasure times of the hologram during readout. However, a nondestructive readout of stored information is

needed for various applications, e.g., optical signal processing and associative memories. In reference [10], we reported the high efficiency thermal fixing of volume holograms in potassium niobate crystals. Hydrogen ions play an important role in the process of thermal fixing. Potassium niobate crystal has a perovskite structure with space group C_{2v} (mm2) at room temperature. An interstitial proton binds with an adjacent oxygen ion to form an [OH^-] center, giving rise to a stretching-mode absorption in the infrared. This has been reported in many ABO_3 type crystals such as lithium niobate [11], barium titanate [12] and potassium tantalate [13], etc. Beside the vibration, [OH^-] bands also display librational motion [14]. The integrated absorption intensity is proportional to the [OH^-] band concentration in the certain polarization. This enables us to compare the [OH^-] band concentration differences between the different polarization. The polarization dependence of the integrated absorption intensity corresponds to the hydrogen ions distribution along the different axes in the crystal. In this study, we investigated the properties of hydrogen ion in the lattice of potassium niobate through FTIR spectra.

Iron doped and undoped potassium niobate crystals are employed in our experiments. The samples are cut along the a, b, and c directions and optically polished. The IR absorption spectra characteristic of the stretching vibration of the [OH^-] were monitored using a FTIR spectrometer(Mattson Instruments Inc. Gl-2020). All spectra were recorded at room temperature. Linearly polarized light is used to obtain the polarization dependence of the integrated absorption intensity. The IR beam is incident normally to the surface of the sample. All the data were averaged over 100 to 1000 measurements depending on the signal to noise

ratio. Figure 7-7 shows the FTIR spectra at different spectral region. The strongest absorption peak is around 3504 cm^{-1} (Figure 7-7a), which corresponds to the transition energy between ground state and the first excited state of [OH^-] vibration.

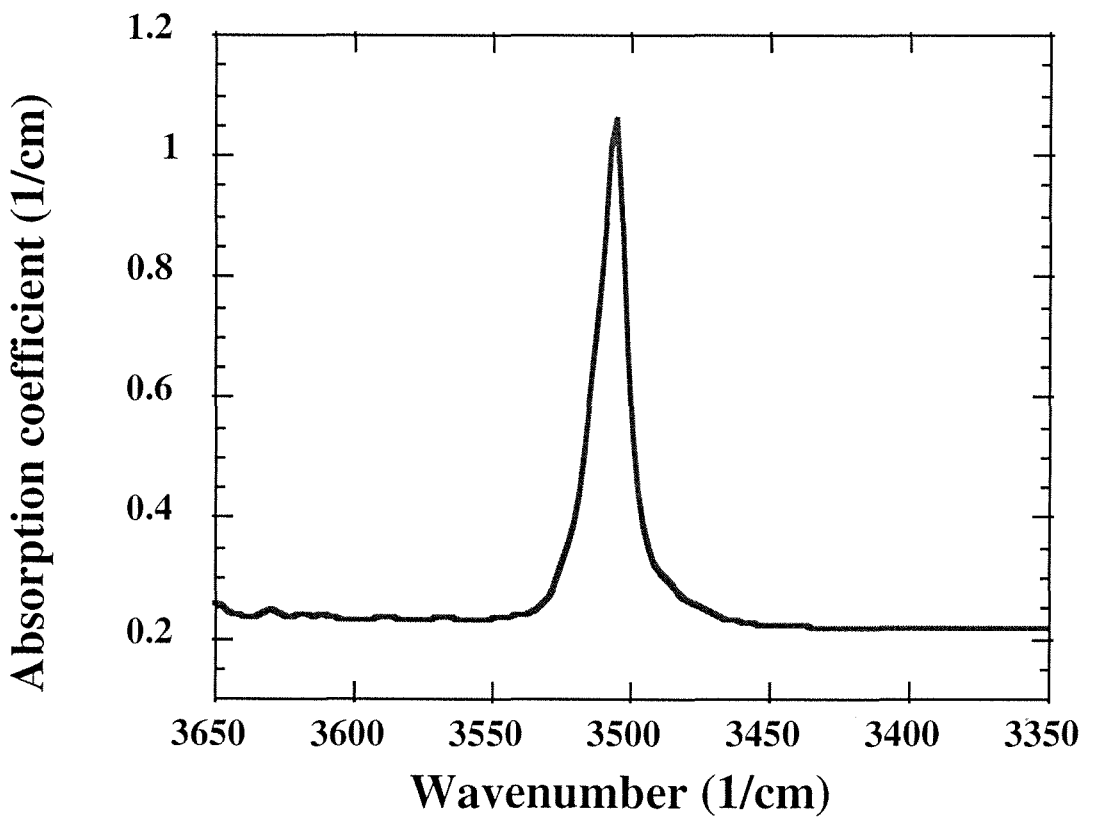

Figure 7-7a

[OH^-] absorption spectrum of potassium niobate crystal near 3504 cm^{-1}. It corresponds to the transition energy between ground state and the first excited state of [OH^-] vibration.

The transition energy between ground state and the second excited state displays an absorption peak around 6843 cm^{-1} (Figure 7-7b). The absorption bands around 3992 cm^{-1} and 4476 cm^{-1} are attributed to the combination of the [OH^-] vibration plus libration (Figure 7-7c).

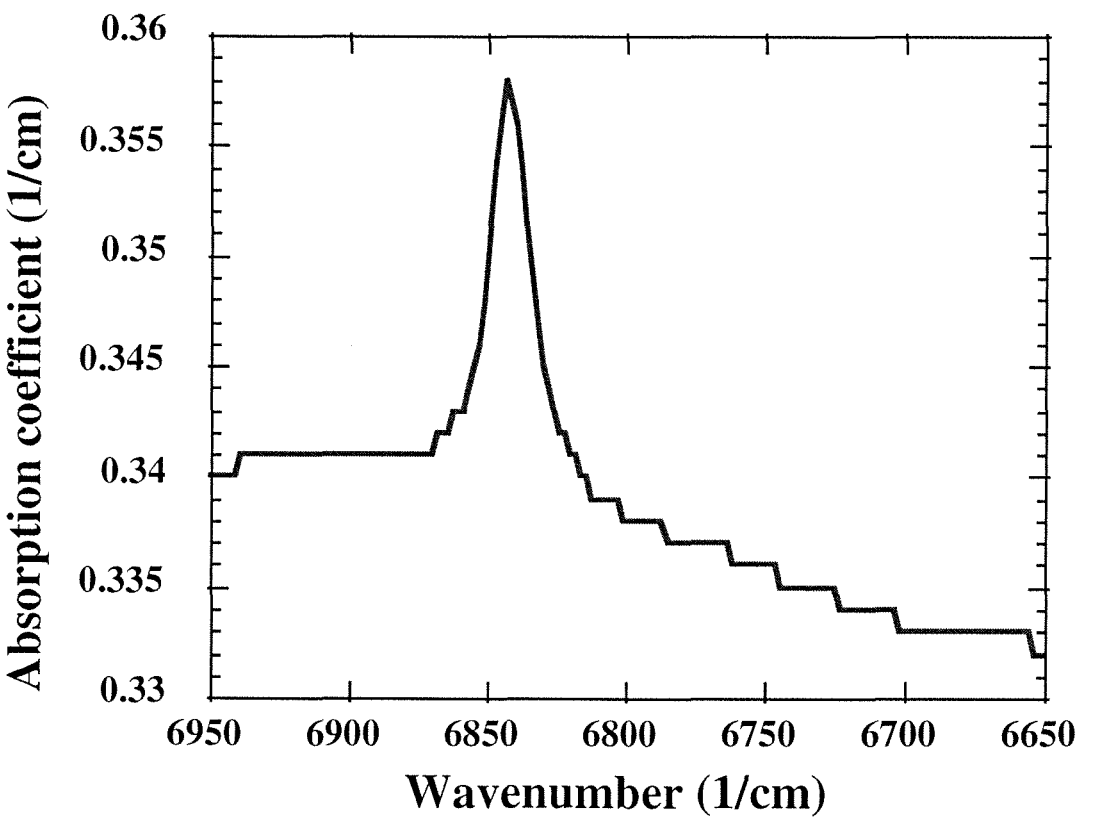

Figure 7-7b

[OH^-] absorption spectrum of potassium niobate crystal near 6843 cm^{-1}. It corresponds to the transition energy between ground state and the second excited state of [OH^-] vibration.

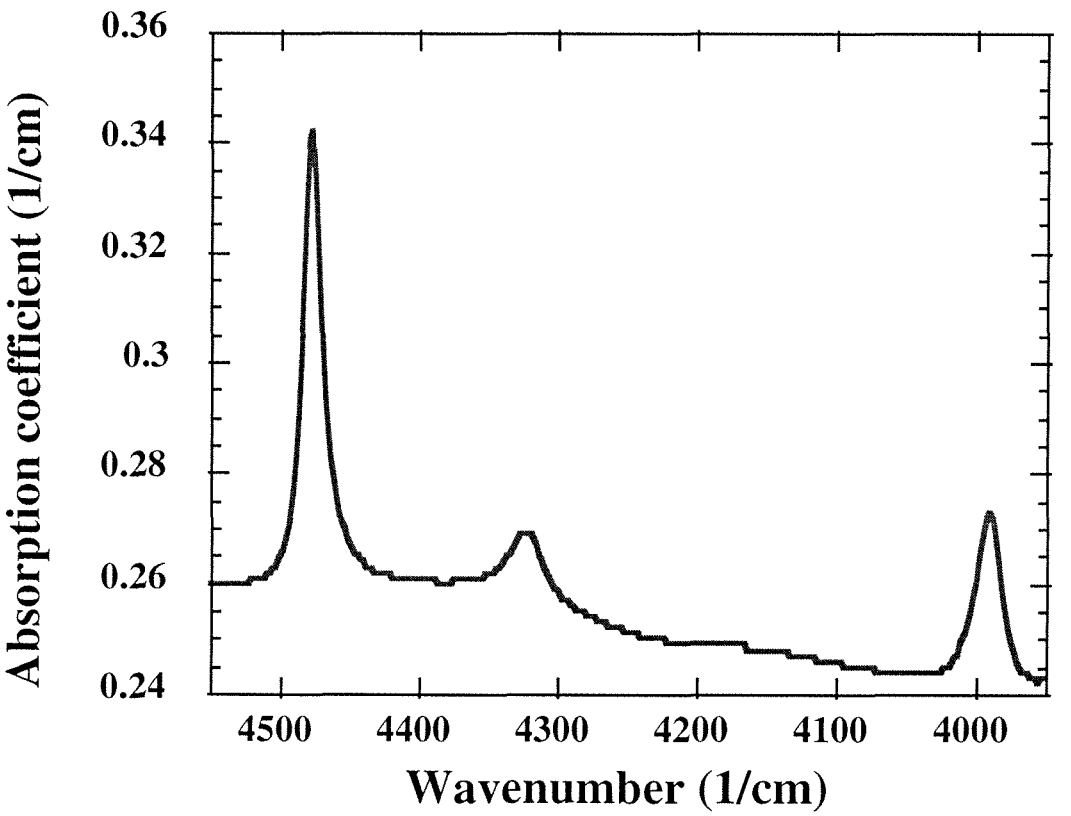

Figure 7-7c

[OH^-] absorption spectrum of potassium niobate crystal in the range of 3950 cm and 4550 cm. The absorption peaks near 3992 cm^{-1} and 4476 cm^{-1} are attributed to the combination of [OH^-] vibration plus libration.

The measurements of the polarization dependence of [OH^-] band absorption are carried out as follows: The three principal axes of the crystal are along the beam propagation direction, the horizontal direction, and the vertical direction, respectively. The zero degree polarization is chosen in the horizontal direction. The polarizer is rotated by 10 degrees per step and measurement is performed at each step, until the polarization is rotate a 90 degrees. The experimental results are shown in Figure 7-8.

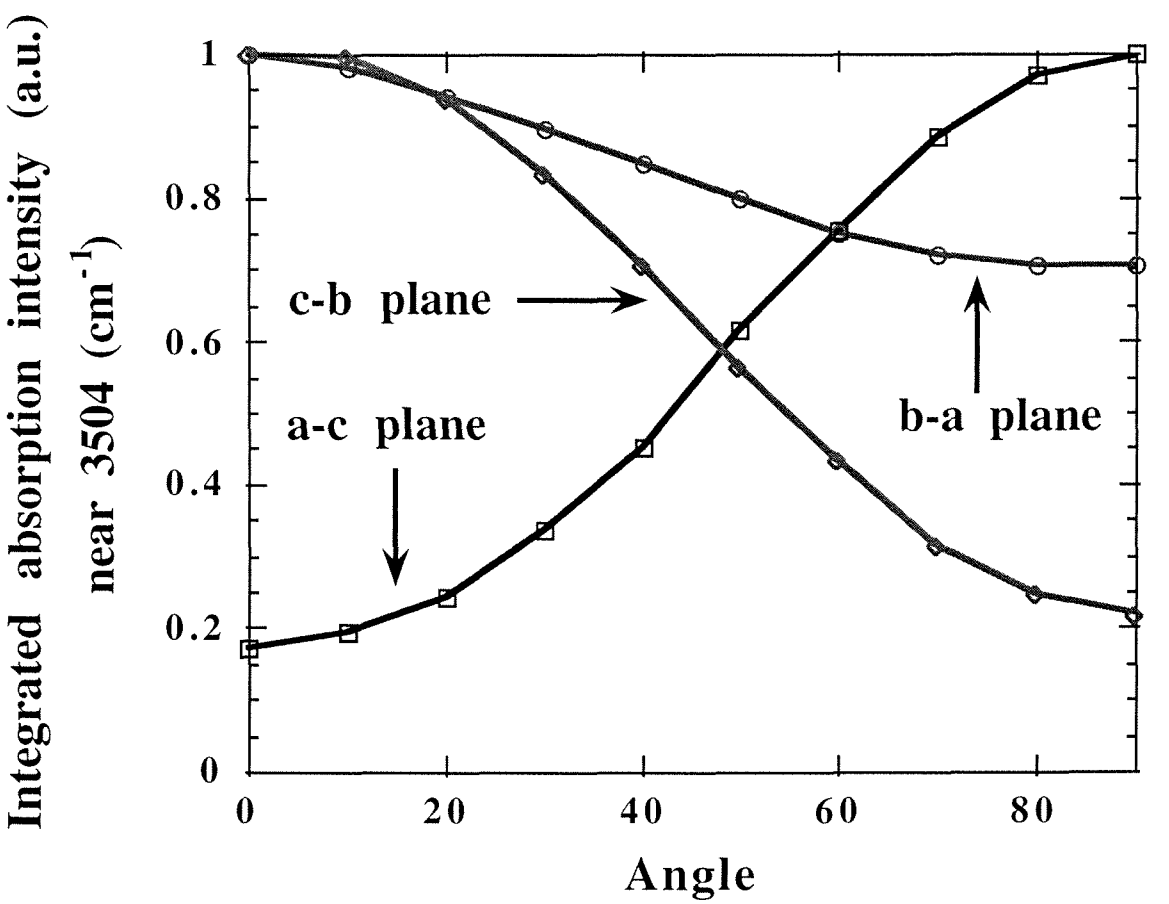

Figure 7-8 (previous page)

Angular dependence of the polarization characteristics of the [OH^-] stretching vibration in a potassium niobate crystal. The "a-b plane" means that the polarization is in the a-b plane and angle with respects to the a axis, and so as to the other plane.

The integration is calculated in the range of 3520 cm^{-1} and 3490 cm^{-1}. When the polarization is in the c-a plane and along the c axis (the beam along the b axis), the integrated absorption intensity is almost 6.5 times larger than that for polarization along the a axis. In the c-b plane, the difference of the integrated absorption intensity is about a factor of 5 between the two perpendicular polarizations along the axis. In the a-b plane, the difference is about a factor of 1.3. All curves follow a $Sin^2(\theta)$ function. Here θ is the angle with respect to one principal axis as specified in the figure caption. These results indicate that most [OH^-] bands are oriented along the c axis of potassium niobate crystals. For the purpose of comparison, similar FTIR data is taken for lithium niobate crystals, where most of the [OH^-] bands are perpendicular to the c axis. The integrated absorption intensity is about 20 times different for polarizations oriented perpendicular and parallel to the c axis.

The energy levels of [OH-] libration are [9]:

$$E_l^{\theta} = (l + 1/2)\hbar\omega' \ . \qquad (7\text{-}7)$$

$\hbar\omega'$ was determined from the FTIR spectra to be 0.06 eV and 0.12 eV for 3992 cm^{-1} and 4476 cm^{-1}, respectively. Unlike KLTN crystals [5], in potassium niobate crystals the energy levels of [OH^-] libration are different along each axis. Figures 7-9, 7-10 give the polarization dependence of integrated absorption intensity near 3992 cm^{-1} and 4476 cm^{-1}.

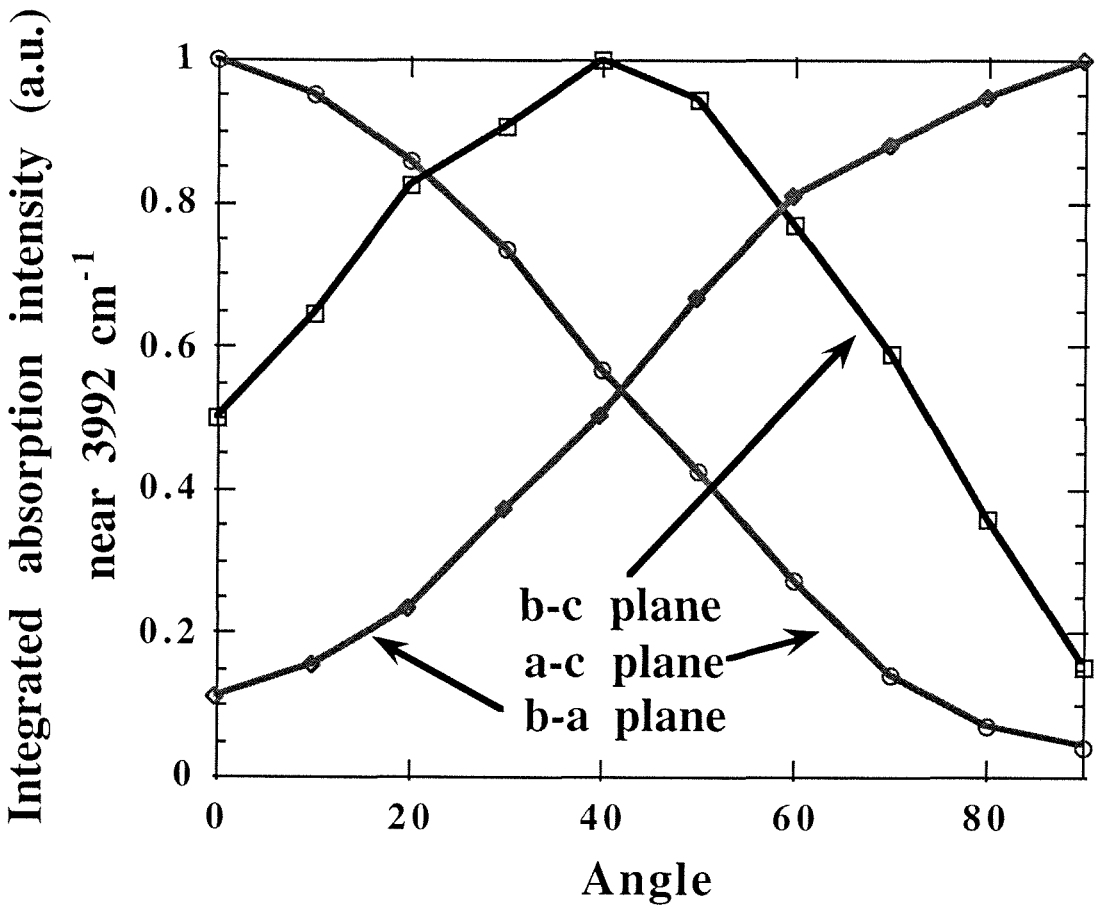

Figure 7-9

Angular dependence of the polarization characteristics of the [OH^-] vibrational-librational combination side band around 3992 cm^{-1}.

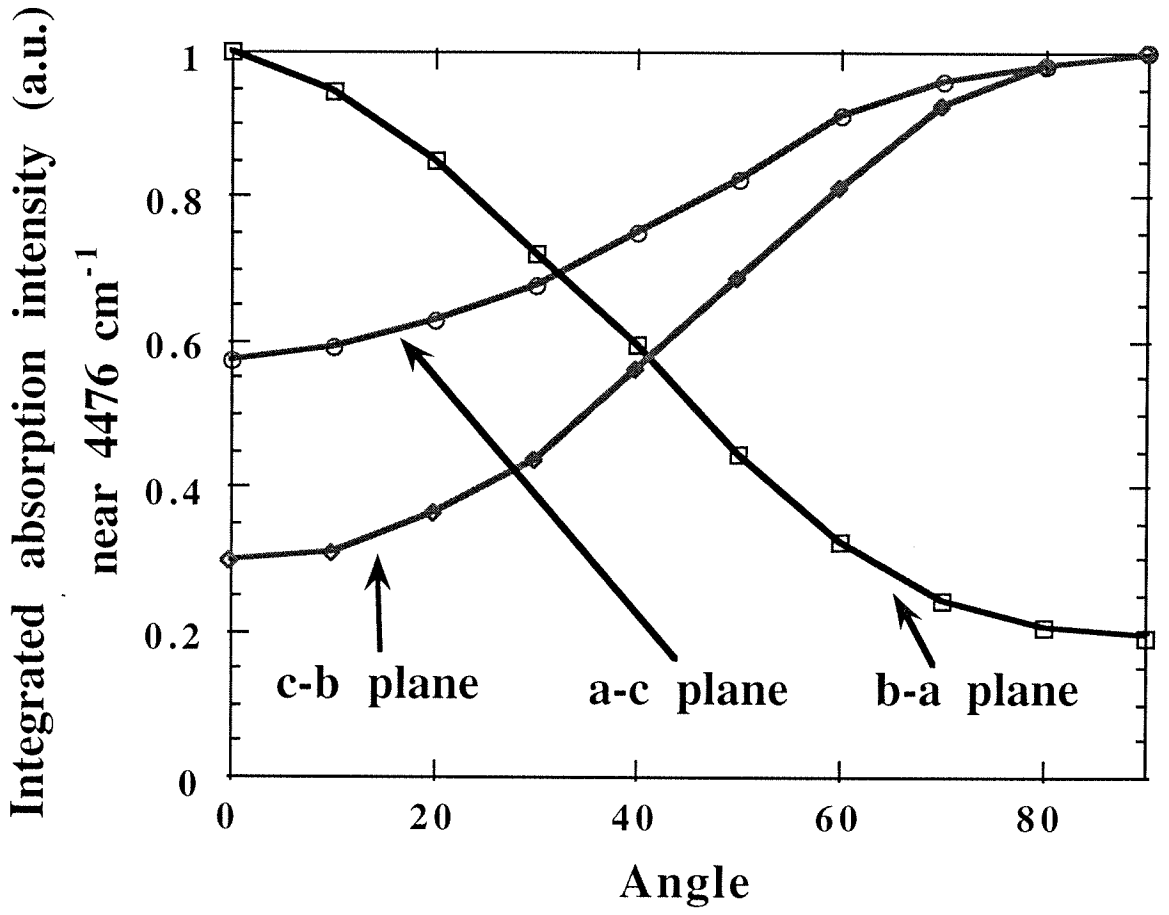

Figure 7-10

Angular dependence of the polarization characteristics of the [OH^-] vibrational-librational combination side band around 4476 cm^{-1}.

The strongest absorption around 3992 cm^{-1} is along the a axis, which indicates that [OH^-] libration along the a axis is due to the [OH^-] bands along either the b or the c axis, where the transition energy for this libration is 0.06 eV. In the a-c plane (Figure 7-9), the difference of integrated absorption intensity between the a axis and the c axis is about 23 to 1. In the a-b plane (Figure 7-9), it is about 15 to 1. Similarly the strongest absorption around 4476 cm^{-1} is along the b axis which indicates that [OH^-] libration along the b axis is more likely due to the [OH^-] bands along the c axis. In the a-b plane (Figure 7-10), the difference of integrated absorption intensity between the a axis and the c axis is about 1 to 4. In the c-b plane, it is about 1 to 5.3. The transition energy for this libration is near 0.12 eV.

In KLTN crystals, we are able to reduce the hydrogen ions concentration by doping with copper. The absorption peak near 4490 cm^{-1} disappears only in crystals which show no absorption peak near 3512 cm^{-1}. This is direct evidence to support that the origin of the absorption at 4490 cm^{-1} is due to the combination of [OH^-] vibration plus libration.

In the potassium niobate crystal, it was found that the stongest absorption near 3504 cm^{-1} occurs for light polarized perpendicular to the light polarization of maximum absorption near 3992 cm^{-1} and 4476 cm^{-1}. This indirect evidence also supports the claim that the origin of the absorption at 3992 cm^{-1} and 4476 cm^{-1} is due to the combination of [OH^-] vibration plus libration.

7.5 Summary

A suitably cut iron doped potassium niobate crystal was designed to achieve the maximum exponential gain coefficient. Volume holograms are thermally fixed in this sample through the screening of a photorefractive space-charge field by hydrogen ions at elevated temperatures. A diffraction efficiency of 43% in a 4 mm thick $KNbO_3$:Fe sample is measured. The activation energies of the holograms' thermal decay are determined to be 0.81 eV and 0.64 eV for the $KNbO_3$:Fe sample, which corresponds to hydrogen ions hopping along the c and the b axis, respectively.

We have also demonstrated that most [OH^-] absorption bands in $KNbO_3$ arise from vibration along the c axis in both the iron doped and undoped crystals. Absorption bands near 3504 cm^{-1} and 6843 cm^{-1} correspond to the transition energies of O-H stretching vibration, from the ground state to the first excited state and to the second excited state, respectively. The absorption bands near 3992 cm^{-1} and 4476 cm^{-1} are attributed to the combination of O-H vibration plus libration. The integrated absorption intensities near 3504 cm^{-1}, 3992 cm^{-1}, and 4476 cm^{-1} display three dimensional polarization dependence arising from the anisotrpic motion properties of hydrogen ions in the lattice. The strongest absorption around 3992 cm^{-1} is along the a axis which indicates that [OH^-] libration along the a axis is attributed to the [OH^-] bands along either the b or the c axis, whose transition energy for this libration is 0.06 eV. Similarly, the strongest absorption around 4476 cm^{-1} is along the b axis

which indicates that [OH^-] libration along the b axis is attributed more likely by the [OH^-] bands along the c axis.

References for Chapter Seven

[1] G. Montemezzani and P. Gunter, J. Opt. Soc. Am. B **7**, 2323 (1990).

[2] J. C. Baumert, J. Hoffnagle, and P. Gunter, Appl. Opt. **24**,1299 (1985).

[3] P. Gunter, Phys. Rep. **93**, 199(1982).

[4] P. Gunter and F. Micheron, Ferroelectrics **18**, 27 (1978)

[5] C. Medrano, E. Voit, P. Amrhein, and P. Gunter, J. Appl. Phys. **64** 4668 (1988).

[6] X. Tong, M. Zhang, A. Yariv, A. Agranat, Appl. Phys. Lett. **69**, 3345 (1996).

[7] Y. Fainman, E. Klancnik, and S. H. Lee, Opt. Eng. 25, 228 (1986).

[8] P. Gunter, Phys. Rep. **93**, 199(1982).

[9] A. Yariv, S. Orlov, G. A. Rakuljic, and V. Leyva, Opt. Lett. **20**, 1334 (1995).

[10] X. Tong, M. Zhang, A. Yariv, and A. Agranat, Appl. Phys. Lett. **69**, 3369 (1996).

[11] J. Amodei and D. Staevler, Appl. Phys. Lett. **18**, 540 (1971).

[12] S. Kapphan, J. Koppitz, G. Weber, Ferroelectrics **25**, 585 (1980).

[13] H. Engsreom, J. B. Bates, and L. A. Boatner, J. Chem. Phys. **73**(3) (1980).

[14] A. Grone and S. Kapphan, Ferroelectrics, **125** , 307 (1992).

Chapter Eight

Topological Distribution of Optical Mixing Phase Matching in Biaxial Crystals

8.1 Introduction

The nonlinear optical response of a material can produce optical frequency conversion. Three-wave mixing process involves two optical waves which produces a third (sum/difference) wave within a nonlinear optical medium. Sceond harmonic generation is thought as a degenerate case of three-wave mixing in which both waves have the same optical frequency. In order to use bulk crystal to achieve efficient frequency conversion, a technique called phase matching is applied. This technique takes several forms, including birefringent (angle/temperature) phase matching [1,2], quasi-phase matching [3-6], and self-phase matching [7] . Our focus will be on the birefringent (angle) phase matching, in which the direction of the optical beam within the crystal is selected for efficient frequency conversion.

Suitable nonlinear optical crystals are essential to produce nonlinear optical effects. A crystal may have one or two optical axes, in which case it is designated uniaxial and biaxial. We only consider the biaxial case here. Figure 8-1 illustrates the projection of refractive index ellipse on the x-z plane for biaxial crystals.

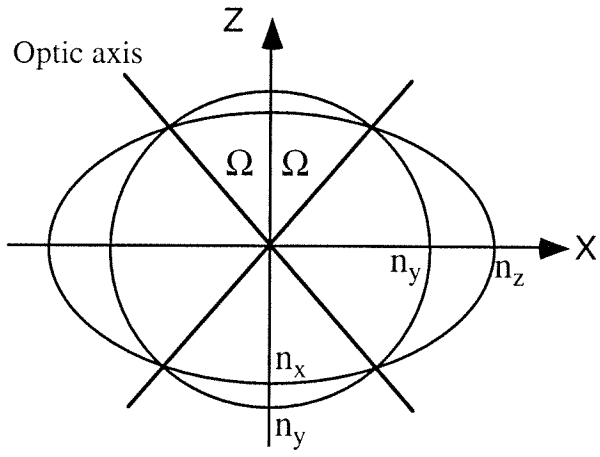

Figure 8-1

The projection of refractive index ellipse on the x-z plane for biaxial crystals. 2Ω is the angle between the two optics axes .

$KTiOPO_4$ (KTP), $KNbO_3$ (KN) and LiB_3O_5 (LBO) are all outstanding biaxial NLO crystals with space group mm2 [8-10]. Second harmonic generation of solid state Nd:YAG lasers and tunable optical parametric oscillators have been demonstrated in all three crystals. These materials form the basis of many NLO devices commercially available. The nonzero elements in the second order nonlinear optical coefficient tensor for biaxial crystals are deducible from the symmetry operations. These tensors are usually based on the crystallographic axes. The relationship of the principal axes of refractive index to the crystallographic axes is to some extent arbitrary, depending on the particular crystal. These will be described in this chapter.

8.2 Optical Mixing

The nonlinear optical response of a medium is described by an expansion of the induced optical polarization P in powers of the electric field amplitude E [11]:

$$P_i(t) = \varepsilon_0 \chi_{ij} E_j + d_{ijk} E_j E_k + 4\chi_{ijkl} E_j E_k E_l + \ldots \qquad (8\text{-}1)$$

The term $d_{ijk}E_jE_k$ describes first order optical nonlinearities responsible for three-wave mixing phenomena. These nonlinearities include second harmonic generation, and sum/difference frequency generation. Consider the interaction of a monochromatic wave:

$$E_j^{\omega 1} = \mathrm{Re}(E_j^{\omega 1} e^{i\omega 1 t}) = \frac{1}{2}(E_j^{\omega 1} e^{i\omega 1 t} + E_j^{\omega 1^*} e^{-i\omega 1 t}) \qquad (8\text{-}2)$$

with a crystal whose response is given by equation 8-1. This interaction mixes the two waves to produce new waves at the sum and difference frequencies. The optical wave at the sum frequency is induced by the term of the optical polarixation given by:

$$P_i^{\omega_3=\omega_1+\omega_2} = \sum_{j,k} d_{ijk}^{\omega_3,\omega_2,\omega_1} E_j^{\omega_1} E_k^{\omega_2} \, . \qquad (8\text{-}3)$$

Second harmonic generation is the degenerate case of three-wave mixing:

$$P_i^{2\omega} = \sum_{j,k} d_{ijk}^{2\omega,\omega,\omega} \; E_j^{\omega} \; E_k^{\omega} \; . \qquad (8\text{-}4)$$

The coupled wave equation describing the evolution of the second harmonic optical beam as it passes through the nonlinear crystal is given by [11]:

$$\frac{\partial E^{2\omega}}{\partial z} = -i\omega \sqrt{\frac{\mu}{\varepsilon}} d_{eff}^{2\omega,\omega,\omega} \; [E^{\omega}(z)]^2 \; e^{i\Delta kz} \; . \qquad (8\text{-}5)$$

Assume the crystal length is L. The output power $P^{2\omega}$ at a distance z=L from an input plane wave E^{ω} at z=0 is:

$$P^{2\omega} = 2\frac{(P^{\omega})^2}{A}\left(\frac{\mu}{\varepsilon_0}\right)^{3/2} \frac{\omega^2 (d_{eff}^{2\omega,\omega,\omega})^2 L^2}{n^3} \sin c^2(\Delta kL/2) \; . \qquad (8\text{-}6)$$

Figure 8-2 shows that when the phase matching condition is satisfied, two waves at ω_1 and ω_2 interact within the NLO crystal, generating a third wave at ω_3.

8.3 Phase Matching in Biaxial Crystals

In equation 8-6, Δk is the wavevector mismatch. To obtain significant second harmonic power it is necessary that $\Delta k = 0$. This is the phase matching condition, which is formally equivalent to a momentum conservation relation for the nonlinear interation.

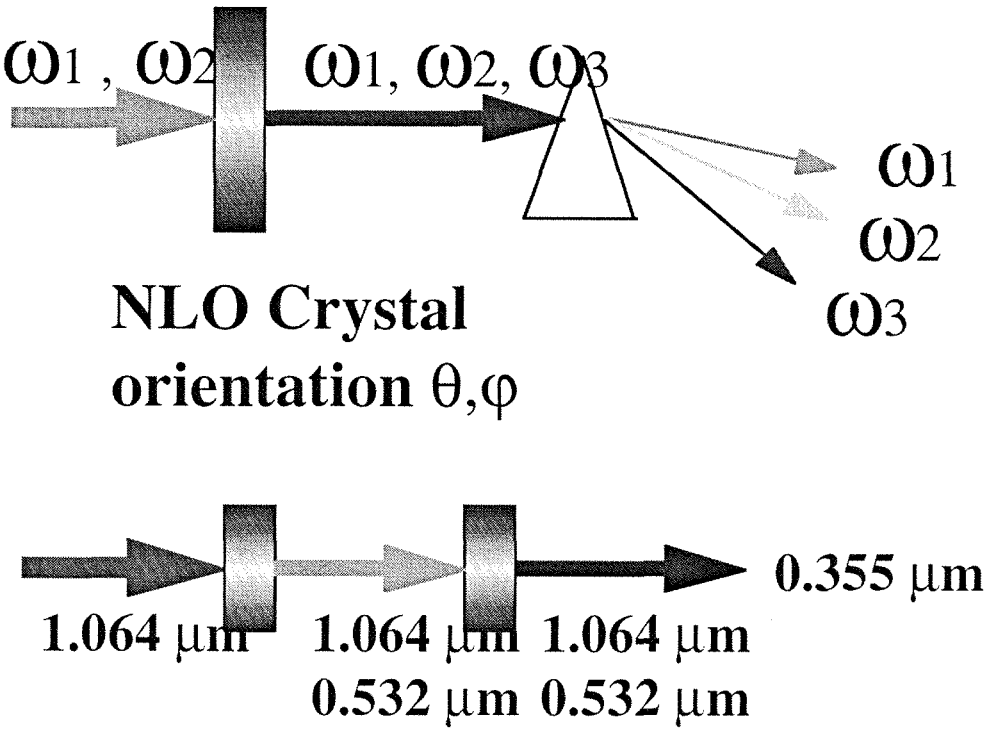

Figure 8-2

Upper figure illustrates that under phase matching condition, two waves at ω_1 and ω_2 interact within NLO crystal generating a third wave at ω_3. Lower figure gives an example of using two pieces of the NLO crystal with different angles cut to obtain three frequencies from a solid state Nd:YAG laser.

$$\Delta k = \left|\vec{k}^{2\omega} - 2\vec{k}^{\omega}\right| = \frac{2\omega}{c}(n^{2\omega} - n^{\omega}) \,. \qquad (8\text{-}7)$$

In normally dispersive materials, phase matching can be achieved by utilizing the anisotropic property of birefringence for certain wavelengths.

In three-wave mixing, we assume that $\omega_1 < \omega_2 < \omega_3$. The energy conservation relation gives:

$$\omega_1 + \omega_2 = \omega_3 \qquad (8\text{-}8)$$

and the phase matching condition gives:

$$n_1\omega_1 + n_2\omega_2 = n_3\omega_3. \qquad (8\text{-}9)$$

In general, two types of phase matching are possible. Type I describes the situation in which the optical waves at ω_1 and ω_2 are of the same polarization. Type II describes the situation in which the optical waves at ω_1 and ω_2 are of orthogonal polarizations. In a biaxial crystal, the refractive index of an optical beam propagating along the direction (θ,φ) is given by :

$$\frac{Sin^2\theta Cos^2\varphi}{n^{-2} - n_x^{-2}} + \frac{Sin^2\theta Sin^2\varphi}{n^{-2} - n_y^{-2}} + \frac{Cos^2\theta}{n^{-2} - n_z^{-2}} = 0 . \qquad (8\text{-}10)$$

where n_x, n_y,and n_z are principal refractive indices and $n_x < n_y < n_z$ is assumed. Two real solutions of refractive index n' and n" exist for three waves at ω_1, ω_2, and ω_3. The following condition is also assumed:

$$n_1' > n_1'' \ ; \ n_2' > n_2'' \ ; \ n_3' > n_3'' \ . \qquad (8\text{-}11)$$

The index of refractive requirements for the two types phase matching are, by momentum conservation:

$$n_3'' = \frac{\omega_1}{\omega_3} n_1' + \frac{\omega_2}{\omega_3} n_2' \qquad (8\text{-}12)$$

$$n_3'' = \frac{\omega_1}{\omega_3} n_1' + \frac{\omega_2}{\omega_3} n_2'' \qquad n_3'' = \frac{\omega_1}{\omega_3} n_1'' + \frac{\omega_2}{\omega_3} n_2' \ . \qquad (8\text{-}13)$$

(8-12) is for type I, (8-13) is for type II.

By solving the equations (8-10), (8-12) and (8-13), all of the directions (θ,φ) which satisfy the phase matching conditions can be determined. The intersection of these directions (θ,φ) and the surface of the refractive index ellipse forms a closed loci in 3D space. In the following section, a stereographic projection is used to aid in visualizing the distributions of the loci.

8.4 Topological Distribution

The stereographic projection is a common tool to assist in analyzing the structure of a crystal. Any point on a sphere given by an angle (θ,φ) can be mapped to a plane in such a way that arbitrary point P(x,y) is determined by

$$x = \frac{Sin\theta Cos\varphi}{1 + Sin\theta Sin\varphi} \quad ; \quad y = \frac{Cos\theta}{1 + Sin\theta Sin\varphi} \, . \qquad (8\text{-}14)$$

Figure 8-3 illustrates a stereographic projection (only a quadrant is needed in general). To study this distribution of angles, we divide this projection to four parts:

A1) $0° < \theta < \Omega$, $\varphi = 0°$

B1) $\Omega < \theta < 90°$, $\varphi = 0°$

B2) $\theta = 90°$, $0° < \varphi < 90°$

A2) $0° < \theta < 90°$, $\varphi = 90°$

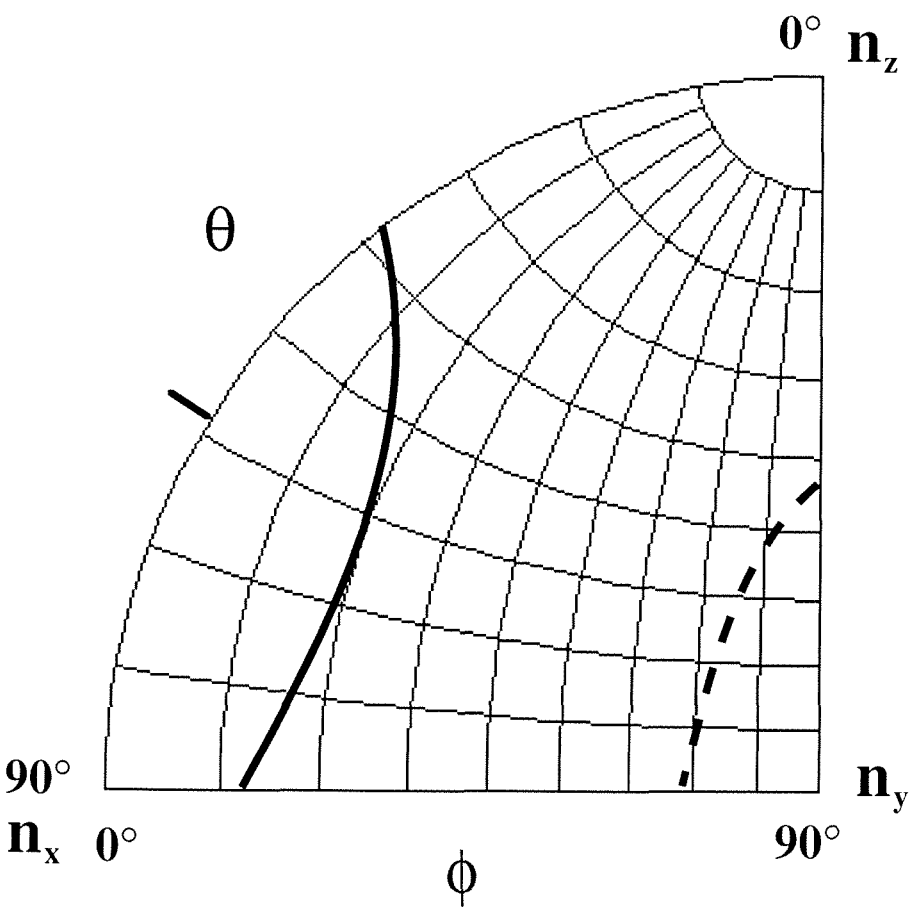

Figure 8-3(previous page)

Two typical phase matching curves projected stereographically. The solid line represents type I phase matching. The dashed line corresponds to type II phase matching and appears on the near side to the original point. The optics axis is at $\theta \sim 58°$.

In optically well-behaved biaxial crystals, phase matching loci start at part A1 or A2 and end at B1 or B2. There are thirty possible distributions of loci for the phase matching of three-wave mixing processes in biaxial crystals. They are shown schematically in figure 8-4. Quadrants with the principal refractive index x axis to the left, the principal refractive index y axis out of page and the principal refractive index z axis towards the top of the page. The continuous lines are the loci for type I processes and the dashed lines are for type II processes. The lines drawn between quadrants in figure 8-4 represent transitions from one critical phase matching situation to another wherein non-critical phase matching occurs because of an accidental equality of certain refractive indices. This case only occurs along either the x, y, or z axis. Processes involving parallel polarizations (type I) are seen to be phase matched along cones of whose vertices lie on the optic axes.

In general, the energy conservation relation for nonlinear processes involving many optical waves at different frequencies is:

$$\omega_1 + \omega_2 + \ldots + \omega_{s-1} = \omega_s \qquad (8\text{-}15)$$

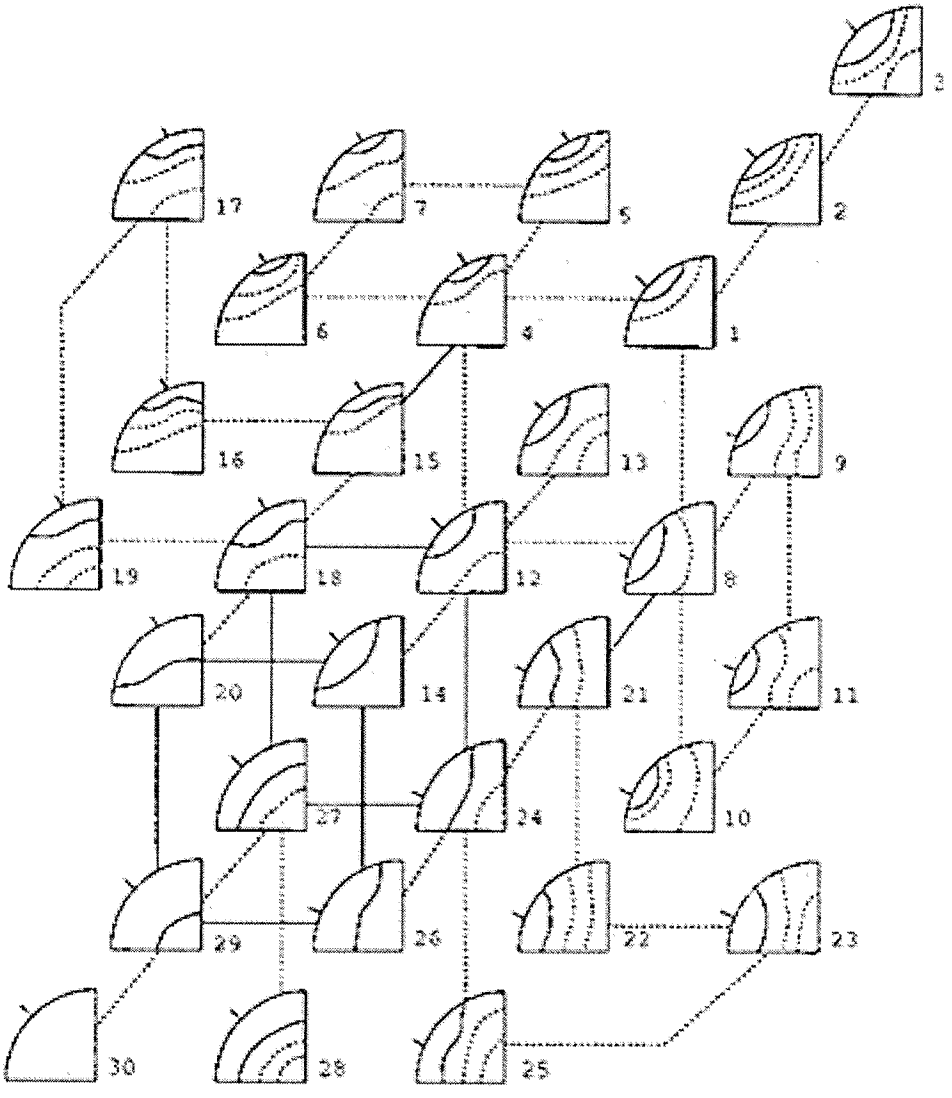

Figure 8-4

Schematic diagram of the possible loci of directions for phase matching in optically well behaved biaxial crystals. The continuous lines refer to type I, and the dashed lines to type II processes.

and the following relation is also assumed:

$$\omega_1 < \omega_2 < \ldots < \omega_{s-1} < \omega_s \ . \tag{8-16}$$

To simplify the mathematics, we define:

$$H_l = \frac{\omega_l}{\sum_{q=1}^{s-1} \omega_q} \ . \tag{8-17}$$

Then phase matching condition is expressed as:

$$n_s = \sum_{l=1}^{s-1} H_l n_l \ . \tag{8-18}$$

For type I phase matching, the refractive indices satisfy:

$$n_s^{''} = \sum_{l=1}^{s-1} H_l n_l^{'} \tag{8-19}$$

and for type II phase matching:

$$n_s^{''} = \sum_{l=1}^{s-1} H_l (n_l^{'} \bigcup n_l^{''}) \ . \tag{8-20}$$

The total number of possible distributions for phase matching is:

$$m = \sum_{p=0}^{2^{s-1}-1} [(p-r+1)^2 + 2\sum_{p'=0}^{p-1} p'] \quad . \tag{8-21}$$

In the first part of the square bracket, r is the fold numbers of degeneration. For example, second harmonic generation is one fold degeneration in three-wave mixing. The second part in the square bracket can be ignored in the general case. It must be counted only if the loci of phase matching start at part B1 and end at part B2 in figure 8-3. And it does not occur in optically well-behaved biaxial crystals.

8.5 Effective NLO Coefficient

Under the phase matching condition, the second harmonic power grows quadratically with the effective nonlinear coefficient. According to equation 8-6,

$$P^{2\omega} \sim d_{eff}^2 L^2 \quad . \tag{8-22}$$

The effective nonlinear coefficient d_{eff} is a function of d_{ijk} and the orientation of the crystals. For type I and type II phase matching, the effective nonlinear coefficients are given by [12]:

$$d_{eff}^{I} = d_{ijk} a_i^{e2} a_j^{e1} a_k^{e1} \tag{8-23a}$$

$$d_{eff}^{II} = d_{ijk} a_i^{e2} a_j^{e1} a_k^{e2} \quad , \tag{8-23b}$$

where

$$a^{e1} = \begin{pmatrix} Cos\theta Cos\varphi Cos\delta - Sin\varphi Sin\delta \\ Cos\theta Sin\varphi Cos\delta + Cos\varphi Sin\delta \\ -Sin\theta Cos\delta \end{pmatrix} \qquad (8\text{-}24)$$

$$a^{e2} = \begin{pmatrix} -Cos\theta Cos\varphi Sin\delta - Sin\varphi Cos\delta \\ -Cos\theta Sin\varphi Sin\delta + Cos\varphi Cos\delta \\ Sin\theta Sin\delta \end{pmatrix} \qquad (8\text{-}25)$$

and

$$ctg2\delta = \frac{ctg^2\Omega Sin^2\theta - Cos^2\theta Cos^2\varphi + Sin^2\varphi}{Cos\theta Sin2\varphi} \quad . \qquad (8\text{-}26)$$

8.6 KTP, LBO, and KN Crystals

The third order tensor has a total of 27 elements. By considering the symmetric properties of d_{ijk}, that is, $d_{ijk} = d_{ikj}$, the maximum number of independent elements reduces to 18 [13]. It is possible to compress the index notation of the d_{ijk}. The index i is left unchanged and jk is transformed to :

kj		new index
11	->	1
22	->	2
33	->	3
23, 32	->	4
13, 31	->	5
12, 21	->	6

This notation often simplifies equations considerably and will be used wherever convenient. However, it must be used with care because tensors contracted using this notation no longer obey tensor transformation and multiplication properties.

The nonzero elements in d_{ijk} for biaxial crystals are deducible from the symmetry operations for each point group. For mm2 (C_{2v}) group, the nonzero elements are :

$$d_{ijk} = \begin{pmatrix} 0 & 0 & 0 & 0 & d_{15} & 0 \\ 0 & 0 & 0 & d_{24} & 0 & 0 \\ d_{31} & d_{32} & d_{33} & 0 & 0 & 0 \end{pmatrix}. \qquad (8\text{-}27)$$

These tensors are usually referred to axes defined by the piezoelectric convention which is based upon the crystallographic axis. The relationship of the optical indicatrix to the crystallographic axes is to some extent arbitrary, depending on the particular crystals. It is more convenient

when considering phase matching to transform the d_{ijk} tensors from the piezoelectric axes to the principal axes x, y, and z of the optical indicatrix.

KTP, LBO, and KN crystals are in the same point group. After the transformation, the nonzero elements of the d_{ijk} tensor are:

$$KTP \quad \begin{matrix} x & m \\ y & m \\ z & 2 \end{matrix} \quad \begin{pmatrix} 0 & 0 & 0 & 0 & d_{15} & 0 \\ 0 & 0 & 0 & d_{24} & 0 & 0 \\ d_{31} & d_{32} & d_{33} & 0 & 0 & 0 \end{pmatrix} \tag{8-28}$$

$$LBO \quad \begin{matrix} x & m \\ y & 2 \\ z & m \end{matrix} \quad \begin{pmatrix} 0 & 0 & 0 & 0 & 0 & d_{15} \\ d_{31} & d_{33} & d_{32} & 0 & 0 & 0 \\ 0 & 0 & 0 & 0 & d_{24} & 0 \end{pmatrix} \tag{8-29}$$

$$KN \quad \begin{matrix} x & 2 \\ y & m \\ z & m \end{matrix} \quad \begin{pmatrix} d_{33} & d_{32} & d_{31} & 0 & 0 & 0 \\ 0 & 0 & 0 & 0 & 0 & d_{24} \\ 0 & 0 & 0 & 0 & d_{15} & 0 \end{pmatrix}. \tag{8-30}$$

From equations 8-23 through 8-30, we obtained the effective nonlinear coefficient for the mm2 group, in particular for KTP, LBO, and KN. The results are listed in table 8-1. The phase matching directions must be in either x, y, or z plane in order to reach the maximum coefficient.

Table 8-1

The effective nonlinear optical coefficient for the crystals with mm2 point group. The phase matching directions are in either x, y, or z plane in order to obtain the maximum coefficient.

Crystals	Orientation	d_{eff} (type I)	d_{eff} (type II)
mm2 (KTP)	$\theta = 90°$	0	$d_{24}Cos\varphi + d_{15}Sin\varphi$
	$\varphi = 90°$	0	$d_{15}Sin\theta$
	$\varphi = 0°, \theta < \Omega$	$d_{32}Sin\theta$	0
	$\varphi = 0°, \theta > \Omega$	0	$d_{24}Sin\theta$
m2m (LBO)	$\theta = 90°$	$d_{32}Cos\theta$	0
	$\varphi = 90°$	0	$d_{15}Cos\theta$
	$\varphi = 0°, \theta < \Omega$	0	$d_{24}Sin\theta - d_{15}Cos\theta$
	$\varphi = 0°, \theta > \Omega$	$d_{31}Cos\theta + d_{32}Sin\theta$	0
2mm (KN)	$\theta = 90°$	$d_{31}Sin\varphi$	0
	$\varphi = 90°$	$d_{33}Cos\theta + d_{31}Sin\theta$	0
	$\varphi = 0°, \theta < \Omega$	$d_{33}Cos\theta$	0
	$\varphi = 0°, \theta > \Omega$	0	$d_{15}Cos\theta$

8.7 Summary

It has been shown that the phase matching for three-wave interactions in biaxial crystal can be achieved in two types. The directions of polarizations in biaxial crystals are governed by the Biot-Fresnel law, which is shown analytically by equation 8-10. The general expression of the effective second order nonlinear coefficients in biaxial crystals under

the phase matching condition can be derived by taking into account the projection of the generated polarizations in the directions of the respective optical electric fields.

The topological distributions of phase matching loci has been described. Three-wave mixing processes display thirty types of possible distributions. Second harmonic generation is the degenerate case of three-wave mixing, displaying 14 types of phase matching loci.

The optimum operating directions under the phase matching condition in biaxial crystals can be obtained from the calculation of the effective nonlinear coefficients. In order to utilize bulk crystal and to achieve efficient conversion, the phase matching direction must be within the principal plane.

Finally, a set of analytical expressions of effective nonlinear optical coefficient for the crystals with mm2 point group is given. The phase matching directions are in either x, y, or z plane in order to obtain maximum coefficient.

References for Chapter Eight

[1] J. A. Giordmaine, Phys. Rev. Lett. **8**, 19 (1962).

[2] M. V. Hobden, J. Appl. Phys. **38**, 4365 (1967).

[3] J. A. Armstrong, N. Bloembergen, J. Ducuing, and P. S. Pershan, Phys. Rev. **127**, 1918 (1962).

[4] S. Somekh and A. Yariv, Opt. Commun. **6**, 301 (1972).

[5] M. M. Fejer, G. A. Magel, D. H. Jundt, and R. L. Byer, IEEE J. Quan. Elec. **QE-28**, 2631 (1992).

[6] A. Kewitsch, M. Segev, A. Yariv, G. Salamo, T. Towe, E. Sharp, R. Neurgoankar, Appl. Phys. Lett. **64**, 3068 (1994).

[7] S. Orlov, A. Yariv, and M. Segev, Appl. Phys. Lett, **68**, 1610 (1996).

[8] F. C. Zumsteg, J. D. Bierlein, and T. E. Gier, J. Appl. Phys. **47**, 4980 (1976).

[9] J. C. Baumert, J. Hoffnagle, and P. Gunter, Appl. Opt. **24**, 1299 (1985).

[10] C. Chen, Y. Wu, A. Jiang, B. Wu, G. You, and S. Lin, J. Opt. Soc. Am. B. **6**, 616,(1989).

[11] A. Yariv, Quantum Electronics (Saunder College Publishing, Philadelphia, 1991).

[12] H. Ito, H. Naito, and H. Inaba, J. Appl. Phys. **46**, 3992, (1975).

[13] D. A. Kleinman, Phys. Rev. **126**, 1977 (1962).

Chapter Nine

Relevant Publications

Ferroelectric domain gratings and Barkhausen spikes in potassium lithium tantalate niobate

Xiaolin Tong , Amnon Yariv, Min Zhang, Aharon Agranat
Rudolf Hofmeister, and Victor Leyva
Appl. Phys. Lett. **70**, 2241 (1997).

Copper, hydrogen and titanium incorporation in potassium lithium tantalate niobate single crystals

Xiaolin Tong, Min Zhang, Amnon Yariv, and Aharon Agranat
Appl. Phys. Lett. **70**, 1688 (1997).

Three dimensional polarization dependence of OH bands absorption in potassium niobate crystals

Xiaolin Tong , Min Zhang, Amnon Yariv, and Aharon Agranat
Appl. Phys. Lett. **70**, 429 (1997).

Thermal fixing of volume holograms in potassium niobate

Xiaolin Tong , Min Zhang, Amnon Yariv, and Aharon Agranat
Appl. Phys. Lett. **69**, 3966 (1996).

Diffusion of hydrogen in $K_{1-y}Li_yTa_{1-x}Nb_xO_3$:doped crystals

Xiaolin Tong , Min Zhang, Amnon Yariv, and Aharon Agranat

Appl. Phys. Lett. **69**, 3345 (1996).

Fixing of volume holograms in ferroelectric $K_{1-y}Li_yTa_{1-x}Nb_xO_3$

Xiaolin Tong , Rudolf Hofmeister, Min Zhang, Amnon Yariv, Aharon Agranat, and Victor Leyva

Opt. Lett. **21**, 1860 (1996).

Near infrared absorption and dark conductivity of $K_{1-y}Li_yTa_{1-x}Nb_xO_3$ *crystal*

Xiaolin Tong , Min Zhang, Amnon Yariv, Aharon Agranat Rudolf Hofmeister, and Victor Leyva

Appl. Phys. Lett. **69**, 479 (1996).

Fixing of photorefractive volume holograms in $K_{1-y}Li_yTa_{1-x}Nb_xO_3$

Victor Leyva, Doruk, Engin, Xiaolin Tong , Min Zhang, Amnon Yariv, and Aharon Agranat

Opt. Lett. **21**, 1321 (1995).